

# Patient-specific modelling of the cerebral circulation for aneurysm risk assessment

**Citation for published version (APA):**

Mulder, G. (2011). *Patient-specific modelling of the cerebral circulation for aneurysm risk assessment*. [Phd Thesis 1 (Research TU/e / Graduation TU/e), Biomedical Engineering]. Technische Universiteit Eindhoven. <https://doi.org/10.6100/IR721569>

**DOI:**

[10.6100/IR721569](https://doi.org/10.6100/IR721569)

**Document status and date:**

Published: 01/01/2011

**Document Version:**

Publisher's PDF, also known as Version of Record (includes final page, issue and volume numbers)

**Please check the document version of this publication:**

- A submitted manuscript is the version of the article upon submission and before peer-review. There can be important differences between the submitted version and the official published version of record. People interested in the research are advised to contact the author for the final version of the publication, or visit the DOI to the publisher's website.
- The final author version and the galley proof are versions of the publication after peer review.
- The final published version features the final layout of the paper including the volume, issue and page numbers.

[Link to publication](#)

**General rights**

Copyright and moral rights for the publications made accessible in the public portal are retained by the authors and/or other copyright owners and it is a condition of accessing publications that users recognise and abide by the legal requirements associated with these rights.

- Users may download and print one copy of any publication from the public portal for the purpose of private study or research.
- You may not further distribute the material or use it for any profit-making activity or commercial gain
- You may freely distribute the URL identifying the publication in the public portal.

If the publication is distributed under the terms of Article 25fa of the Dutch Copyright Act, indicated by the "Taverne" license above, please follow below link for the End User Agreement:

[www.tue.nl/taverne](http://www.tue.nl/taverne)

**Take down policy**

If you believe that this document breaches copyright please contact us at:

[openaccess@tue.nl](mailto:openaccess@tue.nl)

providing details and we will investigate your claim.

# **Patient-specific modelling of the cerebral circulation for aneurysm risk assessment**

Gwen Mulder

CIP-DATA LIBRARY TECHNISCHE UNIVERSITEIT EINDHOVEN

Mulder, Gwen

Patient-specific modelling of the cerebral circulation for aneurysm risk assessment

Eindhoven University of Technology, 2011.

Proefschrift.

A catalogue record is available from the Eindhoven University of Technology Library.

ISBN: 978-90-9026414-1

Copyright © 2011 by Gwen Mulder. All rights reserved.

This thesis is prepared with L<sup>A</sup>T<sub>E</sub>X 2<sub>ε</sub>

Cover design: Gwen Mulder and Frederike Manders – *MaMaproducties.nl*

Printed by Ipskamp Drukkers, Enschede, The Netherlands

# Patient-specific modelling of the cerebral circulation for aneurysm risk assessment

## Proefschrift

ter verkrijging van de graad van doctor  
aan de Technische Universiteit Eindhoven,  
op gezag van de rector magnificus, prof.dr.ir. C.J. van Duijn,  
voor een commissie aangewezen door het College voor Promoties  
in het openbaar te verdedigen op  
woensdag 14 december 2011 om 16.00 uur

door

Gwen Mulder

geboren te Eindhoven

Dit proefschrift is goedgekeurd door de promotor:

prof.dr.ir. F.N. van de Vosse

Copromotoren:

dr.ir. A.C.B. Bogaerds

en

dr.ir. P.M.J. Rongen

# Contents

---

<b>Contents</b>	<b>vii</b>
<b>Summary</b>	<b>ix</b>
<b>Nomenclature</b>	<b>xi</b>
<b>I Introduction</b>	<b>I</b>
I.1 Physiological background . . . . .	2
I.2 Pathological background . . . . .	4
I.3 Measurement techniques . . . . .	7
I.4 Computational techniques . . . . .	8
I.5 Objective . . . . .	II
I.6 Outline . . . . .	II
<b>2 Vortex dynamics in cerebral aneurysms</b>	<b>13</b>
2.1 Introduction . . . . .	14
2.2 Materials and Methods . . . . .	16
2.2.1 CFD . . . . .	16
2.2.2 Vortex identification . . . . .	18
2.2.3 Experiment . . . . .	18
2.2.4 Data acquisition and postprocessing . . . . .	19
2.3 Results . . . . .	19
2.4 Discussion and conclusions . . . . .	24
<b>3 Geometrical variations in a 1D model</b>	<b>27</b>
3.1 Introduction . . . . .	28
3.2 Materials and methods . . . . .	29
3.2.1 Measurement methods . . . . .	29
3.2.2 Data processing . . . . .	30
3.2.3 1D wave propagation model . . . . .	31
3.3 Results . . . . .	35
3.4 Discussion . . . . .	37

---

3.4.1	General findings . . . . .	37
3.4.2	Case study . . . . .	38
3.4.3	Impact on clinical application . . . . .	39
3.5	Conclusion . . . . .	40
<b>4</b>	<b>Patient-specific boundary conditions for 3D CFD</b>	<b>41</b>
4.1	Introduction . . . . .	42
4.2	Materials and methods . . . . .	42
4.2.1	Geometry domain . . . . .	42
4.2.2	Computational model . . . . .	43
4.2.3	Boundary conditions . . . . .	44
4.2.4	Data analysis . . . . .	45
4.3	Results . . . . .	46
4.4	Discussion and conclusions . . . . .	55
4.5	Conclusion . . . . .	56
4.5.1	Acknowledgement . . . . .	56
<b>5</b>	<b>The influence of injection</b>	<b>57</b>
5.1	Introduction . . . . .	58
5.2	Materials and methods . . . . .	59
5.2.1	Governing equations for a single vessel . . . . .	59
5.2.2	Arterial network . . . . .	61
5.2.3	Boundary conditions . . . . .	62
5.2.4	Virtual patients . . . . .	63
5.2.5	Injection . . . . .	64
5.3	Results . . . . .	65
5.4	Discussion . . . . .	69
5.5	Conclusion . . . . .	72
<b>6</b>	<b>Patient-specific characterisation of the pressure decay in diastole</b>	<b>75</b>
6.1	Introduction . . . . .	76
6.2	Materials and methods . . . . .	77
6.2.1	Compliance from the pressure waveform and relative diastolic flow . . . . .	77
6.2.2	Data acquisition . . . . .	78
6.2.3	Data processing . . . . .	79
6.3	Results . . . . .	79
6.3.1	Gain-normalised pressure waves . . . . .	79
6.3.2	Time-gain-normalised pressure waves . . . . .	82
6.4	Discussion . . . . .	83
6.5	Conclusion . . . . .	84
6.5.1	Acknowledgement . . . . .	84

---

<b>7</b>	<b>Discussion, conclusions and recommendations</b>	<b>85</b>
7.1	General discussion . . . . .	86
7.2	Work flow . . . . .	87
7.3	Conclusions . . . . .	89
<b>A</b>	<b>Model parameters</b>	<b>93</b>
<b>B</b>	<b>Pressure during injection</b>	<b>101</b>
B.1	Introduction . . . . .	102
B.2	Methods . . . . .	102
B.3	Results . . . . .	102
B.4	Conclusion . . . . .	102
	<b>Bibliography</b>	<b>105</b>
	<b>Samenvatting</b>	<b>119</b>
	<b>Acknowledgements</b>	<b>121</b>
	<b>Curriculum Vitae</b>	<b>123</b>



# Summary

---

## Patient-specific modelling of the cerebral circulation for aneurysm risk assessment

Cerebral aneurysms are localised pathological dilatations of cerebral arteries, most commonly found in the circle of Willis. Although not all aneurysms are unstable, the major clinical concern involved is the risk of rupture. High morbidity and mortality rates are associated with the haemorrhage resulting from rupture. New indicators of aneurysm stability are sought, since current indicators based on morphological factors have been shown to be unreliable.

Haemodynamical factors are known to be relevant in vascular wall remodelling, and therefore believed to play an important role in aneurysm development and stability. Studies suggest that intra-aneurysmal wall shear stress and flow patterns, for example, are candidate parameters in aneurysm stability assessment. These factors can be estimated if the 3D patient-specific intra-aneurysmal velocity is known, which can be obtained via a combination of *in vivo* measurements and computational fluid dynamics models. The main determinants of the velocity field are the vascular geometry and flow through this geometry. Over the last decade the extraction of the vascular geometry has become well-established. More recently, there has been a shift of attention towards extracting boundary conditions for the 3D vascular segment of interest.

The aim of this research is to improve the reliability of the model-based representation of the velocity field in the aneurysmal sac. To this end, a protocol is proposed such that patient-specific boundary conditions for the 3D segment of interest can be estimated without the need for added invasive procedures. This is facilitated by a 1D wave propagation model based on patient-specific geometry and boundary conditions measured non-invasively in more accessible regions. Such a protocol offers improved statistical reliability owing to the increased number of patients that can participate in studies aiming to identify parameters of interest in aneurysm stability assessment.

In chapter 2 the intra-aneurysmal velocity field in an idealised aneurysm model is validated with particle image velocimetry experiments, after which the flow patterns are evaluated using a vortex identification method. Chapter 3 describes a 1D model wave

propagation model of the cerebral circulation with a patient-specific vascular geometry. The resulting flow pulses at the boundaries of the 3D segment of interest are compared to those obtained with a patient-generic geometry. The influence of these different boundary conditions on the 3D intra-aneurysmal velocity field is evaluated in chapter 4 by prescribing the end-diastolic flows extracted from the 1D models. In order to measure blood flow with videodensitometric methods, an injection of contrast agent is required. The effect of this injection on the flow of interest is assessed in chapter 5. In chapter 6, pressure measurements in the internal carotid are used to evaluate the variability of pressure waveform and its effect on the boundary conditions for the 1D model. Finally, a protocol for full patient-specific modelling is discussed in chapter 7.

# Nomenclature

---

Table 1: List of symbols.

Symbol	Description
$C_0$	Compliance per unit length
$C_{0D}$	Compliance captured by the windkessel model (0D)
$C_{1D}$	Compliance captured by the wave propagation model (1D)
$C$	Capacitor describing peripheral compliance in the windkessel models
$E$	Young's modulus
$N$	Number of outlets within a vascular domain
$R$	Resistance describing part of the peripheral resistance in the windkessel models
$Z$	Characteristic impedance describing part of the peripheral resistance in the windkessel models
$R_t$	Total peripheral resistance, $R + Z$
$R_T$	Total resistance of the human vascular system
$R_{VD}/R_{BP}$	Total resistance of a vascular domain
$a$	Radius
$a_0$	Radius when $p = p_0$
$a_t^n$	Sum of $a^n$ within a vascular domain, where $n = 2, 3$ if the resistance distribution is based on the wall shear stress or surface area, respectively
$h$	Wall thickness
$m$	m-factor; fraction of the injection rate that is added to the natural blood flow
$p$	Hydrostatic pressure
$p_0$	Initial pressure
$q$	Flow rate
$q_B$	Physiological blood flow before injection
$q_D$	Combined flow during injection
$q_I$	Flow rate of the injection

Table 1: continued

Symbol	Description
$q_{I,m}$	Maximum flow rate of the injection
$q_{1D,i}$	The flow from the 1D model prescribed at the corresponding $i^{\text{th}}$ outlet in the 3D model
$t$	Time
$t_b$	Time at the beginning of the injection
$t_e$	Time at the end of the injection
$v$	Velocity vector
$\bar{v}$	Cross-sectional average of the velocity
$z$	Axial coordinate of an arterial segment
$\Gamma$	Boundary of the 3D domain
$\Omega$	3D domain
$\lambda_i$	$i^{\text{th}}$ eigenvalue where $\lambda_i < \lambda_{i+1}$
$\zeta$	Ratio of the diastolic flow to the mean flow

Table 2: Abbreviations (vascular names are provided in appendix A).

Abbreviation	Description
3D-RA	3D rotational angiography
APG	Model geometry based on patient-generic data by Alastruey
APS	Model geometry based on patient-generic data by Alastruey and patient-specific data
CFD	Computational fluid dynamics
COW	Circle of Willis
GAR	Segmentation based on geodesic active regions
ISO	Segmentation based on iso-intensity surface extraction
pc-MR	Phase-contrast magnetic resonance
PIV	Particle image velocity
PG	Patient-generic
PS	Patient-specific
RPG	Model geometry based on patient-generic data by Reymond
RPS	Model geometry based on patient-generic data by Reymond and patient-specific data
TCD	Transcranial doppler

# CHAPTER ONE

## Introduction

---

Cerebral aneurysms are localised dilatations of the arterial wall in the brain, which may be prone to rupture. In the event of rupture, the blood in the brain tissue leads to serious complications associated with high morbidity and mortality rates. Although as many as 25% of the population older than 50 years harbours these lesions, the annual rupture rate is low (about 2% of all aneurysms). This indicates that the majority of the cerebral aneurysms are stable and intervention would impose an unnecessary risk on the patient. Current indicators for aneurysm stability, based on morphological factors, are found to be unreliable. As haemodynamics are involved in remodelling of the arterial wall, analysis of the intra-aneurysmal velocity field is likely to provide candidate indicators for aneurysm stability. In this chapter the pathological background of aneurysms and the current clinical status of aneurysm diagnostics and treatment are addressed, thereby introducing the problems involved aneurysm risk assessment. The strategy adopted in this research and outline of the thesis are given.

## 1.1 Physiological background

The cerebral vasculature is a complex arterial network including many collateral pathways in order to provide all parts of the brain with oxygen even in case of an arterial obstruction. The collateral circulation includes both extracranial sources and intracranial pathways (fig 1.1). The latter is commonly divided into primary collateral pathways, which include the arteries in the circle of Willis (COW), and secondary collaterals consisting of smaller arteries (Liebeskind, 2003).

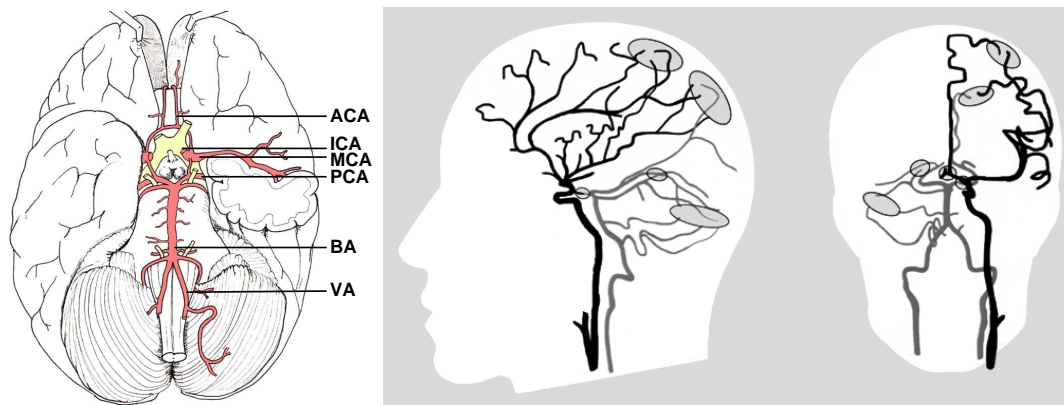


**Figure 1.1:** The main collateral pathways in the cerebral arterial circulation consist of (left) the circle of Willis (COW; adapted from <http://library.med.utah.edu/kw/hyperbrain/>) and (right) the secondary pathways (adapted from Liebeskind (2003)).

Both the basilar (BA) and internal carotid arteries (ICA) supply the brain with blood, which is redistributed via the COW. The lengths and radii of the arterial segments of the COW show significant inter-patient variability (David and Moore, 2008). Moreover, in a significant proportion of the general population one or more arterial segments in the circle of Willis are hypoplastic or absent, as only about 50% has a complete COW (David and Moore, 2008). If one or more arteries are absent, the other segments adapt to compensate, such that sufficient oxygenation of the peripheral brain tissue is ensured. As the resistance of a tube is proportional to the radius raised to the fourth power, and thus small variations of vessel caliber can have a profound effect on the blood flow distribution, a correspondingly high variability of the blood flow through the different arterial segments within the COW is to be expected. Indeed, Tanaka et al. (2006) found a significant correlation between variations in the circle of Willis and the relative flow rates of the internal carotid and basilar artery.

In a literature review by Fahrig et al. (1999), the reported mean blood flow in the ICA and vertebral artery (VA) are  $4.6 \text{ ml s}^{-1}$  and  $1.3 \text{ ml s}^{-1}$ , respectively. Care should be taken when comparing the results of different studies, as the cerebral blood flow decreases with age while many studies are based on healthy, often young, volunteers (Yazici et al., 2005). This might partially explain the differences observed in ICA and VA blood flow (table 1.1). Although the absolute blood flow differs significantly between patients, the gain nor-

**Table 1.1:** The flow rate in the ICA, BA and VA in  $\text{ml s}^{-1}$  based on  $n$  patients.

Ref	$q_{ICA}$	$\pm$	$SD$	$q_{BA}$	$\pm$	$SD$	$q_{VA}$	$\pm$	$SD$	Method	$n$
Cebral et al. (2008)	4.1	$\pm$	0.8	-			1.4	$\pm$	0.8	pc-MR	44
Ford et al. (2005a)	4.6	$\pm$	0.9	-			1.5	$\pm$	0.3	pc-MR	17
Schöning et al. (1994)	4.4	$\pm$	1.0	-			1.4	$\pm$	0.6	TCD	48
Scheel et al. (2000)	4.2	$\pm$	0.9	2.6	$\pm$	0.8	-			TCD	78
Enzmann et al. (1994)	4.8	$\pm$	0.4	2.4	$\pm$	0.2	-			pc-MR	10
Tanaka et al. (2006)	5.6	$\pm$	1.1	2.2	$\pm$	0.6	-			pc-MR	117
Oktar et al. (2006)	4.0	$\pm$	1.6	-			0.9	$\pm$	0.5	B-flow US	40
Oktar et al. (2006)	3.6	$\pm$	1.4	-			0.8	$\pm$	0.5	pc-MR	40

**Table 1.2:** The flow distribution over the outlets.

Ref	$q_{ACA}[\%]$	$q_{MCA}[\%]$	$q_{PCA}[\%]$
Tanaka et al. (2006)	20	60	20
Enzmann et al. (1994)	19	56	25

malised flow waveform shows relatively low inter-patient variability. Ford et al. (2005a) defined a characteristic waveform in the ICA based on well-defined points on the curve, e.g. the systolic peak and the diastolic minimum. The correlation found between the mean volumetric flow and the systolic peak suggests that the derived waveform characteristics may be used to estimate the ICA flow waveform if the mean flow is available. This corresponds to the findings of Holdsworth et al. (1999), who analysed the common carotid artery (CCA) waveforms.

The flow distribution over the ICAs and VAs is approximately 75 – 80% and 20 – 25% of the total cerebral blood flow, respectively (Ford et al., 2005a; Buijs et al., 1998; Enzmann et al., 1994). Less extensively studied is the flow distribution over the outlets, i.e., the anterior cerebral artery (ACA), middle cerebral artery (MCA) and posterior cerebral artery (PCA). Tanaka et al. (2006) estimated the flow distribution over the ACA, MCA and PCA from pc-MR measurements in the ICAs and BA in different configurations of the circle of Willis. Enzmann et al. (1994) reported mean blood flows in the ACA:MCA:PCA of 0.6 : 1.8 : 0.8 ml per cardiac cycle, which results in a similar flow distribution (table 1.2).

Since oxygen deprivation in brain tissue can only be tolerated for tens of seconds before significant damage occurs David and Moore (2008), the regulatory mechanisms involved in maintaining perfusion need to be faster than, for example, increasing systemic blood pressure. The cerebral autoregulation responds to variations in for example systemic blood pressure, cerebral flow and oxygen concentration (Aaslid et al., 1989; Aaslid, 2006), further complicating the cerebral haemodynamics.

## 1.2 Pathological background

Arterial aneurysms are localised dilatations of blood vessels caused by a congenital or acquired weakness of the media (fig 1.2). A variety of characteristic geometries can be distinguished. In the cerebral arteries the most common type is the saccular aneurysm. Geometrical classification of the aneurysmal sac based on morphological factors, e.g., the dome and neck size, indicate a typical aneurysm is almost spherical of shape, with the exception of the more pear-shaped ACoA aneurysms (Parlea et al., 1999). The vast majority of human intracranial aneurysms are found at the branching sites of the COW.

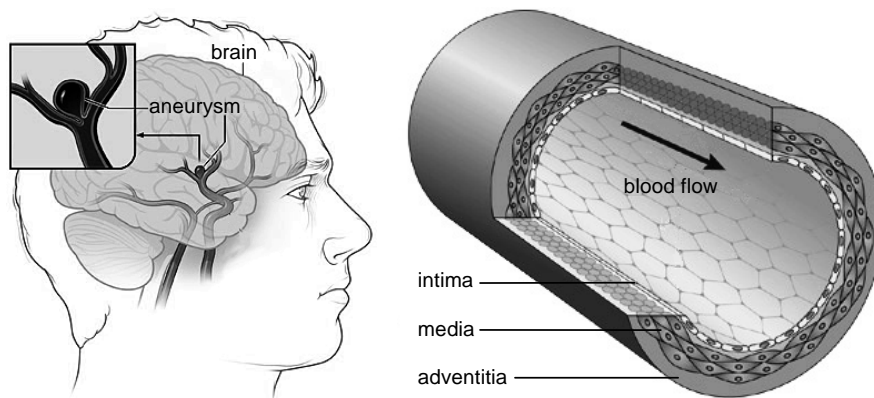


**Figure 1.2:** (left) Cerebral aneurysms are most commonly found in the branches of the COW (adapted from [www.fromyourdoctor.com](http://www.fromyourdoctor.com)) (right) the arterial wall is a heterogeneous 3-layered structure (adapted from Hahn and Schwartz (2009)).

In general, the arterial wall consists of three layers: the intima, media and adventitia (fig 1.2). In healthy cerebral arteries the adventitia is typically less developed compared to other vascular domains. The aneurysm wall typically lacks the media and internal elastic lamina, leaving a thin, fibrous membrane of  $20 - 100\mu\text{m}$  consisting mostly of collagen (Kyriacou and Humphrey, 1996). Although the pathogenesis of cerebral aneurysm is not clear, two theories on the etiology exist. Cerebral aneurysms are believed to be caused by either acquired degenerative changes in the arterial wall or congenital defects in the muscular layer of the cerebral arteries at bifurcations (Lieber et al., 2002; Kyriacou and Humphrey, 1996). Although the mechanisms are not well understood due to the many factors involved, it is commonly accepted that haemodynamics are involved in the pathological remodelling leading to growth and degeneration of the arterial wall .

Most cerebral aneurysms are asymptomatic and therefore remain undetected (Johnston et al., 2002). Although the reported prevalence of unruptured intracranial aneurysms varies significantly, the most commonly accepted prevalence in the general population is within the of range  $1 - 2\%$  (Winn et al., 2002; Rinkel et al., 1998; Mitchell et al., 2004). It should be noted that aneurysms develop during adulthood resulting in higher prevalence if people younger than 30 years old are excluded. About  $15 - 20\%$  of all people harbouring a cerebral aneurysm have multiple lesions (Kyriacou and Humphrey, 1996; Lieber et al., 2002). Although not every aneurysm is life threatening, rupture of an intracra-

nial aneurysm results in subarachnoid hemorrhage (SAH), with mortality and morbidity rates as high as 70% and 10%, respectively (Mitchell and Jakubowski, 2000). The overall annual rupture rate is believed to be 1 – 2% (Chen et al., 2004b; Winn et al., 2002; Juvela et al., 2000), which adds up to a significant life-time risk. The incidence rate of SAH is approximately 10 per 100000 person years, and approximately 85% of all spontaneous hemorrhages are caused by intracranial aneurysms (van Gijn and Rinkel, 2001).

Depending on factors like the aneurysmal and vascular geometry, location within the arterial tree and patient age, the possible treatments for a patient with an unruptured cerebral aneurysm are surgical clip placement, endovascular coil occlusion and stenting (fig 1.3). In surgical clipping blood is prevented from entering the aneurysmal sac by placing a metal clip across the neck of the aneurysm. Endovascular coil occlusion consists of packing platinum coils in the aneurysmal sack, thereby decreasing the intra-aneurysmal flow such that thrombus formation is promoted. Depending on various geometrical factors, such as neck width and orientation of the aneurysm relative to the parent artery, stenting prior to coil placement might be required (Liou and Liou, 2004; Chen et al., 2004a; Gnanalingham et al., 2006; Yavuz et al., 2008). There are only a few articles reporting stenting without coil occlusion as endovascular treatment option for cerebral aneurysms (Lieber et al., 2002; Terada et al., 2005; Fiorella et al., 2004), and recently it has been suggested that sole stenting of giant aneurysms may be associated with higher risks than expected (Pavlis et al., 2010). As the highly tortuous afferent arteries are locally embedded in the skull, making endovascular navigation precarious, special stents to be used in intra-cranial pathologies are in development. Although Slosberg (1997) reported significantly lower rupture rates in a group of patients treated with hypotensive medication, the question whether this approach would be more a efficacious treatment remains unanswered (Mitchell et al., 2004).

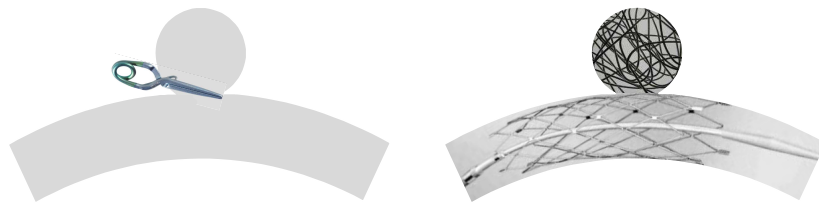


**Figure 1.3:** Possible treatments are (left) clipping, (right) coiling and/or stenting.

According to Koivisto no significant difference was detected in the outcome one year after surgical or endovascular treatment of ruptured cerebral aneurysms (Koivisto et al., 2000). The International Subarachnoid Aneurysm Trial (ISAT), a large scale trial on ruptured aneurysms involving 42 centers in Europe and America, reported that the risk of death or significant disability for endovascular treatment in patients with ruptured aneurysm is significantly lower than for surgical patients (Molyneux, 2002; Molyneux et al., 2005), with the absolute one-year follow-up risks of dependency or death associated with clipping and coiling being 30.9% and 23.5%, respectively. Endovascular treatment appears to be safer choice (Molyneux et al., 2009; Koebe et al., 2006), and the ISAT has changed the management of ruptured aneurysms by increasing the proportion of

patients undergoing endovascular treatment (Gnanalingham et al., 2006).

In the 1970s the benefits of surgical clipping were proven and this became the standard treatment of ruptured aneurysms (Mitchell et al., 2004). Unruptured aneurysms identified in those days were almost exclusively additional aneurysms, i.e., the patient already presented himself with a ruptured aneurysm. In the early 1990s, all aneurysms were considered life threatening and surgical clipping was performed if the aneurysm location was accessible (Mitchell et al., 2004). With the improvement of noninvasive imaging modalities, an increasing number of incidental aneurysms was found. Although additional and incidental aneurysms were initially treated equally, it is now known that the latter harbour a lower risk of rupture (Mitchell et al., 2004; Singh et al., 2009; Wiebers et al., 2002), thereby raising the issue of aneurysm stability assessment.

The decision whether intervention is recommended depends on the balance between the risk of rupture and the risk related to the intervention itself. Risk factors for aneurysm rupture include patient age, cigarette smoking, familial history and aneurysm morphology. Although the dome size is known to be related to the risk of rupture, the critical size could not be defined as other factors play a significant role as well. The intra-aneurysmal velocity field affects aneurysm growth and rupture (Ujiie et al., 1999). Low flow induces degenerative changes in the arterial wall, thereby increasing the risk of rupture. Since a high aspect ratio corresponds to low intra-aneurysmal velocities, the aspect ratio is indicative of rupture (Nader-Sepahi et al., 2004). Following the same reasoning, daughter aneurysms increase the rupture risk significantly (Nader-Sepahi et al., 2004). Aneurysm growth is associated with risk of rupture (Juvela et al., 2001), aneurysms located at the ACoA or PCoA are more likely to rupture than those found in the middle cerebral artery (Mitchell et al., 2004). Although all these factors are known to contribute to the risk of rupture, and recommendations on the management of cerebral aneurysms based on subsets of known indicators have been formulated (Rinkel, 2008; Burns and Brown, 2009), a reliable assessment of the actual rupture risk of an individual aneurysm remains elusive (Singh et al., 2009; Lall et al., 2009). Moreover, the indicators currently used to identify unstable aneurysms that require treatment coincide with the indicators for poor intervention outcome (Singh et al., 2009), further complicating the decision whether it is prudent to intervene.

From a mechanical point of view, the mechanical properties and loading state of the arterial wall are the most important factors in the determination whether rupture of the aneurysm is a serious threat. Currently, the mechanical properties of the wall cannot be measured directly *in vivo*. The cerebral arteries show little movement over the cardiac cycle due to the relatively high wall stiffness and surrounding tissue. However, as the temporal and spatial resolution of the imaging modalities have improved significantly over the past decade this cyclic wall movement can be measured (Zhang et al., 2009; Dempere-Marco et al., 2006), which may allow estimation of the mechanical properties of the wall.

The loading state is defined by the transmural pressure and the forces exerted by the blood flow. In contrast to the flow induced shear stress, the pressure load is a global parameter, although the pressure-induced wall stress will show spatial variations related

to the local geometry and mechanical properties of the arterial wall. Furthermore, the cyclic loading is thought to affect the arterial wall from both mechanical (Mitchell et al., 2006b) and biomechanical point of view. As aneurysms are local lesions and the forces induced by the flow are known to be involved in wall adaptation and degradation (Singh et al., 2009), analysis of the 3D intra-aneurysmal velocity is likely to provide more reliable indicators for rupture risk. A schematic overview of the haemodynamical factors involved is provided in chapter 2.

Since imaging modalities have improved significantly over last decades, 3D velocity fields can be measured directly *in vivo* using 4D phase-contrast Magnetic Resonance Angiography (4D pc-MRA). However, the resolution is currently too low to capture the high velocity gradients present in the aneurysmal sac, resulting in significant errors in derived quantities (Hollnagel et al., 2009; Boussel et al., 2009; Isoda et al., 2010). Computational Fluid Dynamics (CFD) provides high-resolution velocity fields, although boundary conditions need to be prescribed in order to obtain representative flow patterns. Therefore, *in vivo* measurements and CFD modelling are complementary methods; the arterial geometry and boundary conditions extracted from patient data provide the input for the computational model.

## 1.3 Measurement techniques

The geometry of arterial tree can be obtained using Computed Tomography Angiography (CTA), MRA or 3D-RA. The latter is the preferred method for treatment planning due to its superior spatial and contrast resolution. However, for diagnosis and follow-ups, the noninvasive CTA and MRA are used often (Bogunovic et al., 2011).

There are several methods available to measure *in vivo* flows or velocities, including Trans-Cranial Doppler ultrasonography (TCD), MRA and x-ray densitometry. The first two are non-invasive techniques, while the latter requires the injection of a contrast agent in order to visualise the blood.

In TCD the peak velocity waveform is measured at one location in the cerebral vasculature. This can be converted to flows if the local diameter is known, although assumptions on the velocity profile are required (see e.g., Beulen et al. (2010) and Leguy et al. (2009)). Drawbacks of this method are the handler-dependency and the absence of the required temporal window in 10 – 15% of all patients (Tsvigoulis et al., 2009). Furthermore, as simultaneous measurement in multiple arteries is not possible with conventional TCD, the accuracy with which the flow distribution over bifurcations can be obtained is limited by the natural temporal variations in the blood flow caused by for example the autoregulation. Although power motion-mode TCD (PMD/TCD) improves the window detection and handler-dependency, and facilitates the measurement of multiple arteries (Moehring and Spencer, 2002), a method which allows the measurement of both the vascular geometry and flow is preferred.

Phase-Contrast MRA does facilitate simultaneous measurement in multiple arteries provided one common plane of measurement, perpendicular to all arteries of interest can

be defined. However, while this technique has been successfully applied to the large afferent arteries (Rayz et al. (2010), table 10 in Marzo et al. (2011)), the more tortuous and complex geometry further down the arterial tree does not usually meet this condition (Marzo et al., 2011). Although the 4D MRI used to measure local 3D velocity fields does not require this plane definition, the flow distribution over the outlets cannot currently be measured due to the limited spatial and temporal resolution.

Densitometry relies on the injection of a radio-opaque contrast agent to visualise the arterial lumen. As this contrast agent is transported by the blood, the spatial and temporal changes in attenuation contain information about the blood flow. Densitometric methods, elaborately reviewed by Shpilfoygel et al. (2000), can be subdivided into two groups: tracking algorithms and computational methods (table 1.3).

The simplest algorithms are based on bolus tracking via time-intensity curves (TICs) at several sites along an artery. The difference in arrival time provides the flow since the distance can be extracted from the 3D-RA data. However, this method has proven to be unreliable in pulsatile flows (Shpilfoygel et al., 2000). Similarly, the distance-intensity curves (DICs), i.e., the spatial distribution of the contrast agent, in two subsequent images can be correlated where the spatial shift of the DIC provides an estimate for the flow. Tracking of just the bolus edge yields an overestimation of the volumetric flow during contrast inflow and underestimation during the washout phase due to the velocity profile with high velocities in the core and low velocities in the boundary layer. The same drawback is observed in the optical flow methods, a subgroup of computational methods using the mass conservation law to estimate the time-dependent flow rate from temporal and spatial derivatives of the contrast agent concentration. Because of the usage of derivatives, these methods are highly sensitive to noise (Shpilfoygel et al., 2000; Waechter et al., 2008).

Most densitometric methods presented in literature rely on 2D planar data, while 3D-RA is commonly used in the diagnosis and treatment planning of pathologies concerning the cerebral vasculature. Furthermore, using 2D data only does not provide for correction of artifacts introduced by projecting 3D data on a 2D plane. A combination of 2D and 3D data as proposed by Schmitt et al. (2005) requires patient-motion compensation due to the increased measurement time. Therefore, a method to extract flow directly from the 3D-RA data would be preferable (Waechter et al., 2008).

All videodensitometric methods share one major drawback as they all rely on the injection of contrast agent, thereby altering the flow to be measured (Spiller et al., 1983). Therefore, measuring absolute flow rates might be unreliable. As MRI allows the non-invasive measurement of the 3D geometry as well as local flow measurements, this would be the preferred method if the spatial resolution issue were to be resolved.

## 1.4 Computational techniques

Segmentation of the MRA or 3D-RA data provides the cerebral arterial tree, of which a small longitudinal section of interest can be selected for the 3D simulations of the local

**Table 1.3:** Overview of the videodensitometric methods as described in Shpilfoygel et al. (2000), and the drawbacks most relevant for flow measurements in the cerebral circulation.

TRACKING METHODS		
TIC based		Inaccurate in pulsatile flow conditions
DIC based:	Bolus edge	Overestimation due to deviation from plug velocity profile
	Small bolus	Complicated, flow-disturbing injection protocol
	Curve fitting	Upper limit velocity by FOV
Parametric image		Sensitivity to noise
Droplet tracking		Risk of embolism in peripheral circulation
COMPUTATIONAL METHODS		
Indicator-dilution		Inaccurate in pulsatile flow
First-pass distribution		Not suitable for arteries
Inverted continuity		Only valid on bolus edge
Inverse mass transport		Computationally expensive
Optical flow methods		Reduced accuracy by diffusion and high velocities
Fluid continuity		Requires smooth changes of contrast agent concentration

velocity field. Commonly, the arterial wall is assumed rigid as the effect of wall motion on the 3D intra-aneurysmal velocity field is small compared to those of the variations in geometry or boundary conditions (Sforza et al., 2010). However, arterial wall movement has shown to affect the wall stress and the velocity field in some cases (Torii et al., 2007). If a strong jet impinges on the arterial wall the local wall shear stress is reduced when wall distensibility is taken into account, while a change of wall shear stress distribution is observed when the blood flows straight into the aneurysm. Furthermore, in nearly stagnant intra-aneurysmal flows the pressure-induced wall motion causes a local flow, thereby raising the minimum wall shear stress (Torii et al., 2009).

Even ignoring the numerical problems involved in fluid-structure interaction models, taking into account wall motion is far from straightforward. First, the tissue in which the arteries are embedded should be considered (Anor et al., 2010). Secondly, the arterial wall is a heterogeneous layered structure, which complicates the formulation of an adequate constitutive model. Mostly, its non-linear behaviour is approximated with homogeneous quasi-linear models. A more realistic material model was developed by Holzapfel et al. (2002). However, more complicated models introduce more unknown parameters, many of which currently cannot be measured *in vivo*. Next, the material properties of the arterial wall show a large inter-patient variability. Finally, the reference (unloaded) geometry is unknown, although reverse analysis could be applied (Speelman et al., 2009). A more realistic approach is to impose image-based wall motion, circumventing the need to define the mechanical properties of the wall (Dempere-Marco et al., 2006; Zhang et al., 2009). It should be noted, however, that incorporating models describing the multi-layered, non-homogeneous wall allow assessment of the role of wall-adaptation in aneurysm growth (Watton et al., 2011).

Another complicating factor is the non-Newtonian blood rheology. For shear rates higher than  $100 \text{ s}^{-1}$ , as found in large arteries, the Newtonian fluid assumption often adopted

in numerical studies seems reasonable (Anor et al., 2010). Especially in complex geometries however, shear thinning may reduce blood recirculation and the strength of vortices present. Furthermore, the low velocities observed in some aneurysms may be altered by neglecting the non-Newtonian behaviour of blood, which is important when adhesion or thrombus formation are of interest (Rayz et al., 2010).

Apart from the constitutive complexity given above, appropriate boundary conditions need to be prescribed at the cut-off surfaces of the arterial segment considered. The boundary conditions are often based on patient-generic data, e.g., averaged flow curves from healthy volunteers or patient-generic 1D wave propagation models. These 1D models are computationally less expensive than full 3D models, and therefore more suitable to describe a large part of the arterial tree. Although the connectivity of the vasculature is commonly patient-generic, scaling factors based on patient characteristics such as age, height and weight aim to provide more representative flow waveforms (Reymond et al., 2009). The boundary conditions for the 1D model are based on (averaged) generic data (Reymond et al., 2009) or derived from the vascular geometry (Alastruey et al., 2007b). The latter is based on the fact that arteries adapt such that a target wall shear stress, i.e., flow, is reached (Murray, 1926), although the absolute targeted value varies throughout the body (Dammers et al., 2003). Variations of boundary conditions based on geometry include the structural tree (Olufsen, 1999; Steele et al., 2007), tapered tube (Azer and Peskin, 2007) and windkessel models with the resistance based on the outlet radius (Stergiopoulos et al., 1992; Alastruey et al., 2007b). The 1D model can be extended with heart models (Reymond et al., 2009), wall adaptation models (Chatziprodromou et al., 2007) and autoregulation models (Aaslid et al., 1989; Aaslid, 2006; Alastruey et al., 2007a) in order to enable modelling of special circumstances to increase the understanding of the cerebral circulation. The 1D domain can be coupled directly to the 3D domain via a 0D element to avoid reflections on the transition from one domain to the next (Passerini et al., 2009). The more simple uncoupled approach is to prescribe the flow and pressure curves extracted from the 1D model at the positions corresponding to the boundaries of the 3D model (Reymond et al., 2009).

At the truncated arteries of the 3D segment, either pressure or flow curves can be prescribed. Ujiie et al. (1999) observed a significant effect of the flow ratio of the distal branches in animal models of cerebral aneurysms, so the prescribed boundary conditions should result in a realistic flow distribution. If the outlets are considered stress-free (e.g., Grinberg et al. (2001)), the relative resistance of each outlet artery included in the vascular segment determines the flow distribution rather than the peripheral vasculature. Although prescribing the pressure at each outlet allows a more representative flow distribution based on the peripheral circulation, small errors in the pressure would significantly affect this flow distribution. Therefore, prescribing the flows is more reliable in this type of problem. As the flow rates at the outlets currently cannot be measured accurately *in vivo* (see section 1.3), a 1D model could be used to determine the flow curves throughout the cerebral circulation.

A challenging problem is the *in vivo* validation of CFD models describing the intra-aneurysmal velocity field. Although 4D pc-MR is not accurate enough to measure derived quantities directly, comparisons of the measured velocity fields and those obtained

with patient-specific models look promising (Rayz et al., 2008; Isoda et al., 2010). This might allow a more thorough validation, which is needed in order to reduce the distrust amongst clinicians before the models can be applied to clinical practice (Singh et al., 2009).

## 1.5 Objective

The aim of this research is to investigate how the reliability of the model-based representation of the velocity field in the aneurysmal sac can be improved. To this end, a work-flow is proposed such that patient-specific boundary conditions for the 3D segment of interest can be estimated without the need for additional invasive procedures. This is facilitated by a 1D wave propagation model based on patient-specific geometry and boundary conditions measured non-invasively in more accessible regions. Furthermore, the suggested post-processing methods allow automated quantitative analysis of the 3D intra-aneurysmal velocity field. Such a protocol offers improved statistical reliability owing to the increased number of patients that can participate in studies aiming to identify parameters of interest in aneurysm stability assessment.

## 1.6 Outline

Automated 3D analyses allow processing of the number of data sets needed to identify parameters predictive for rupture. For example, vortex identification methods facilitate the quantification of the vortex dynamics of intra-aneurysmal flow. In chapter 2 a vortex identification method is applied to the velocity field in an idealised aneurysm model, which is validated with particle image velocimetry experiments. Though patient-specific geometry is commonly used for 3D segments, the 1D model on which the boundary conditions for the 3D model are based is usually patient-generic. A full patient-specific model would require patient-specific geometry and boundary conditions for the 1D model of the arterial tree. In chapter 3, a patient-specific geometry is extracted from a patient data set. The resulting flow pulses at the boundaries of the 3D segment of interest are compared to those obtained with a patient-generic geometry. The influence of these different boundary conditions on the 3D intra-aneurysmal velocity field is evaluated in chapter 4 by prescribing the end-diastolic flows extracted from the 1D models. The patient-specific boundary conditions should be based on pressure and flow measurements. Some methods to estimate volumetric flow rates require the injection of a contrast agent. In chapter 5, the effect of this injection on the flow of interest is assessed. In chapter 6, pressure measurements in the internal carotid are used to evaluate the variability of pressure waveform and its effect on the boundary conditions for the 1D model. Finally, a protocol for full patient-specific modelling is discussed in chapter 7, with which a reliable representation of the intra-aneurysmal velocity fields in a large patient study can be obtained.



## CHAPTER TWO

# On automated analysis of flow patterns in cerebral aneurysms based on vortex identification<sup>1</sup>

---

It is hypothesised that the risk of rupture of cerebral aneurysms is related to geometrical and mechanical properties of the arterial wall as well as to local haemodynamics. In order to gain better understanding of the haemodynamical factors involved in intra-aneurysmal flows, a thorough analysis of the 3D velocity field within an idealised geometry is needed. This includes the identification and quantification of features like vortices and stagnation regions. The aim of our research is to develop experimentally validated computational methods to analyse intra-aneurysmal vortex patterns and, eventually, define candidate haemodynamical parameters (e.g. vortex strength) that could be predictive for rupture risk. A computational model based on a standard Galerkin finite element approximation and an Euler implicit time integration has been applied to compute the velocity field in an idealised aneurysm geometry and the results have been compared to Particle Image Velocimetry (PIV) measurements in an *in vitro* model. In order to analyze the vortices observed in the aneurysmal sac, the vortex identification scheme as proposed by Jeong and Hussain [JFM. 285(1995)69] is applied. The 3D intra-aneurysmal velocity fields reveal complex vortical structures. This study indicates that the computational method predicts well the vortex structure that is found in the *in vitro* model and that a 3D analysis method like the vortex identification as proposed is needed to fully understand and quantify the vortex dynamics of intra-aneurysmal flow. Furthermore, such an automated analysis method would allow the definition of parameters predictive for rupture in clinical practice.

---

<sup>1</sup> *Reproduced from:* G. Mulder, A. C. B. Bogaerds, P. M. J. Rongen, F. N. van de Vosse (2009). On automated analysis of flow patterns in cerebral aneurysms based on vortex identification. *Journal of Engineering Mathematics*, 64:391-401.

## 2.1 Introduction

Cerebral aneurysms are localised pathological dilatations of cerebral arteries, most commonly found in the circle of Willis. In the general population, approximately 2 – 5% is likely to harbour these aneurysms (Mizoi et al., 1995; Krex et al., 2001), which have an annual rupture risk of approximately 1% (Mitchell et al., 2006a). Rupture of a cerebral aneurysm results in subarachnoid hemorrhage (SAH), with a mortality rate of 40 – 50% (Juvela et al., 2001; van Gijn and Rinkel, 2001).

The rupture risk is determined by the loading state and the mechanical properties of the arterial wall, which are both related to the haemodynamics as illustrated in figure 2.1. The loading state, i.e. wall stress (*i*), depends on the mechanical properties of the arterial wall (*j*), the aneurysmal geometry (*f*) and the intra-aneurysmal pressure (*e*). The pressure is determined by the flow (*b*) through the parent artery and the peripheral resistance (*a*). The influence of the peripheral circulation is not considered in most Computational Fluid Dynamics (CFD) models since they focus on an isolated rigid aneurysm geometry (Cebal et al., 2005b; Castro et al., 2006c). Coupling the 3D model to a 1D model of the global cerebral circulation would allow prescribing more realistic boundary conditions. Furthermore, autoregulation controlling the resistance provides feedback of the pressure and flow. The local geometry, which slightly varies with the pressure due to the distensibility of the arterial wall, has a major effect on the intra-aneurysmal flow patterns (*b*) (Cebal et al., 2005a). However, this geometry is also affected by the flow via biochemical cascades that control the adaptation of the arterial wall (mechano-transduction) (Malek and Izumo, 1995; Wentzel et al., 2003). The flow-induced wall shear rate (*c*) is known to affect particle residence times (*d*). Moreover, changes in shear stress (*c*) magnitude and direction alter the permeability of the arterial wall and the transport (*d*) between the lumen and wall (Friedman and Fry, 1993). Endothelial cells are sensitive to these haemodynamical changes, resulting in the activation of biochemical factors (*g*) that control the adaptation of the arterial wall (*h*). Altogether, this adaptation may become pathological and may cause weakening of the arterial wall, which, under the influence of wall stress, may result in aneurysm growth. In the event of rupture (*k*), the mechanical properties of the arterial wall have been altered by the degradation process such that the stress in the wall exceeds its strength.

One would prefer to base the decision whether or not to treat an aneurysm on the balance between the risk of rupture and the risk related to the treatment itself. However, the risk of rupture is not easily determined, since there currently are no proven methods for *in vivo* measurements of flow, pressure or mechanical properties of the wall in cerebral aneurysms. Several attempts have been made to find a direct correlation between geometry and risk of rupture, using parameters like size of the dome and aspect ratio (Beck et al., 2006; Dickley and Kailasnath, 2002; Ohashi et al., 2004). However, no conclusive critical size parameter could be defined based on those studies. Currently, the decision whether treatment is recommended is based primarily on the size of an aneurysm, although this remains controversial.

Since rupture risk is also related to haemodynamical factors, intra-aneurysmal velocity

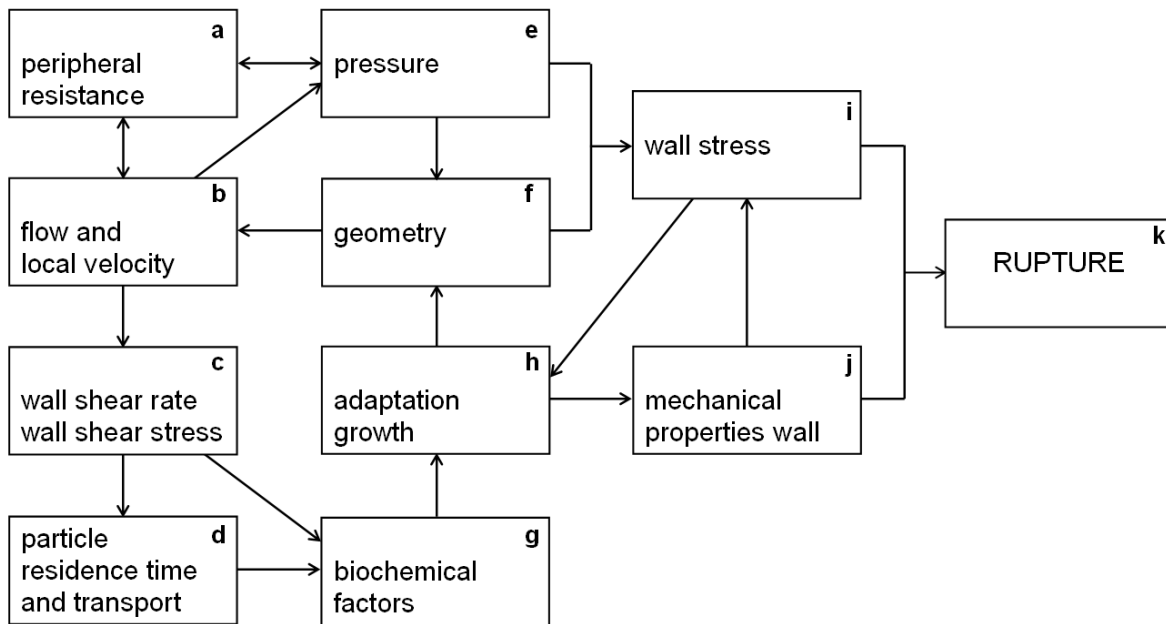


Figure 2.1: Schematic representation of the factors involved in aneurysm rupture.

fields in idealised as well as patient-specific models have been analyzed in various studies (Liou and Liou, 1999; Steinman, 2002; Chatziprodromou et al., 2007). Since several methods for *in vivo* flow measurements in cerebral arteries are in development, it seems realistic to use these flow measurements as input for numerical models of which the geometry has been determined by e.g. CT imaging or 3D Rotational Angiography (3D-RA). In general, the intra-aneurysmal velocity fields show complex 3D flow patterns containing inflow jets, vortices, and stagnation regions. A quantitative comparison of biplane DSA images recorded with a high frame rate and numerical results shows similar flow patterns, which suggests that these major features are captured by the CFD models (Cebal et al., 2007). Cebal et al. (2005b) suggested a direct relation between intra-aneurysmal flow patterns and rupture risk. The flow patterns in the aneurysmal sac of patient-specific geometries were characterised based on the stability of inflow jet and the number of vortices. Unstable flow patterns could be related to aneurysm progression and rupture due to elevated oscillating stresses or larger regions of elevated mean wall shear stresses. Stable patterns may provide a more suitable environment for arterial adaptation mechanisms to counterbalance the stresses, resulting in safer aneurysms. Indeed, simple stable flow patterns, large impingement regions and large jet sizes are more commonly found in unruptured aneurysms, whereas disturbed flow patterns, small impingement regions and narrow jets were found more frequently in ruptured aneurysms. However, further research evaluating more patient-specific geometries is needed to confirm these preliminary results. In order to enable a more thorough and efficient analysis of the intra-aneurysmal velocity fields, these features should be identified in an automated fashion. Vortex and stagnation region identification allow a more accurate analysis of patient data, and therefore, are believed to enhance our understanding of the flow patterns observed in various geometries and sites at which rupture occurs most frequently.

In this research, a vortex identification scheme as proposed by Jeong and Hussain (1995) has been implemented in order to evaluate the intra-aneurysmal velocity field in an idealised CFD model of a lateral aneurysm with a curved parent artery. The velocity field computed with this model is compared to the velocity field measured with Particle Image Velocimetry (PIV) in order to validate the observed vortex structure and check for possibly missed transitional flow features. Obviously, the geometry of both the parent artery and aneurysm have a high impact on the flow patterns, resulting in e.g. underestimation of the wall shear stress and complexity of the flow pattern in idealised geometries (Castro et al., 2006a,b). However, the rigid-walled idealised model is more suitable for examining the value of such an identification scheme in the analysis of aneurysmal flow patterns. Furthermore, this paper argues the commonly employed method of reviewing a single cross-section in the analysis of the complex 3D intra-aneurysmal flow.

Eventually, this research should lead to a more accurate method to estimate the risk of rupture of cerebral aneurysms. When accurate *in vivo* measurement of blood flow in the, frequently small, parent arteries becomes possible, the shear rate experienced by the endothelial cells covering the aneurysmal wall can be derived. The response of those endothelial cells leads to adaptation, or, in aneurysms, degradation of the arterial wall. Hence, patient-specific CFD modeling will become a valuable tool in risk of rupture assessment when models describing the relation of this degradation process to the haemodynamics become available. In clinical practice however, the flow analysis should be based on automated methods like the vortex identification method presented in this study.

## 2.2 Materials and Methods

### 2.2.1 CFD

In general, the flow characteristics in lateral aneurysms depend on the geometrical configuration of the aneurysm in relation to the parent vessel, the size of the neck, the volume of the aneurysm and the haemorheological properties. The geometry used here (fig 2.2) was based on the geometrical considerations described by (Parlea et al., 1999).

The intra-aneurysmal velocity field is obtained by solving the momentum equation

$$\rho \left\{ \frac{\partial v}{\partial t} + v \cdot \nabla v \right\} = -\nabla p + \nabla \cdot \tau + f \quad (2.1)$$

and the incompressibility constraint:

$$\nabla \cdot v = 0, \quad (2.2)$$

on the 3-dimensional domain  $\Omega$  ( $\Omega \subset \mathbb{R}^3$  constrained by the closed boundary  $\Gamma$ ). Here,  $\rho$  denotes the constant density,  $v$  the velocity vector,  $f$  a body force defined per unit of volume,  $p$  the hydrostatic pressure and  $\tau$  the extra stress tensor. Since Newtonian fluid

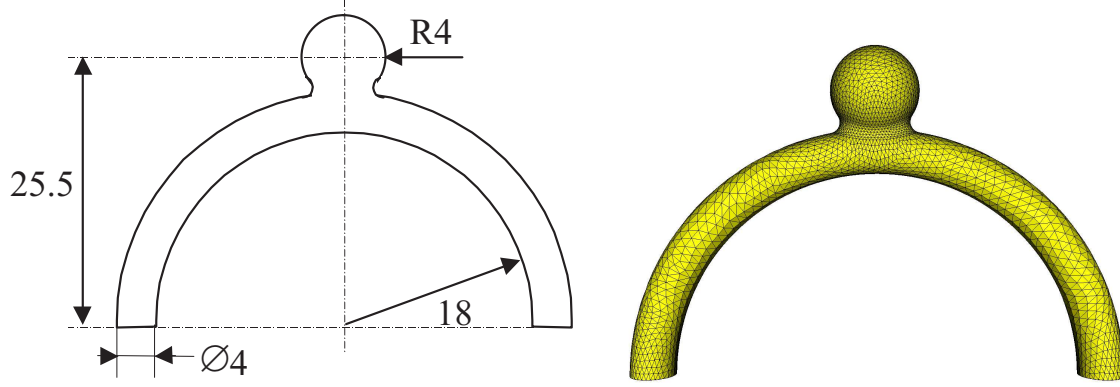


**Figure 2.2:** Geometry of the lateral aneurysm model in [mm]. Measured from the neck, the aneurysm height and semi-axis height equal 7 and 3 mm respectively, while the neck width is 3.9 mm. The 3D finite element mesh generated with Patran (MSC Software) consists of 39405 tetrahedron elements, with a total of 152095 degrees of freedom.

behavior is assumed, the relation for the extra stress tensor reads:

$$\tau = 2\eta D, \quad (2.3)$$

with  $\eta$  the dynamic viscosity and  $D = (\nabla v + \nabla v^T)/2$  the rate of deformation tensor. Substitution of (2.3) in (2.1) while neglecting body forces like gravity results in the well-known incompressible Navier-Stokes equations. Together with the appropriate boundary conditions on  $\Gamma$  and suitable initial conditions, the Navier-Stokes equations will result in a unique solution for  $v$  and  $p$  when the Reynolds numbers are sufficiently low. The weak formulation of the Navier-Stokes equations is found after definition of the appropriate Sobolev space of functions with 1<sup>st</sup> order square integrable derivatives on  $\Omega$  ( $W = \{w \in [H_0^1(\Omega)]^3\}$ ). Those derivatives vanish on  $\Gamma$  where Dirichlet boundary conditions are prescribed, as well as  $Q$ , the Lebesgue space of square integrable functions on  $\Omega$  ( $Q = \{q \in L^2(\Omega), \int_{\Omega} q d\Omega = 0\}$ ). In that case, the weak form is given by

$$\int_{\Omega} \rho w \cdot \left\{ \frac{\partial v}{\partial t} + v \cdot \nabla v \right\} d\Omega + \int_{\Omega} \eta \nabla w^T : \nabla v d\Omega - \int_{\Omega} p \nabla \cdot w d\Omega = \int_{\Gamma} w \cdot (-pn + \tau \cdot n) d\Gamma \quad \forall w \in W, \quad (2.4)$$

$$\int_{\Omega} q \nabla \cdot v d\Omega = 0 \quad \forall q \in Q. \quad (2.5)$$

The variational form is solved using Crouzeix-Raviart type finite elements. These elements apply second order continuous interpolation for the fluid velocity and a linear discontinuous basis for pressure interpolation. In this work, the domain  $\Omega$  is discretised using tetrahedral elements with 15 nodal points. The 3-dimensional computational grid is shown in figure 2.2.

At the arterial wall and the wall of the aneurysm, no-slip boundary conditions were applied. At the proximal side of the parent artery a sinusoidal start-up Poiseuille profile was prescribed, reaching a steady state limit after 1 second. At the distal side of the parent artery, the normal component of the stress vector, and all in-plane velocity components, were prescribed as equal to zero. Based on the data reported by Liou and Liou (2004), Narracott et al. (2003) and Rudin et al. (2002), the mean blood flow through the 4 mm parent artery was chosen to be  $3.6 \text{ ml s}^{-1}$ . The radius of the parent artery, the mean blood velocity, and the blood viscosity ( $3.5 \text{ mPa}\cdot\text{s}$ ) result in a Reynolds number ( $\text{Re} = \rho VR/\eta$ ) of  $\text{Re} = 165$ .

Temporal discretisation of the Navier-Stokes equations was achieved using the implicit Euler scheme, while Newton's method was used for the linearisation of the convective terms within each time step. The iterative method used to solve the linearised set of equations is Bi-CGStab with an incomplete LU decomposition pre-conditioner (Segal, 2000).

### 2.2.2 Vortex identification

The vortex identification method developed by Jeong and Hussain (1995) is based on the second largest eigenvalue of  $D^2 + \Omega^2$ , with  $D$  and  $\Omega = (\nabla\mathbf{v} - \nabla\mathbf{v}^T)/2$  the deformation and rotation tensor, respectively. After substitution of the vorticity equation, the gradient of the Navier-Stokes equations read

$$\frac{\partial D}{\partial t} + (\mathbf{v} \cdot \nabla)D + D^2 + \Omega^2 = -\frac{1}{\rho}\nabla(\nabla p) + \frac{\eta}{\rho}\nabla\nabla^2\mathbf{v}. \quad (2.6)$$

The Hessian of the pressure  $H_p = \nabla(\nabla p)$  provides information about local pressure minima within the flow. In general, pressure gradients can be attributed to local irrotational straining (first two terms of the left hand side of equation 2.6), viscous dissipation (last term on the right hand side) and rotational effects in the vortex cores. Hence, the rotational effects on the pressure gradient are represented in

$$H_p^{\text{rot}} = -\rho(D^2 + \Omega^2). \quad (2.7)$$

In order to find a local pressure minimum due to rotation around the vortex core two negative eigenvalues of  $-H_p^{\text{rot}}$  are required. Hence,

$$\lambda_i = \text{eig}(D^2 + \Omega^2), \quad \text{with } \lambda_2 < 0 \quad (\lambda_1 < \lambda_2 < \lambda_3) \quad (2.8)$$

results in a plane ( $\lambda_2 < 0$ ) that constrain the position of the vortex core(s).

### 2.2.3 Experiment

An *in vitro* model of an aneurysm on a curved parent artery (fig 2.2) was produced out of silicone (Sylgard 184). A stationary pump (Cole-Palmer, Mo.75211-15) was used to produce

a stationary flow with  $Re = 165$ .

A 30 wt% electrolyte solution of calcium chloride and magnesium chloride (ratio 5 : 1) was selected as working fluid, minimising the difference in refraction indices. In order to enable the PIV measurements, the fluid was seeded with silver-coated hollow glass particles with mean particle size  $10 \mu\text{m}$  and density  $1.4 \cdot 10^3 \text{ kg m}^{-3}$  (DANTEC). The particles were illuminated by a continuous argon ion laser (Midwest ILT 5500A; 458 – 515 nm; 300 mJ/s) and recorded by a high-speed video camera (Phantom V9.0).

### 2.2.4 Data acquisition and postprocessing

The three measured planes correspond to plane b, e and h in figure 2.3. The high speed video camera allows high frame rates providing a temporal resolution usually not achieved in PIV. Plane b was measured using a frame rate of 5.4 kHz, while 5 kHz was used for the other planes. Depending on the expected velocities within the measurement plane, either subsequent frames (plane b) or every tenth frame were correlated. The region of interest is imaged on  $570 \times 368$  pixels, and the scaling factor is  $2.5 \cdot 10^{-5}$  m per pixel for plane b and h, whereas it is  $2.9 \cdot 10^{-5}$  m per pixel for plane e.

The velocity field was computed using an adaptive correlation method van der Graaf (2007), which improves the correlation for larger displacements and velocity gradients. In the first incremental step the interrogation areas was  $32 \times 32$  pixels, the result of which is used to pre-shift the interrogation areas in the next incremental step in which the interrogation area size equals  $16 \times 16$  pixels. Furthermore, every step uses a 50% overlap of the interrogation areas to reduce loss-of-pairs.

Various methods are available to identify erroneous vectors which are inevitably present in PIV data even when the experiment is conducted carefully (Westerweel, 1994). In general, detecting erroneous vectors based on temporal information is not reliable since PIV has a rather low temporal resolution (Shinneeb et al., 2004). However, since the measurements were performed with a high frame rate in a stationary flow without any expected transient flow phenomena, the velocity field could be averaged over the 189 measurements performed.

In order to compare the computational and experimental results, the computed velocities were interpolated onto a uniform grid of which the grid size corresponds to the PIV data. Equal Reynolds numbers were used in the experiment and computation. Furthermore, several cross-sections (fig 2.3) were visualised for a more detailed analysis of the 3D velocity field obtained with the CFD model.

## 2.3 Results

The profiles in figure 2.4 clearly show the slanted profile in the curved parent artery, with higher velocities and velocity gradients near the outer wall. The aneurysmal neck shows a high velocity gradient where the aneurysmal vortex and the flow in the parent

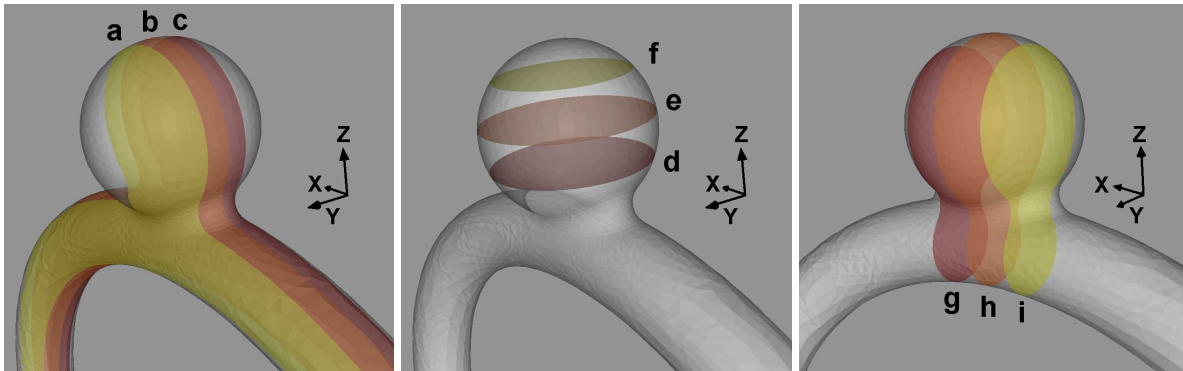


**Figure 2.3:** The velocity fields are visualised on 9 cross-sections, of which the numbering corresponds to the numbering in figure 2.5 and 2.7.

artery meet. In order to estimate the quantitative agreement of PIV and CFD, the discrete integrals of the velocity magnitude over the lines shown in figure 2.4) are determined. In the parent artery (below the neck as indicated by the arrow in figure 2.4), this integral is approximately 8% higher in PIV relative to CFD. In the aneurysm however, the difference is approximately 2% in both directions.

The contours in figure 2.4 represent the magnitude of the in-plane velocity determined with CFD and PIV. The measured velocities are slightly higher than the computed velocities. Both velocity fields in plane b (fig 2.4) depict a single vortex structure in the aneurysmal sac, with the vortex center located distally to the aneurysm center. Furthermore, the velocities and velocity gradients near the distal wall are much higher compared to those at the proximal wall. Plane h (fig 2.4) reveals secondary flow patterns in the curved parent artery, although the velocity in the center of the parent artery is not captured by the PIV measurements. The flow patterns (e.g. vortex core in the top of the aneurysmal sac) observed in the velocity field obtained with PIV do not appear in the computed velocity field. In plane e (fig 2.4) however, the features show good agreement.

While with PIV only three planes are measured, CFD allows a more detailed analysis of multiple planes in the 3D velocity field. Figure 2.5 shows the velocity field in the cross-sections defined in figure 2.3, with the contours representing the out-of-plane velocity. The velocity fields in figure 2.5a-c depict a single vortex structure as described above.

Inflow occurs mainly at the distal lip of the neck close to the plane of symmetry (fig 2.5b and d). As the inflow jet meets the distal lip a portion of the flow is directed into the aneurysm, whereas most fluid follows the flow in the parent artery. This is clearly visible from the out-of-plane velocity in two cross-sections in the aneurysmal neck (fig 2.6), just above and underneath the site where the inflow jet meets the distal lip. At the bottom of the neck the velocity at the distal lip is directed towards the parent artery (red), while the cross-section at the top of the neck shows flow into the aneurysm (white). The inflow jet widens as it spreads over the distal wall, initiating two small vortex cores on each side of the symmetry plane at the distal side of the aneurysm (fig 2.5d and e). In the upper part of the aneurysm the fluid follows the wall (fig 2.5f).

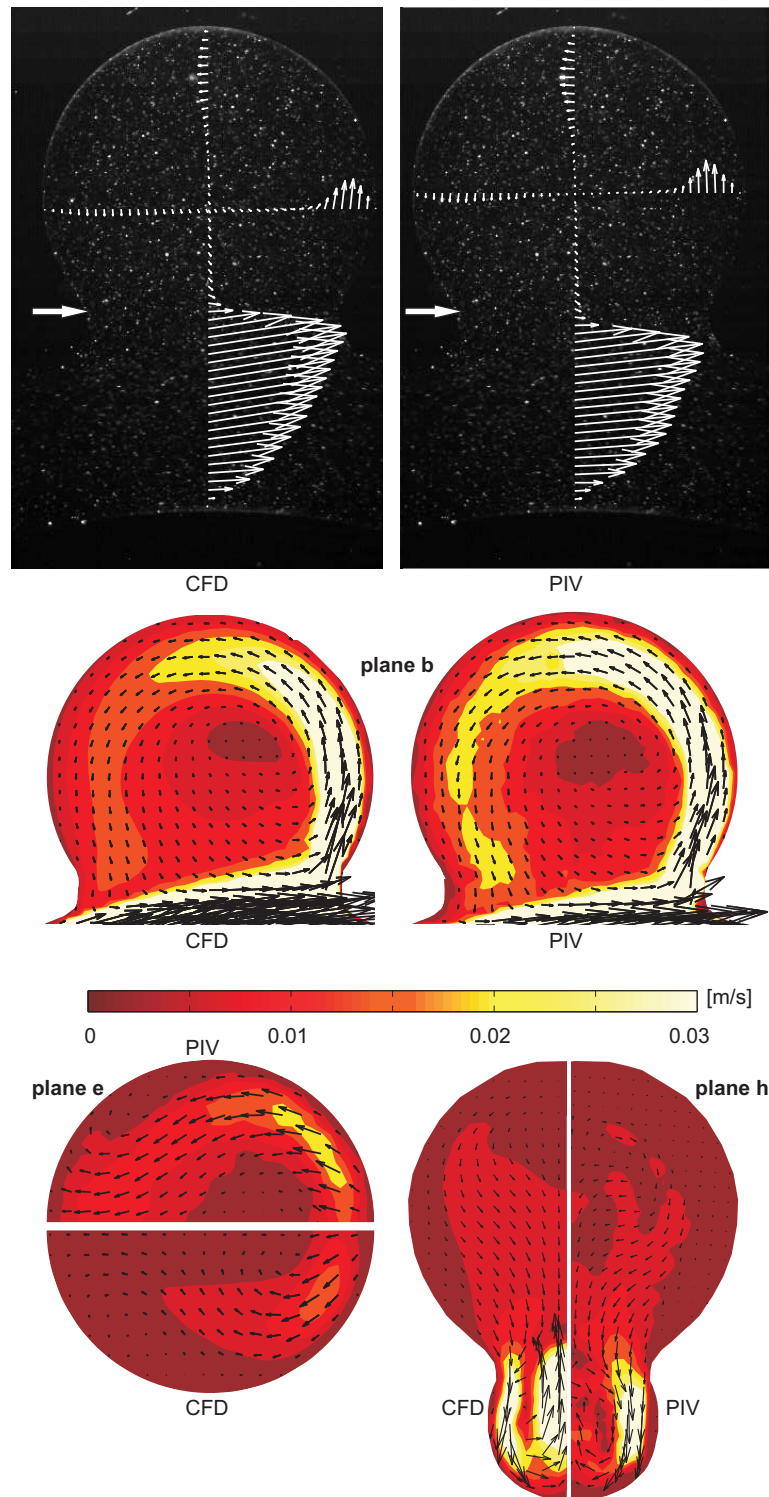


**Figure 2.4:** The absolute in-plane velocity (in  $\text{ms}^{-1}$ ) determined with CFD and PIV in plane b, plane e, and plane h, as defined in figure 2.3. The velocity vector scaling in plane e and h is a factor 3 higher for visualisation purposes. The flow in the parent artery, as shown in the profiles (top), is from left to right.

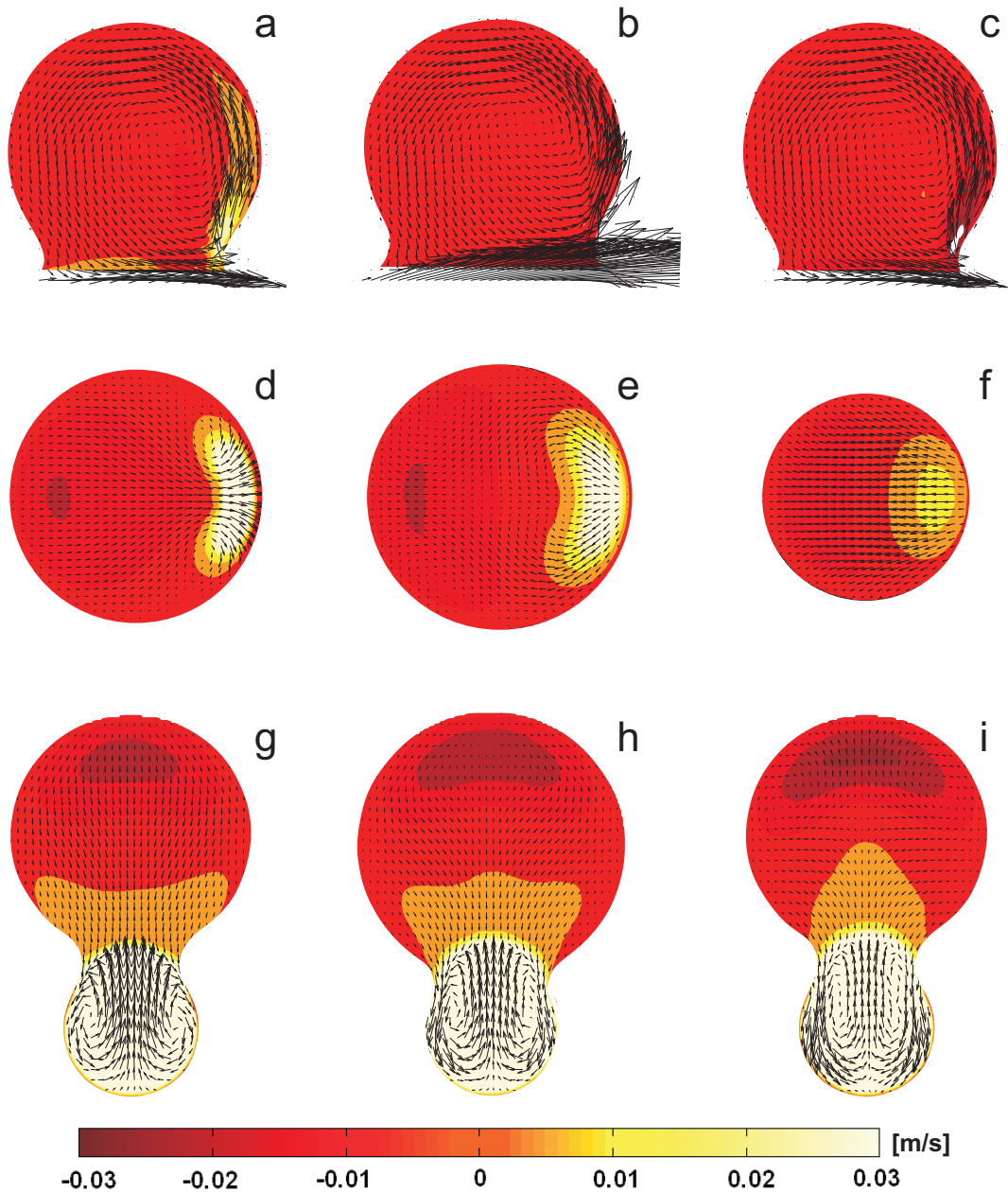


**Figure 2.5:** The velocity field within several cross-sections, of which the numbering is as introduced in figure 2.3. The contours represent the out-of-plane velocities (in  $\text{ms}^{-1}$ ). The flow in the parent artery is from left to right in a-f, while the viewing direction in g-i is in the direction of the flow.

Figure 2.5g-i depicts a shift of the secondary flow pattern in the parent artery towards the aneurysm as it proceeds along the neck, allowing outflow along the wall (see also figure 2.6). In the proximal cross-section (fig 2.5g) the flow follows the aneurysm wall, while the velocity is directed towards the symmetry plane in the middle of the aneurysm (fig 2.5h). In the lower part of the aneurysm, the velocity is re-diverted towards the wall as it meets

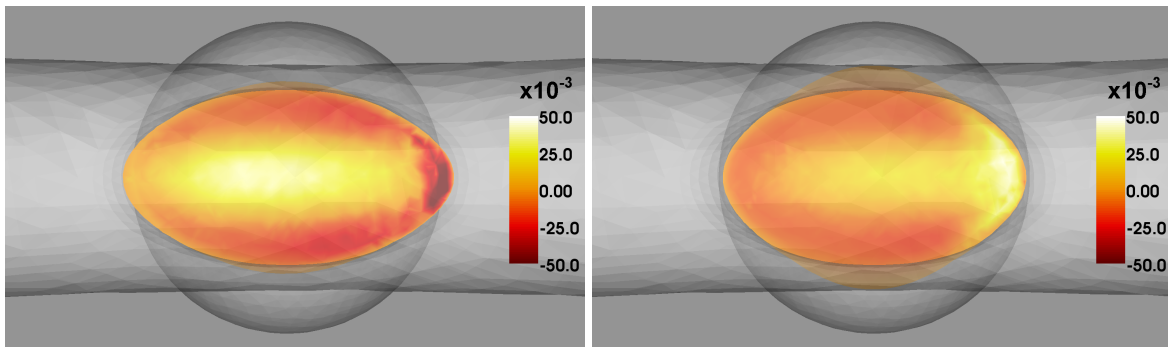


**Figure 2.6:** Bottom view of the out-of-plane velocity (in  $\text{ms}^{-1}$ ) in the lower part of the neck (left) and 0.3 mm higher, at the upper part of the neck (right). Since these cross-sections are localised just above and underneath the site where the inflow jet meets the distal lip of the neck, the light area at the distal lip in the top cross-section represents the inflow in the aneurysms while the red area in the lower cross-section represents the fluid that goes straight back into the parent artery and never entered the aneurysm. Inflow occurs mainly in the symmetry plane, whereas outflow occurs along the wall. The flow into the parent artery is from left to right.

the flow in the parent artery. Figure 2.5i shows the cross-section in close proximity to the vortex center, which depicts a complex flow pattern. In the lower part the flow is directed towards the parent artery, whereas it is directed towards the top in the upper part of the aneurysm. As the fluid meets the top of the aneurysm it spreads along the wall, only to be directed towards the symmetry plane just below of the vortex center. This results in yet another set of small vortex cores on each side of the plane of symmetry.

The contours in figure 2.7 represent the area in which the second largest eigenvalue,  $\lambda_2$ , is smaller than zero. The velocity fields in figure 2.5a-c show a single vortex, whereas the vortex identification depicts a more complex vortex structure (fig 2.7a-c). When considering the velocity fields in other cross-sections, it becomes evident that there are other smaller vortex cores present as described above (fig 2.5d,e and i). This clearly shows the complexity of the 3D vortex structure, in which smaller vortices interact with each other. Altogether, the volume containing the vortex core is a doubly curved structure where both curvatures have the same sign, resulting in an indented sphere.

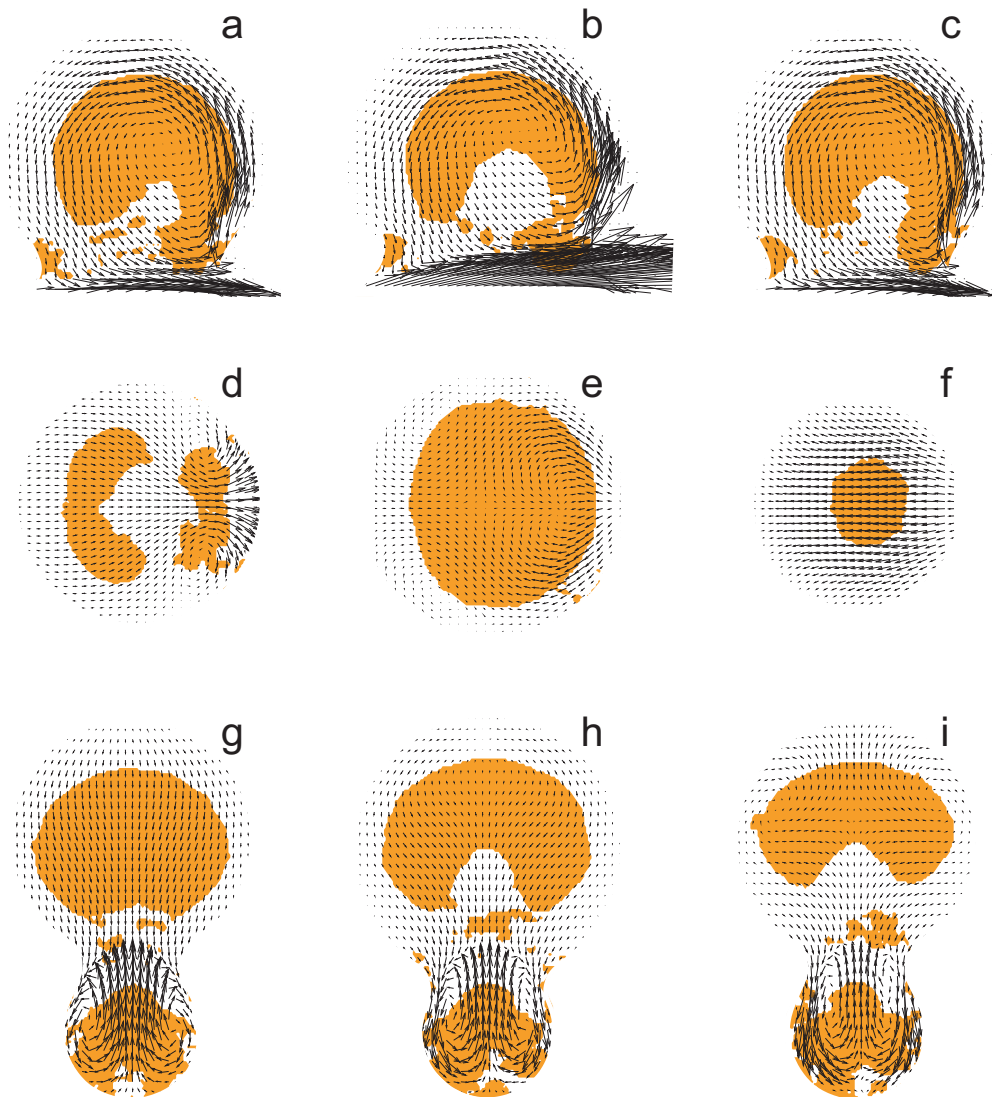


**Figure 2.7:** Velocity vectors and vortex structures in the cross-sections defined in figure 2.3. Detection of the vortex core is achieved using a vortex identification scheme based on the second eigenvalue method developed by Jeong and Hussain (1995).

## 2.4 Discussion and conclusions

It is well-known that haemodynamical forces are involved in aneurysm growth and rupture. Unfortunately, intra-aneurysmal flow can currently not be determined *in vivo*. CFD is a powerful tool in the analysis of intra-aneurysmal flow patterns, in both idealised and patient-specific geometries. However, several assumptions have to be made in the modeling of this pathology, as in all biological systems. First of all, Newtonian behavior

was assumed when modeling the blood flow, which is reasonable for the high flows observed in large arteries. Within the aneurysmal sac however, velocities may become very low which might introduce the need for a more realistic viscosity model. Furthermore, a rigid wall is assumed, which obviously is not the case *in vivo* (Meyer and Riederer, 1993). The compliance of the vessel wall might be incorporated in the model, but that would require knowledge of the pressure and mechanical properties of the wall. These properties can not be measured directly *in vivo*. However, as the resolution of visualisation modalities increases, it might become possible to derive them from wall motion and pressure measurements in the future. These pressure measurements would also be relevant when determining appropriate boundary conditions, since the stress-free out-flow boundary condition used here will not suffice when wall compliance is taken into account. Altogether, the number of unknowns introduced when the wall compliance is taken into account may cause this more complex model to be less accurate.

The velocity fields obtained with the CFD model are compared to those measured with PIV in three cross-sections (fig 2.3). In PIV measurements the high out-of-plane velocities are a major complication, especially if the in-plane velocities are relatively low. Hence, the measurements in-plane b were expected to be most accurate. Indeed, the magnitude of the measured intra-aneurysmal velocities are only 2% higher than the computed velocities. Since the PIV settings were based on the velocities in aneurysm, a larger difference is observed in the parent artery. However, the slanted profile in the parent artery (fig 2.4) is consistent with theoretical considerations of flow in curved tubes (Dean, 1927, 1928).

In plane e and h the out-of-plane velocities are higher than the in-plane velocities, especially near the distal side of the aneurysm and in the parent artery. Still, PIV captures the secondary flow pattern along the wall of the parent artery, whereas the out-of-plane velocity is too high in the center of the parent artery. The characteristics in the measured velocity field in plane h (fig 2.4) resembles the velocity field in plane i (fig 2.5). For plane e and h, the flow patterns observed 1 mm next to the plane considered differ significantly, whereas this is not the case for plane b. Hence, when measuring plane e and h, a slight deviation in the positioning of the laser sheet, and averaging of the velocities over the thickness of the laser sheet, influence the resulting velocity field.

As could be expected based on the low Reynolds number, no transitional flow or flow disturbances are observed in the velocity field obtained with PIV. Therefore, the Euler implicit time integration used in the CFD model is able to describe the steady state limit of the flow. Considering the similarities between the characteristics of the measured and computed velocity fields, it seems that the CFD model describes the velocity fields in the aneurysm and its parent artery correctly. Since this CFD method has been used successfully in other applications (van de Vosse et al., 2003) and the velocity fields obtained with PIV and CFD show the same characteristics, the CFD model will be used for further analysis of the intra-aneurysmal velocity field.

The intra-aneurysmal velocity fields show a single anti-clockwise vortex, which is consistent with the findings of Liou and Liou (1999). Furthermore, Liou and Liou (1999) reported that the inflow proceeds around the distal lip of the neck close to the plane of symmetry, which is also observed in the velocity field within the plane of symmetry (fig

2.5b) and cross-sections in the neck (fig 2.6). When considering the velocity field within the planes in figure 2.5a-c, one would expect the vortex identification to result in a circle in figure 2.7a-c. The 3D flow pattern, as can be seen in the other cross-sections, results in a more complex vortex core structure due to the presence of multiple interacting vortices. This clearly shows the need of a more advanced analysis method for intra-aneurysmal flow patterns, such as the identification and quantification of features like vortices and stagnation regions.

Cebral et al. (2005a) uses one cross-section to characterise the blood flow patterns in the aneurysmal sac. This may lead to a misinterpretation of the data, since a pattern might appear to be a single vortex in one plane and more complex in the other. This can be observed even in the simplified geometry used here. In pulsatile flow conditions, the location of the vortex cores will shift throughout a cardiac cycle. The smaller vortices observed in figure 2.5d, e and i, if present in pulsatile flow, might have an influence on the oscillating wall shear stress. Therefore, these small vortices may be important in the relation of rupture risk and flow patterns. However, since the major drawback of the vortex identification method used here (Jeong and Hussain, 1995) is the failure to discriminate between different vortex cores that are in close proximity of each other, multiple cores may arise as one vortex structure. Another vortex identification method, e.g. the predictor-corrector method proposed by Banks and Singer (1995), or combination of vortex identification methods, might be more appropriate for this application. The relationship between the vortex structure and rupture risk remains to be established. Moreover, other features, such as stagnation regions, may be relevant as well. The methods to be used should be optimised by the analysis of intra-aneurysmal flow patterns in different idealised geometries, after which patient-specific geometries should be examined in order to identify rupture risk estimators.

## CHAPTER THREE

# Patient-specific modelling of cerebral blood flow: geometrical variations in a 1D model<sup>I</sup>

---

Cerebral aneurysm growth is influenced by haemodynamical factors, which are commonly estimated by means of a Computational Fluid Dynamics (CFD) model of a small 3D patient-specific segment of the arterial tree. Since direct *in vivo* assessment of the boundary conditions for the 3D segment is often not possible, the flow pulses are generally computed with a patient-generic 1D model. The aim of this study is to evaluate the necessity of, and requirements for, full patient-specific modelling, i.e., both geometry and boundary conditions based on patient data. The flow waveforms obtained with several models from literature and a patient-specific geometry of the arterial tree are compared and analysed. By comparing patient-specific and patient-generic models, it is investigated whether different but all reasonable modelling assumptions results in substantial differences in flow distribution. The flow pulses obtained at the boundaries of the arterial segment of interest are significantly affected by the 1D geometry and boundary conditions. The geometry as well as the in- and outflow conditions of the 1D model should be patient-specific, as they significantly influence the flow pulses to be prescribed at the boundaries of the 3D arterial segment.

---

<sup>I</sup> *Reproduced from:* G. Mulder, A. Marzo, A. C. B. Bogaerds, S. C. Coley, P. Rongen, D. R. Hose, F. N. van de Vosse (2011). Patient-specific modelling of cerebral blood flow: geometrical variations in a 1D model. *Accepted for publication in Cardiovascular Engineering and Technology*

### 3.1 Introduction

Haemodynamical factors are believed to play an important role in cerebral aneurysm growth and rupture via the adaptation of the arterial wall (Singh et al., 2010). These factors, such as wall shear stress, may be derived from the intra-aneurysmal velocity field measured directly *in vivo*, or estimated by means of a three-dimensional Computational Fluid Dynamics (3D CFD) model. The intra-aneurysmal velocity field obtained with 3D phase-contrast Magnetic Resonance (pc-MR) angiography shows good qualitative agreement with CFD computations (Hollnagel et al., 2009; Isoda et al., 2010). However, the spatial resolution is limited, resulting in averaging of the velocity over a voxel. This low resolution leads to a loss in accuracy in regions with high velocity gradients, such as near the arterial wall and inflow jets, leading to inaccuracies in derived quantities such as the wall shear stress.

Therefore, *in vivo* measurement techniques and CFD remain complementary tools in cerebral aneurysm research (Isoda et al., 2010). The 3D arterial segment modelled is defined by its geometry and the boundary conditions prescribed at the inlets and outlets. Since the intra-aneurysmal flow patterns are complex (Mulder et al., 2009) and most sensitive to the geometric accuracy of the model (Cebal et al., 2005a), patient-specific geometries have become the standard in cerebral aneurysm studies. In order to improve further the reliability of these models, the focus is shifting from patient-generic boundary conditions (Cebal et al., 2007; Steinman, 2002) towards patient-specific boundary conditions (Marzo et al., 2011). Taking arterial distensibility into account is believed to be less important for the flow patterns in cerebral aneurysms (Sforza et al., 2010).

As long as the 3D segments are modelled assuming rigid walls, the boundary conditions to be prescribed are flows. Changes in absolute flow merely change the magnitude of the velocities observed in the aneurysmal sac (Cebal et al., 2005a), and are therefore considered less relevant than the flow distribution over both the inlets (Castro et al., 2006b) and outlets. It has been observed that small intra-patient variations in flow distribution over the outlets do not affect the characteristics of the intra-aneurysmal velocity field (Cebal et al., 2005a). However, several papers show a high inter-patient variability of the cerebral vasculature. Only about 55% of all patients have a complete circle of Willis (David and Moore, 2008). Within the anterior circulation, common variations observed are either multiple Anterior Communicating Arteries (ACoAs) (21%) or an absent or hypoplastic ACoA (7%). In the posterior circulation a unilateral absent or hypoplastic Posterior Communicating Artery (PCoA) (27%) or hypoplastic PCA P1 segment (8%) are the most common variations. Considering the observed geometric variations of the cerebral arterial tree (David and Moore, 2008), significant inter-patient variations of flow distributions are expected and thus a patient-specific model including both inlet and outlet boundary conditions is sought.

As summarised by Marzo et al. (2011), most studies involving patient-specific inlet flows are based on pc-MR angiography, which allows local *in vivo* measurement of the flow pulse through a plane of measurement perpendicular to the artery of interest. Although this technique has been applied to the afferent arteries, the plane definition in the com-

plex geometries of smaller, more tortuous arteries is unreliable (Marzo et al., 2011; Hollnagel et al., 2009). Moreover, the diameter of the artery that can be measured is limited by the resolution of the imaging modality. Because of these limitations, pc-MR is unsuitable for obtaining boundary conditions at the small outlets.

Since the flow distribution is the true parameter of interest and the pc-MRA technique is deemed inappropriate for determining outlet flow distribution boundary conditions, a more global method is preferred. Alternatively, methods to extract flow from travelling contrast agent are being developed, allowing relative flow measurements in the smaller branches of the circle of Willis (Lieber et al., 2009).

If flow measurements cannot be performed at all the boundaries of the 3D segment, or only as an average in time, a 1D wave propagation model of the arterial tree may be used to estimate the flow waves at the location of interest based on measurements at more accessible locations. However, in addition to geometry and flow measurements, also pressure measurements may be needed to fully define a patient-specific 1D model. Although the need to apply patient-specific boundary conditions has been discussed in many papers (Marzo et al., 2011; Spilker and Taylor, 2010; Pope et al., 2009; Venugopal et al., 2007), as far as known by the authors of this paper, no studies dedicated to patient-specific 1D modelling of the flow in the cerebral arteries have been published until now.

The aim of this study is to explore the necessity of, and requirements for, full patient-specific 1D modelling, i.e., both geometry and boundary conditions based on patient data. The influence of both geometric variations and boundary conditions prescribed at the outlets are assessed.

To assess the impact of patient-specific geometry, two 1D patient-generic geometries introduced by Alastruey et al. (2007b) and Reymond et al. (2009) are compared with two 1D models comprising both patient-specific and patient-generic data. The patient-specific aspects of these models are obtained from the arterial segments from which the length and diameter could be extracted from the 3D rotational angiography data. This data set contains most of the cerebral circulation in both hemispheres, such that the circle of Willis remains patient-specific in the latter two models. The three-element windkessel models prescribed at the outlets of the 1D models have peripheral resistances based on a patient-generic flow division over the vascular domains (Mulder et al., 2011a), after which the resistance per truncated artery is based on its cross-sectional area (Alastruey et al., 2007b) or the wall-shear stress at the outlet (Murray, 1926). The effect of the choices made in these models on the flow waves throughout the cerebral circulation is analysed.

## 3.2 Materials and methods

### 3.2.1 Measurement methods

The patient-specific geometry of the cerebral circulation was based on a middle-aged male patient at the Royal Hallamshire Hospital (Sheffield, UK), who harboured multiple aneurysms in both hemispheres. A coiling procedure was required for aneurysms in

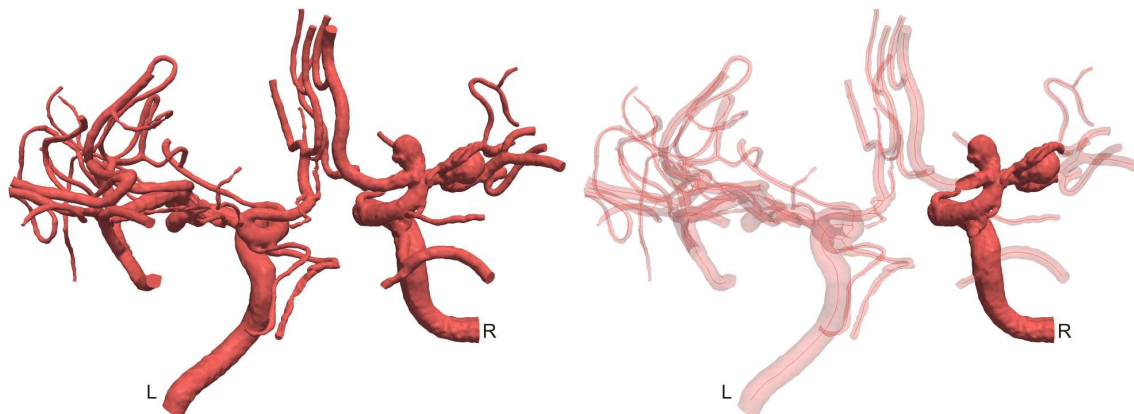


**Figure 3.1:** (left) The triangulated surface extracted from the 3D-RA data (posterior view), where L and R indicate the Left and Right side of the patient. (right) The centreline and local diameters are extracted to provide the 1D geometry, while a small segment of the surface defines the 3D geometry.

both the left and right middle cerebral artery. Therefore, rotational angiography images are available for both hemispheres, allowing extraction of the full anterior geometry and a part of the posterior circulation.

The 3D Rotational Angiography (3D-RA) was performed using a Philips<sup>®</sup> Integris<sup>™</sup> BV 5000 machine (Philips<sup>®</sup> Healthcare, Best, The Netherlands), recording 100 images in 4 s with an exposure time of 5 ms per image. Geometrical deformation was corrected for by means of a built-in x-ray image-intensifier, a close-circuit-digital camera and the standard Philips software. The voxel size in the reconstructed 3D images was 303 microns with a  $512 \times 512 \times 512$  reconstruction matrix. In accordance the ethical approval for @neurIST's (aneurist.org) for use of patient data, informed consent has been obtained and the images have been anonymised.

### 3.2.2 Data processing

The @neurIST computational tool-chain was used to extract the 1D and 3D geometry from the 3D-RA images, as described in Marzo et al. (2009) The vessel triangular surfaces were extracted using the threshold isosurface extraction tool. Artifacts and unnecessary vasculature was removed and the surface repaired. These surfaces are used to extract a 3D vascular segment containing two aneurysms, as well as the 1D geometry from the centrelines (fig 3.1).

For the 1D geometry, the processing aimed to preserve as much of the visualised vasculature as possible. The sculptured isosurface was used to compute the centreline and local diameters throughout the geometry (fig 3.1). The centreline extraction (Mellado et al., 2007), which is based on the flux driven automatic centreline extraction algorithm (Siddiqi et al., 2002), was insufficiently accurate to obtain the connectivity automatically due to the complexity of the vasculature. After manual identification of the relevant segments and the connectivity (fig 3.2), the segment lengths were derived from the centreline data.

**Table 3.1:** The arteries in the 3D model at which boundary conditions need to be prescribed (fig 3.2).

Nr.	Name
1	Internal carotid artery
2	Ophthalmic artery
3	Posterior communicating artery
4	Anterior choroidal artery
5	Anterior cerebral artery A1
6	Middle cerebral artery M2 inferior branch
7	Middle cerebral artery M2 inferior
8	Middle cerebral artery M2 superior
9	Middle cerebral artery M2 superior branch

Furthermore, tapering was ignored considering the short segment lengths and accuracy of the segmentation. Instead, the mean radius per segment was determined. Since the left Middle Cerebral Artery (MCA) was visualised in greater detail than the right MCA (fig 3.1), only the arteries up to the fifth generation from the start of the MCA were included while all more distal small side branches (family 6 and higher) are neglected. The flow waveforms are evaluated at the boundaries of the 3D segment (fig 3.2 and table 3.1).

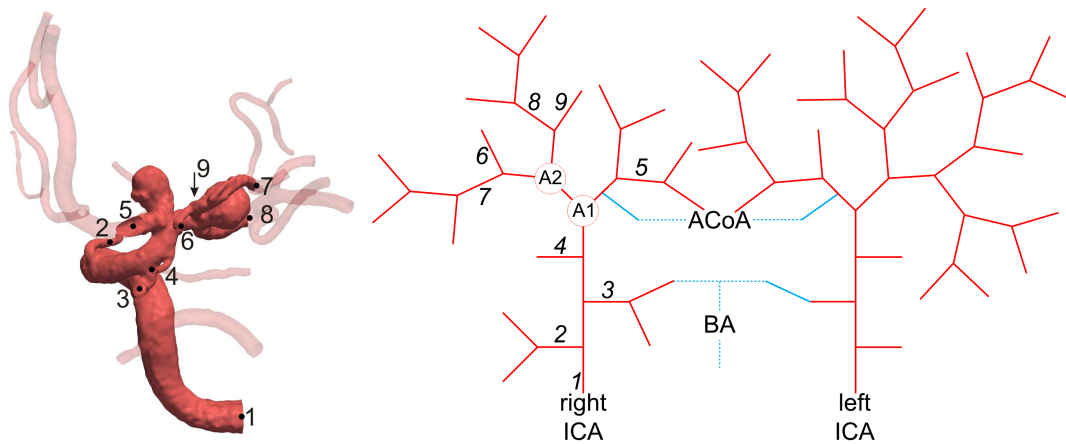


**Figure 3.2:** (left) The 3D patient-specific geometry (posterior view) and its boundaries. (right) Schematic representation of the connectivity of the arterial segments, where the numbers correspond to the numbers in the 3D geometry and table 3.1. A1 and A2 indicate the location of the two aneurysms present, while the dashed lines indicate how the two hemispheres are connected.

### 3.2.3 1D wave propagation model

The conservation of mass and momentum balance, describing 1D wave-propagation in incompressible fluids through distensible tubes (Hughes and Lubliner, 1973), are rewritten such that the pressure  $p$  and flow  $q$  are the parameters for which the set of equations is solved. Neglecting the influence of small side branches, and assuming a velocity profile

function as introduced by Bessems et al. (2007), the set of equations becomes

$$\begin{aligned} C_0 \frac{\partial p}{\partial t} + \frac{\partial q}{\partial z} &= 0, \\ \frac{\partial q}{\partial t} + \frac{\partial}{\partial z} \left( \delta_1(\alpha) \frac{q^2}{A} \right) + \frac{A}{\rho} \frac{\partial p}{\partial z} &= \frac{2\pi a}{\rho} \tau_w(\alpha) + \frac{\eta}{\rho} \frac{\partial^2 q}{\partial z^2}, \end{aligned} \quad (3.1)$$

with  $t$  the time,  $z$  the axial coordinate, and  $\rho$  and  $\eta$  the density and dynamic viscosity of the fluid, respectively. The arterial wall is characterised by the compliance per unit length  $C_0$ , while the cross-sectional area  $A$  and the radius  $a$  are geometrical parameters. The  $\delta_1$  and  $\tau_w$ , both functions of the Womersley parameter  $\alpha$  and based on the first harmonic, describe the influence of the non-linear and the friction term respectively. For more details on this model, the reader is referred to van de Vosse and Stergiopulos (2011) and Bessems et al. (2007).

**Geometry** The geometries modelled consist of two parts (fig 3.3); the body (black) and head (blue) respectively. Since the cerebral circulation is of interest here, only this part will be varied while the body vasculature is the same in all simulations. The vasculature of the body is based on data published by Stergiopulos et al. (1992) with some adaptations for the assumptions made in this model (e.g., thin-walled segments) (Mulder et al., 2011a). The two patient-generic cerebral geometries (fig 3.3, middle) are based on Alastruey et al. (2007b) (solid lines only), and Reymond et al. (2009) (solid and dotted lines). In order to obtain the patient-specific geometries, the segments in the patient-generic geometries, of which the lengths and radii could be extracted from the patient data, were substituted (fig 3.3, middle; thick lines). Since part of the posterior circulation and the supplying arteries were not imaged, a patient-generic geometry is assumed for this part of the vasculature. Figure 3.4 provides a schematic overview of the geometries considered here, which are referred to as RPG, APG, RPS and APS. Here, the first letter refers to the model from literature that has been used to define the cerebral circulation (Reymond and Alastruey, respectively). The last two letters indicate whether Patient-Specific (PS) data is included or alternatively, the geometry is fully Patient-Generic (PG). The subscript 2 and 3 refer to the assumptions made in the derivation of the terminal impedances applied, as will be described below.

The segment in which the patient-specific part of the geometry is coupled to the patient-generic part is adapted such that there is no transition in radius in order to avoid non-physiological reflections. Since in the ICA the patient-generic and specific part meet mid-segment, the radius of the patient-generic part was chosen to be equal to that of the patient-specific part (fig 3.3, right). The parameters defining all geometries are provided in Appendix A.

**Boundary conditions** At the aortic root, the flow pulse given by Olufsen et al. (2000) is prescribed, whereas the terminal impedance is prescribed at each outlet. This impedance is modelled by a three-element windkessel model (Westerhof et al., 1971), consisting of a resistance  $Z$  in series with a parallel combination of a capacitor  $C$  and another resistance

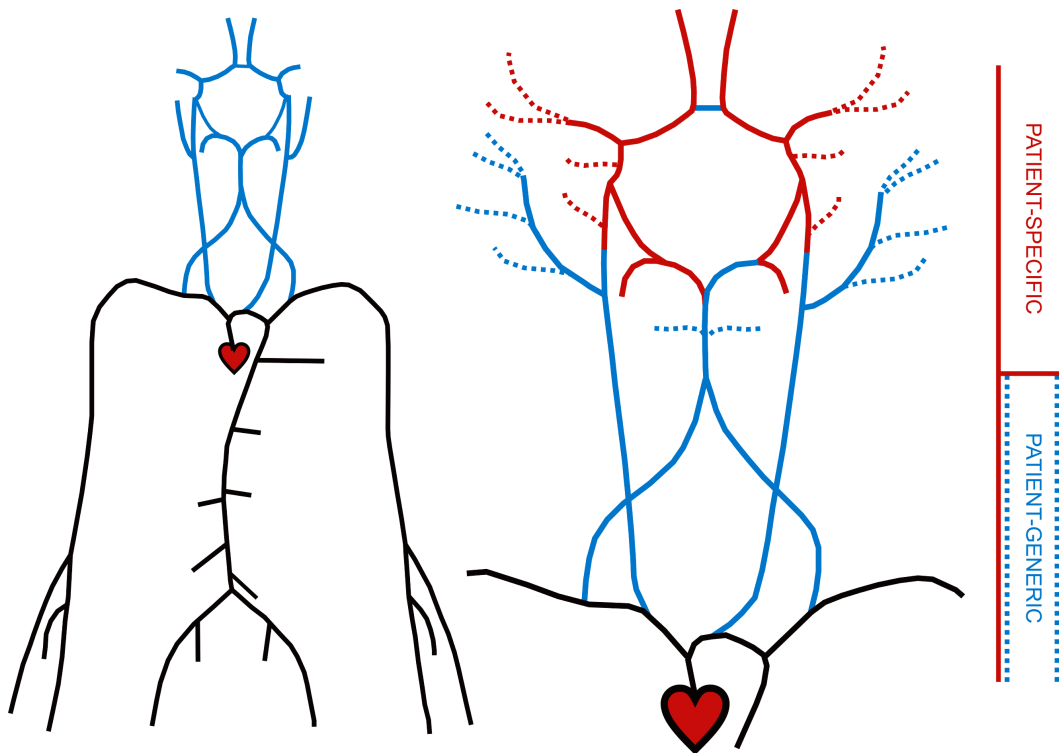


**Figure 3.3:** (left) Geometry of the vascular tree is divided into two building blocks: the body (black) and the head (blue). (middle) Two patient-generic cerebral geometries are considered; Alastruey (blue and red solid lines), Reymond (blue and red solid and dashed lines). The two patient-specific geometries are obtained by substituting the known part of the arterial tree (red) in Alastruey as well as the Reymond geometry. (right) If the patient-generic and specific parts are coupled mid-segment, the whole segment is given the patient-generic radius.

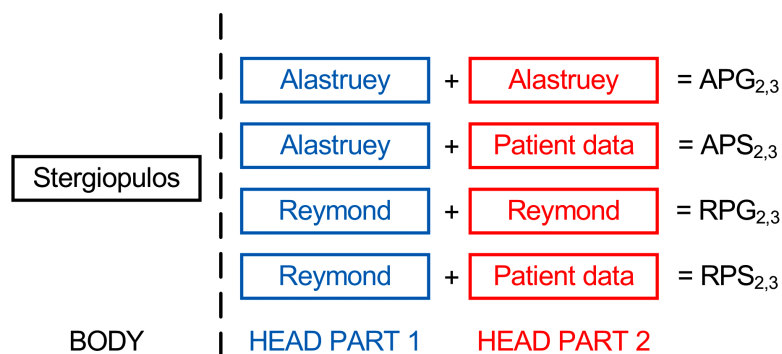


**Figure 3.4:** A schematic overview of the building blocks forming the patient-generic (APG and RPG) and patient-specific (APS and RPS) geometries with the boundary conditions based on the surface area (2) or the wall shear stress (3).

$R$ , resulting in:

$$\frac{\partial p}{\partial t} + \frac{1}{RC}p = \frac{1}{C} \left( \frac{Z}{R} + 1 \right) q + Z \frac{\partial q}{\partial t}. \quad (3.2)$$

The first resistance  $Z$  equals the high frequency characteristic impedance of the truncated artery in order to avoid high frequency reflections (Westerhof et al., 1971). In order to obtain a physiological flow distribution throughout the circulation, the geometry is divided into major vascular domains, such as the legs, head and liver. The total peripheral resistance of each vascular domain, which equals the parallel combination of the  $R_t = R + Z$  of all outlets within a domain, is chosen such that the desired flow distribution over the body parts is obtained (Mulder et al., 2011a). Within the cerebral vasculature, the distribution of the terminal resistances of the head can be based on either the wall shear stress (Murray, 1926), i.e., reciprocal of  $a^3$ , or the surface area of the outlet (Alastruey et al., 2007b), i.e., reciprocal of  $a^2$ . With  $R_{VD}$  being the total resistance of a vascular domain with  $N$  outlets, the resistance of a single truncated artery within that domain  $R_t$  equals

$$R_t = R_{VD} \frac{a_t^n}{a^n} \quad \text{with} \quad a_t^n = \sum_{i=1}^N a_i^n. \quad (3.3)$$

Both cases ( $n = 2, 3$ ) are considered here. The difference between the typical total compliance of the human body and the compliance captured by the 1D arterial segments equals the compliance to be incorporated in the peripheral beds  $C_{0D}$  described by the windkessel models. The distribution of this peripheral compliance is proportional to the flow distribution, i.e., the terminal resistances (Alastruey et al., 2007b):

$$C = C_{0D} \frac{R_T}{R_t}, \quad (3.4)$$

where  $R_T$  denotes the total resistance of the body. The resulting windkessel parameters are provided in Appendix A.

**Analysis** In total, eight simulations were performed (fig 3.4); two fully patient-generic geometries and two partially patient-specific geometries, each with outflow boundary conditions based on wall shear stress and the outlet area. In order to compare the results obtained with these models, the flow distribution over the inlets of the circle of Willis and the flow and pressure waveforms are evaluated.

The flow distribution over the afferent arteries obtained with the models is compared to the physiological flow distribution from literature. Approximately 70% and 30% of the flow through the CCA enters the ICA and External Carotid Artery (ECA) respectively (Marshall et al., 2004). Furthermore, about 80% of the blood flow supplying the circle of Willis is provided by both ICAs, whereas the remaining 20% comes from the Vertebral Arteries (VAs) (Tanaka et al., 2006). Combining these fractions provides the flow division over the CCA, ECA, ICA and VA relative to the total flow towards the head, i.e., the sum of the flow through the CCAs and VAs.

Since these models aim to provide boundary conditions for the 3D CFD model of the

**Table 3.2:** The flow distribution the cerebral circulation in % of the total inflow (CCAs + VAs). The geometries (abbreviations defined in figures 3.3 and 3.4) are either fully Patient-Generic (PG) based on Alastruey et al. (2007b) (A), Reymond et al. (2009) (R), or partially Patient-Specific (PS). The last column shows the physiological flow distributions Marshall et al. (2004); Tanaka et al. (2006).

	APG3	APG2	RPG3	RPG2	APS3	APS2	RPS3	RPS2	Phys.
r. ECA	19	17	14	16	13	9	14	10	13
l. ECA	18	17	14	16	13	9	14	10	13
r. ICA	24	25	25	25	35	39	37	40	30
l. ICA	23	24	23	22	25	30	24	28	30
r. VA	8	9	12	11	6	6	6	6	7
l. VA	8	9	12	11	6	7	6	6	7

arterial segment introduced in figure 3.1, the flow waveforms (fig 3.5) are visualised at the locations of the 3D boundaries depicted in figure 3.2.

### 3.3 Results

Although the APG shows a physiological distribution over the CCAs (ICAs + ECAs) and VAs (table 3.2), the flow in the ECA is high relative to the flow in the ICA compared the physiological division (last column). In the RPG models, the flow through the VAs is high relative to the flow in the CCAs compared to the physiological distribution, resulting in an underestimation of the flow fraction in the ICA.

The patient-generic models show a marked asymmetry of the flow in the CCAs, while the sum of the left and right CCA corresponds to 86% of the total inflow as expected from literature. When the peripheral resistances are based on the wall shear stress (APS3 and RPS3), the sum of the left and right flow fraction resembles the physiological flow distribution. When the resistances are based on the surface area (APS2 and RPS2) however, the flow fraction through the ECAs appears underestimated. All patient-specific models result in an asymmetric flow division over the right and left hemisphere.

When comparing the flow waves at the sites corresponding to the boundaries of the 3D model, it becomes evident that the geometry and method of deriving boundary conditions significantly affect the mean flow as well as the waveform. The flow in the MCA M1 segment (fig 3.5, panel 10) that is obtained with the RPG model is significantly lower than the flow obtained with the other models. Furthermore, this model predicts the flow in the PCoA to be directed towards the ICA, which is opposite to the flow direction in the other models. Typically, the asymmetric flow observed in the patient-specific model results in higher flows than those predicted by the patient-generic model. This does not hold for the anterior choroidal artery, which is due to its smaller radius in the patient-specific model.

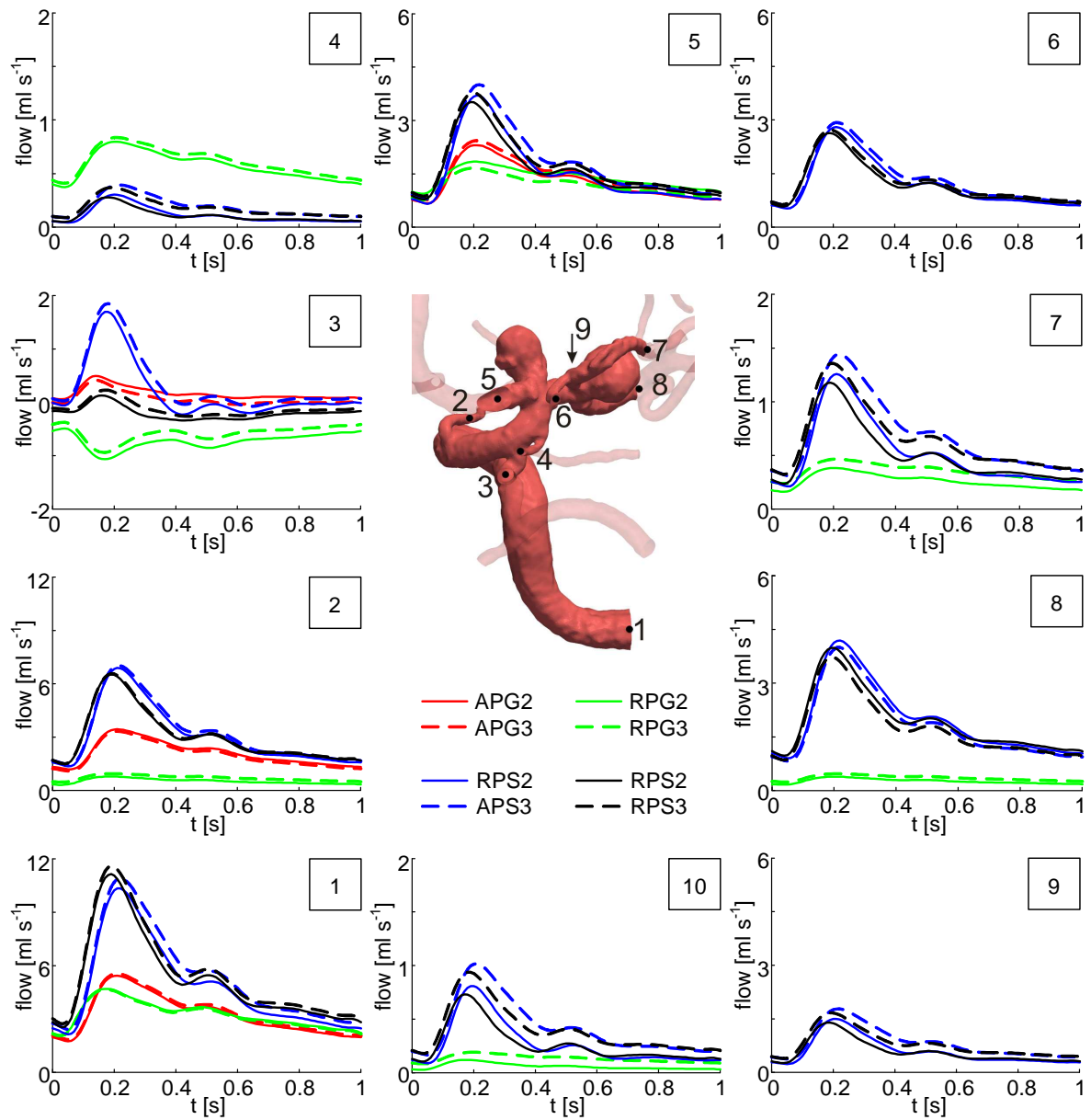


Figure 3.5: Flow pulses at the boundaries of the 3D geometry (fig 3.2; table 3.1). In order to allow comparison to the Alastruey model, the flow at the MCA Mr segment is shown (panel 10).

## 3.4 Discussion

### 3.4.1 General findings

Considering clinical practice and the limitations of current technology, measuring the flow and pressure at the boundaries of the 3D arterial segment of interest in each patient to serve as boundary conditions for a 3D aneurismal flow analysis is undesirable and often not possible. Furthermore, in order to minimise the risk of rupture during the measurement procedure, performing the pressure and flow measurements either non-invasively at more accessible locations or at a reasonable distance from the aneurysm is preferable. A 1D wave-propagation model facilitates the computation of pressure and flow pulses throughout the cerebral circulation, allowing extraction of local boundary conditions given a geometry and pressure and flow waves at some distant location. However, many parameters are involved in such a model, specifying the geometry, mechanical behaviour of the wall as well as the fluid, and the boundary conditions describing the peripheral circulation. One of the questions to be answered is to what extent patient-specific data are needed to obtain valuable boundary conditions from the 1D wave-propagation model.

In this paper, a full patient-specific model of the 1D wave-propagation in the cerebral circulation is defined as a model in which both the vascular geometry as well as the set of outflow boundary conditions are derived from patient-specific data. In order to investigate the relevance of such a full patient-specific model providing boundary conditions for a 3D flow analysis of a specific segment, several simulation results using different modelling assumptions have been compared.

To enable the comparison, the inflow domain (proximal to the carotid and vertebral arteries) was identical in all models, i.e., the vascular geometry was based on data provided by Stergiopoulos et al. (1992) and the cardiac output was based on Olufsen et al. (2000) in all simulations. Outflow conditions have been represented by terminal impedances (pressure-flow relations) defined by three-element windkessel models. The parameters defining each windkessel model were derived from the local geometry of the outflow tracts, where both wall shear stress and cross-sectional area based relations have been used. Two recently published patient-generic data sets representing the cerebral vascular geometry (Alastruey et al., 2007b; Reymond et al., 2009) were connected to the common inflow domain and showed remarkable differences in flow at locations relevant for the provision of boundary conditions for 3D analysis. Since the inflow is identical for each of the two models, these differences can only be explained by the differences in the geometry of the cerebral vasculature and the differences in the corresponding outflow conditions. Knowing that the resistive part of the terminal impedances is much larger than the resistance due to viscous losses in the corresponding supplying arteries, it can be stated that the outflow condition at each of the terminal branches is the main determinant for flow distribution and thus responsible for the differences found between the two patient-generic models.

The differences between the two, both seemingly reasonable models of the cerebral cir-

culature are indicative for the importance of full patient-specific modelling. This has been verified in this study by replacing the circle of Willis and its distal circulation in both models by patient-specific vasculature and its corresponding boundary conditions obtained from 3D-angiographic data of a patient. Even more remarkable and significant differences in flow distribution (both in sign and magnitude) were found compared to the patient-generic models, whereas the differences between the wall shear stress based and cross-sectional area based outflow conditions were less pronounced.

Provided that the derivation of the windkessel parameters as used in this study is meaningful, this result clearly indicates that a simple patient-generic 1D model to provide boundary conditions for a 3D flow analysis in cerebral aneurysms is not sufficient. Obviously, in order to fully establish the significance of the findings presented in this paper, more patient data should be included. However, considering the variability of the geometry of the cerebral vasculature observed *in vivo* (David and Moore, 2008), and the sensitivity of the boundary conditions to geometrical variations, significant inter-patient variations in flow are to be expected. Although it is clear that different flow boundary conditions (fig 3.5) are obtained with the different models evaluated here, the effect on the characteristics of the 3D velocity field in the aneurismal sac, such as the complexity of the vortex structure, may be limited and still needs to be surveyed.

### 3.4.2 Case study

In general, the mean flows in the patient-specific models are found to be higher than those in the patient-generic models, with the exception of the flow through outlet 4 (fig 3.5 panel 4; this location is not defined in Alastruey's model). The radius of this branch in the patient is 0.6 mm, which is smaller than the radius assumed by Reymond (average of 0.7 mm), on which the patient-generic model was based. Therefore, the velocities through this outlet are expected to be unrealistically high when applying the patient-generic boundary conditions on the patient-specific 3D geometry. Especially the lower velocities in the branches adjacent to the aneurysm neck (MCA and ACA; fig 3.5 panels 5 and 10) are expected to lead to lower velocities within the aneurysmal sac, resulting in lower shear stresses on the aneurysm wall. Also, differences in flow through the parent arteries could induce differences in the intra-aneurysmal flow patterns, e.g. the complexity of the flow and vortex strength. Again, the resulting wall shear stresses could show differences in both pattern and magnitude. This would be a concern since the complexity of the flow patterns and the values and patterns of the wall shear stress are considered potentially valuable parameters in the assessment of aneurysm stability (Cebal et al., 2005b).

The effect of deriving the peripheral resistance on either the wall shear stress or the surface area is less pronounced than the effect of the geometry of the segments (fig 3.5). Of course, the effect of the assumption made in the derivation of the in peripheral resistance cannot be considered independently as the resistance is determined by the radius of the outlet branches, i.e., the geometry. However, when considering one geometry (e.g., RPS2 versus RPS3), the differences in the flow waves obtained with the two different pe-

peripheral resistances are smaller than when two geometries (e.g., RPS2 versus RPG2) are compared.

The patient-specific geometry showed more small side branches in the left MCA than in the right MCA. The resulting flow distribution was skewed, i.e., higher flow rates were observed in the less detailed right MCA. The vasculature showed asymmetrical mean radii (e.g., left ICA 2.39 mm vs. right ICA 2.69 mm), suggesting there might indeed be an asymmetry of flow. However, incorporating side-branches up to the 5<sup>th</sup> generation counted from the start of the MCA reduced this effect. The results shown are obtained with the reduced model, where the outlets of the left and right MCA were of the same calibre. However, it is a concern that shifting the truncation point has such an effect on the flows obtained. This is caused by the way the boundary conditions are derived. Since the peripheral resistances scale with  $a^2$  or  $a^3$ , the resistances are sensitive to small changes in outlet radius. Obviously, deriving the boundary conditions from the local geometry would be convenient, although the methods applied should be tested properly. The only way to achieve this is by measuring the flow distribution *in vivo*.

### 3.4.3 Impact on clinical application

In the case study presented here, the full patient-specific geometry of the circle of Willis was available since both hemispheres were visualised with 3D-RA. For this, an additional injection of contrast was required so the patient was exposed to a relatively high amount of radiation. However, usually only the 3D vasculature in one hemisphere is available, allowing only a partially patient-specific model. Possible implications of this model incompleteness still need to be investigated. Although contrast-enhanced Magnetic Resonance Angiography (MRA) provides high resolution images, the measurement-time is significantly longer than that of 3D-RA. A problem involved in this method is the enhancement of the veins, and again an injection of contrast agent is required. This can be circumvented by time-of-flight MRA, but this method relies on high flows and is therefore known to partially miss large aneurysms. The advantage of MRA is the possibility to measure the flow distribution over the supplying arteries with phase-contrast MRA. Unfortunately, the flow distribution over the small outlet branches cannot be measured due to resolution issues. This can be done by applying videodensitometry to an x-ray sequence, although the required injection does alter the flow to be measured. Fortunately, 1D models in which the injection was included suggested that the influence of the injection on the flow through afferent arteries of the circle of Willis was in the same order of magnitude (Mulder et al., 2011a). This allows measuring the flow distribution over the outlets within the field of view, such that the distribution of the peripheral resistances can be estimated.

In order to extract the patient-specific geometry from the raw images, segmentation is needed. Although segmentation based on geodesic active regions (GAR) shows superior accuracy and repeatability relative to iso-intensity surface extraction (ISO) (Bogunovic et al., 2011), the computational costs are significantly higher for the first. Considering the size of the region incorporated in the 1D geometry, ISO had to be applied. The centreline

was less accurate for arteries with an irregular cross-sectional shape, kissing arteries and small arteries with high curvature. A more robust and accurate method should be used in the future studies (see e.g., Lesage et al. (2009)), allowing automated extraction of segment data and connectivity.

The geometry of the proximal vascular domain is believed to be of lesser importance, although it does affect incoming flow and pressure waves. It could be made more patient-specific by scaling the segments with the height of the patient, relating the arterial stiffness to the age, and scaling the cardiac output (Reymond et al., 2009). The latter is the least relevant as absolute flow changes with the physiological state of the patient anyway.

## 3.5 Conclusion

The variations in model assumptions applied in this study significantly influence the resulting flow pulses to be prescribed at the boundaries of the arterial segment. Therefore, incorporating the patient-specific geometry of the cerebral arterial tree and the associated outflow boundary conditions are expected to be necessary to obtain boundary conditions for a representative 3D velocity field computation in the aneurismal sac. However, the exact effect on the computed 3D aneurismal velocity field and its implications for rupture risk predictions remains to be established. If the effect on the characteristics of the intra-aneurysmal velocity field is found to be significant, *in vivo* flow measurements will be needed to validate the full patient-specific 1D model described in this study.

## CHAPTER FOUR

# The effect of patients-specific boundary conditions on the 3D intra-aneurysmal velocity field

---

In general, the intra-aneurysmal velocity field is obtained with a 3D Computational Fluid Dynamics (CFD) model, where patient-generic boundary conditions are prescribed on a patient-specific geometry. In chapter 3, the flow waves obtained with a 1D wave propagation model based on patient-specific geometrical data of the cerebral vasculature was compared to those obtained with a patient-generic model based on literature. The resulting flow waves to be prescribed at the 3D boundaries showed significant differences. In this chapter, the characteristics of the velocity field obtained with patient-generic and patient-specific boundary conditions are evaluated by prescribing the end-diastolic flows obtained in chapter 3. The corresponding intra-aneurysmal vortex and wall shear stress distribution shows remarkable differences, indicating patient-generic boundary conditions are indeed not suitable to obtain a realistic representation of the intra-aneurysmal velocity field.

## 4.1 Introduction

Cerebral aneurysms are localised dilatations of the arterial wall in the brain, which may be prone to rupture. As the resulting haemorrhage is associated with high mortality and morbidity rates, indicators for the rupture risk are sought. From a mechanical point of view, the rupture risk is determined by the loading state and the mechanical properties of the arterial wall, which are both related to the haemodynamics (chapter 2). Haemodynamical factors are believed to play an important role in cerebral aneurysm growth and rupture via the adaptation of the arterial wall (Ujiie et al., 1999; Singh et al., 2010). Parameters that have been identified as likely candidates in aneurysm stability assessment are for example the complexity of the intra-aneurysmal flow patterns (Cebral et al., 2005b,c) and the wall shear stress (Boussel et al., 2008). In order to obtain the characteristics of the intra-aneurysmal flow patterns, the 3D velocity field needs to be determined.

Computational Fluid Dynamics (CFD) is commonly used to obtain the velocity field in a small segment of the cerebral arterial tree, of which the geometry is extracted from patient data. However, in current studies the prescribed boundary conditions at the outlets still are based on patient-generic data (see e.g., Cebral et al. (2011)). In order to obtain a more representative intra-aneurysmal velocity field, patient-specific boundary conditions may be required.

As the geometry of the cerebral vasculature shows significant inter-patient variability (David and Moore, 2008), a 1D wave propagation model of which the geometry of the cerebral arterial tree is based on patient-data has been developed (chapter 3). Incorporating the patient-specific geometry proved to significantly affect the flow waveforms throughout the cerebral arterial tree (chapter 3), and therefore the flow pulses to be prescribed at the boundaries of the 3D segment of interest. The effect of these variations on the characteristics of the 3D intra-aneurysmal velocity field needs to be evaluated in order to establish the impact of this inter-patient variability and the effect of the mismatch of the patient-specific vascular geometry and patient-generic boundary conditions.

To this purpose, a case study is presented in which the end-diastolic flows obtained with both a patient-generic 1D geometry (Reymond et al. (2009); RPG) and a patient-specific geometry (Mulder et al. (2011a); RPS) are prescribed. The resulting intra-aneurysmal velocity fields are compared both qualitatively and quantitatively. Based on this comparison the importance of patient-specific modelling when using haemodynamics to predict cerebrovascular events is illustrated.

## 4.2 Materials and methods

### 4.2.1 Geometry domain

The vascular geometry of the segment including the cerebral aneurysm is obtained from 3D-RA data as described in chapter 3. The surface within the user-defined region of interest (ROI) is extracted using GAR-segmentation (@neufuse software, aneurist.org).

Irregularities are manually removed, smoothing is applied, and the truncated arteries are clipped and capped to create outlet surfaces perpendicular to the local centreline.

The surface is converted into a volume mesh using ICEM (ANSYS) and processed such that the geometry is defined by 268485 second-order Taylor Hood tetrahedrons (fig 4.1), with a total of 1275923 degrees of freedom. The 3D domain  $\Omega \subset \mathbb{R}^3$  (the lumen) in which the pressures and velocities are computed is constrained by the closed boundary  $\Gamma_0$  (the arterial wall). Note that the aneurysm at the MCA bifurcation is not included in order to reduce the complexity of the analysis (fig 3.2 vs. fig 4.1).

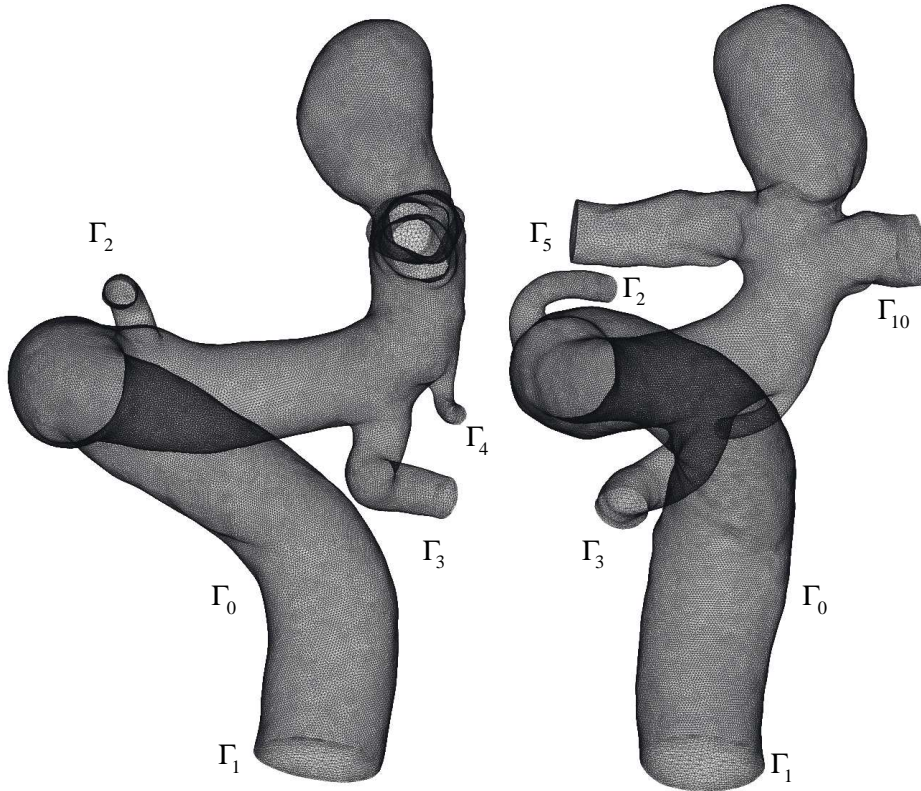


**Figure 4.1:** Two perpendicular views of the 3D surface extracted from the 3D-RA patient data is converted into a triangulated surface mesh corresponding to the surface elements in the volume mesh.

### 4.2.2 Computational model

Incompressible Newtonian flow is described by the Navier-Stokes equations, which, when neglecting the influence of body forces like gravity, reads

$$\rho \frac{\partial v}{\partial t} + \rho(v \cdot \nabla)v = -\nabla p + \eta \nabla^2 v, \quad (4.1)$$

$$\nabla \cdot v = 0. \quad (4.2)$$

**Table 4.1:** End-diastolic and mean flows in  $\text{ml s}^{-1}$  at the truncated arteries of the 3D segment.

		RPG		RPS	
		$q_d$	$\bar{q}$	$q_d$	$\bar{q}$
Internal carotid artery (ICA)	$\Gamma_1$	2.21	3.26	2.82	5.23
Ophthalmic artery (Ophth)	$\Gamma_2$	0.03	0.06	0.13	0.27
Posterior communicating artery (PCoA)	$\Gamma_3$	0.54	0.73	0.17	0.21
Anterior choroidal artery (Ant chor)	$\Gamma_4$	0.40	0.57	0.06	0.11
Anterior cerebral artery (ACA)	$\Gamma_5$	0.99	1.38	0.88	1.61
Middle cerebral artery (MCA)	$\Gamma_{10}$	0.34	0.52	1.68	3.04

Here,  $\rho$  and  $\eta$  denote the constant density and dynamic viscosity,  $v$  the velocity vector, and  $p$  the hydrostatic pressure. More details on the resulting set of equations to be solved numerically are provided in chapter 2. A Newton-Raphson linearisation of the non-linear term was used to achieve convergence within each time step, and the temporal discretisation is achieved by the Euler implicit scheme. The model was implemented in the in-house finite-element package TFEM (TFEM User's Guide, M.A. Hulsen, 2010). The PARDISO solver allows parallel direct solving of this large set of equations ([www.pardiso-project.org](http://www.pardiso-project.org)).

### 4.2.3 Boundary conditions

The 1D model from which the boundary conditions are extracted is described in chapter 3. In essence, the geometry of the cerebral vasculature is based on patient-generic data from Reymond et al. (2009) or a combination of patient-specific data and the data from Reymond. These models will be referred to as RPG (Reymond Patient-Generic) and RPS (Reymond and Patient-Specific) respectively. In the RPS model, the segments of which the patient-specific geometry is available substitute the corresponding segments in the RPG model. The terminal resistances of the windkessel models prescribed at each outlet of the 1D model are derived from the outlet radius assuming constant target wall shear stress throughout a vascular domain, while the compliances are based on the flow distribution. More details on the derivation of the boundary conditions for the 1D model are provided in chapter 5, while the patient-generic and patient-specific geometries are introduced in chapter 3.

At each truncated artery in the 3D model, the end-diastolic flow extracted from the corresponding branch in the 1D model is prescribed (figs 4.1, 4.2 and table 4.1). The integral of the velocity component perpendicular to the  $i^{\text{th}}$  truncated artery  $\Gamma_i$  over the surface area of the outlet equals the flow through that outlet  $q_{1D,i}$ ,

$$\int_{\Gamma_i} v(t) \cdot n_i d\Gamma = q_{1D,i}(t) \quad \text{with } i \geq 1. \quad (4.3)$$

These expressions are added to the set of equations by introducing a Lagrangian multiplier for each of outlet, essentially prescribing the boundary conditions by defining con-

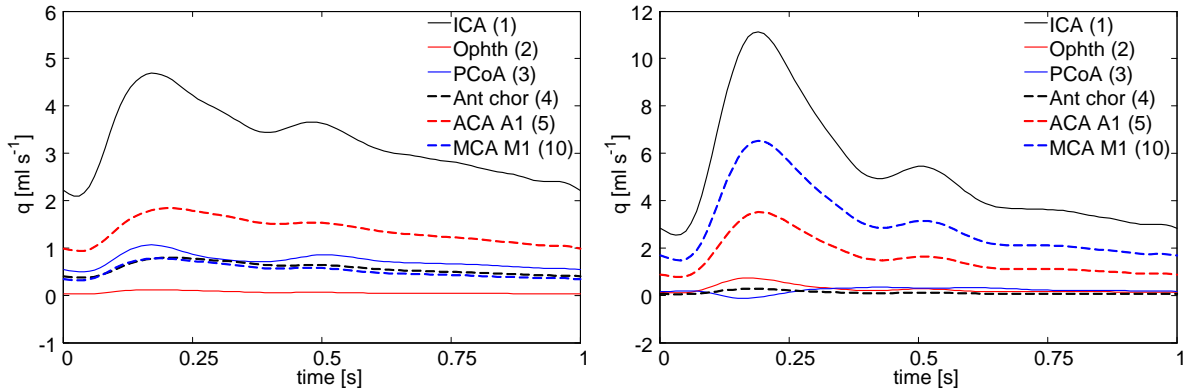


**Figure 4.2:** The flow waveforms at the truncated arteries of the 3D segment are based on (left) a patient-generic model Reymond et al. (2009) and (right) a patient-specific model (chapter 3).

straints. This leaves the velocity components parallel to each outlet undefined, resulting in possible flow instabilities from computational origin. In order to solve this, the in-plane velocities are set to zero at each nodal point on each outlet surface, thus

$$v(t) \cdot t_{i,j} = 0, \quad (4.4)$$

where  $t_{i,j}$  with  $j = 1, 2$  is the  $j^{\text{th}}$  tangent of the  $i^{\text{th}}$  outlet. In order to enable the use of (4.3), these constraints too are added to the set of equations using Lagrangian multipliers rather than being imposed as Dirichlet boundary conditions.

The latter constraint is applied to all truncated arteries, while the first, concerning the flow through the surface, is applied to all but one. A stress-free outlet condition is prescribed at the Posterior Communicating Artery (PCoA; outlet 4 in figure 3.2), as the flow through this branch should equal the sum of the flows through the other truncated arteries. While this assumption is correct for stationary boundary conditions, it does not hold when pulsatile flows are prescribed. Due to the arterial compliance incorporated in the 1D model, the sum of the flows through the in- and outlets is not equal to zero at all times. The distensibility is not included in the 3D model, which results in a discrepancy between the flow predicted by the 1D model and outflow through the open outlet, i.e. the sum of the flows prescribed at the other outlets (fig 4.3).

At the rigid wall, no slip is assumed. Since no pressures have been prescribed, the computed offset in the computed pressures will be undefined.

#### 4.2.4 Data analysis

In order to assess the differences caused by prescribing boundary conditions obtained with the RPG and RPS model, the pressure distribution throughout the 3D domain and the velocity fields at several cross-sections are evaluated (fig 4.4). Since the flow patterns in the aneurysmal sac are of primary interest in this chapter, the intra-aneurysmal velocities and instantaneous streamlines are discussed in more detail, and the effect of the observed differences on the wall shear stress is visualised.

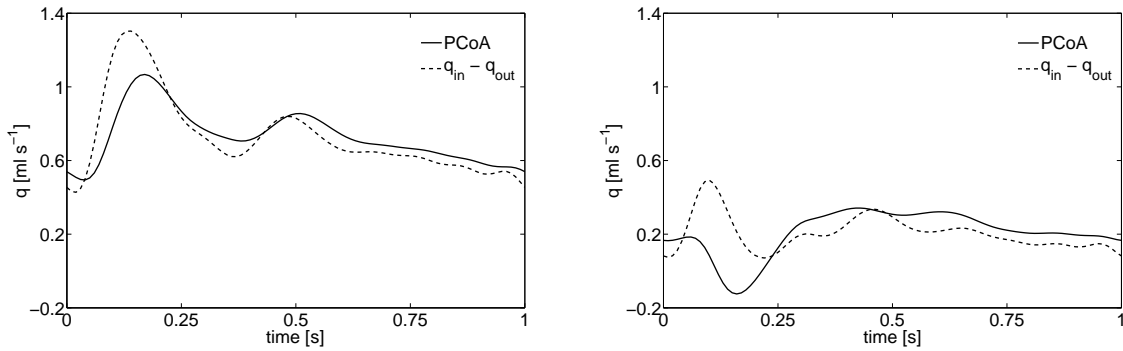


**Figure 4.3:** The flow through the unprescribed artery according to the 1D model (solid) and the effective flow  $q_{in} - q_{out}$  (dashed) do not correspond due arterial distensibility. In (left) the RPS model this effect is smaller than in (right) the RPS model, due to the lower pulsatility observed in the RPG model (fig 4.2).

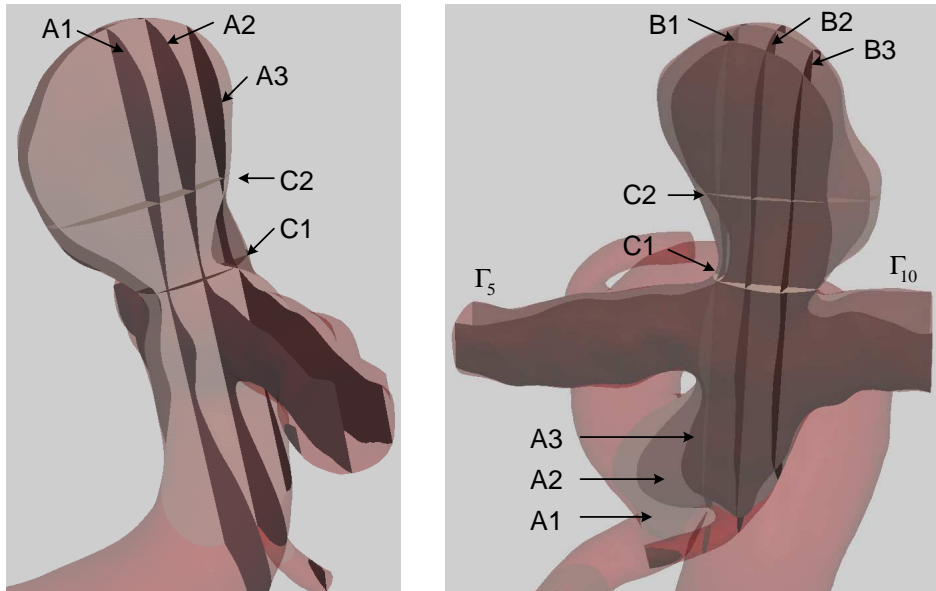


**Figure 4.4:** The slices at which the velocity field is visualised.

### 4.3 Results

The resulting 3D velocity fields, both complex with significant secondary flows (figs 4.5 and 4.6), show several remarkable differences. Both the RPG and RPS model reveal comparable secondary flow patterns in the ICA (outlet 1), as to be expected considering the high degree of curvature. The major differences are observed near the aneurysm neck. For example, the magnitude of the velocities are higher in the RPS model and the flow is more evenly distributed over the ACA and MCA (outlets 5 and 10; fig 4.5 right). This results in higher velocities and a stronger vortex in the aneurysmal sac (fig 4.6). Although the location of the inflow and outflows are similar for both models, the vortex core is situated deeper into the aneurysm (fig 4.6 bottom).

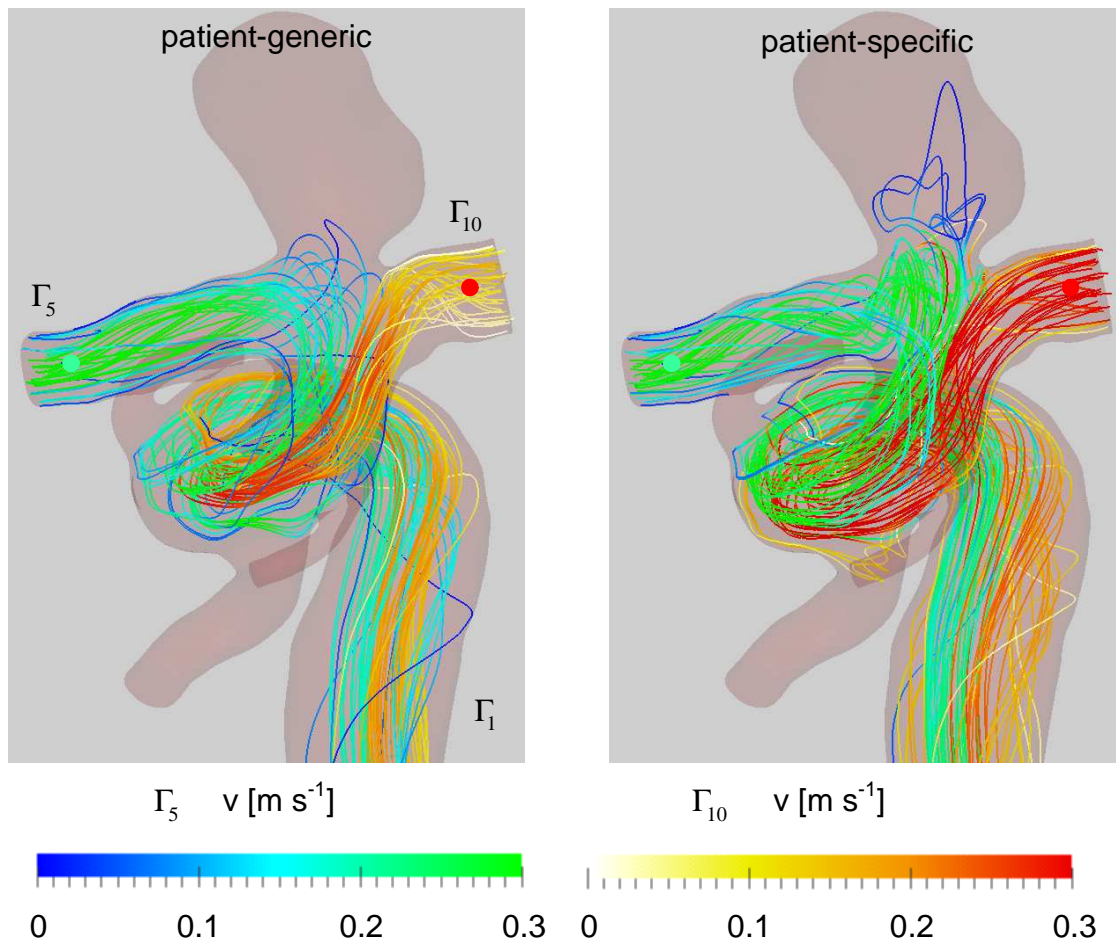


**Figure 4.5:** The streamlines throughout the 3D domain reveal a significant degree of swirl in the ICA with the boundary conditions based on the (left) RPG model and (right) RPS model. The line colours indicate the magnitude of the velocities, and the dots indicate the center of the area where seed points are located (for more information see paraview.org).

At the anterior choroidal artery (outlet 4), the flow obtained with the patient-generic model is much larger than that obtained with the patient-specific model (fig 4.2 and table 4.1). In addition, the radius of the corresponding branch in the patient-specific vasculature is smaller than the radius in the patient-generic geometry (0.6 and 0.7 mm, respectively), resulting in an unrealistically high pressure gradient (fig 4.7 left) and high velocities (fig 4.8; panel 3) in this outlet when the RPG boundary conditions are prescribed. The gradual pressure variations obtained with the RPS model are more representative of the expected *in vivo* pressure distribution.

The difference in flow distribution over the ACA and MCA (outlets 5 and 10) results in a difference in flow pattern just proximal to the neck (fig 4.8; panel 1 and 2). In the PG model, the flow from the ICA splits in two streams at the MCA side of the neck, where the major part supplies the ACA. In the PS model, most of the blood flow enters the MCA rather than the ACA. The division leads to two high velocity domains with opposite directions, effectively introducing a shear layer between the two regions and significant

secondary flow at the aneurysm neck (fig 4.9). The latter enhances the intra-aneurysmal vortices in the RPS model, resulting in lower intra-aneurysmal velocities in the RPG model.

Indeed, the magnitude of the velocities through the neck are lower in the RPG case (fig 4.10), resulting in much (20 times) lower velocities in the aneurysmal sac. These low intra-aneurysmal velocities in the RPG model lead to low shear stresses on the aneurysm wall (fig 4.11). The wall shear stress distribution shows a region of high wall shear stress near the neck in the RPS model, while the RPG wall shear stress is fairly uniformly distributed.

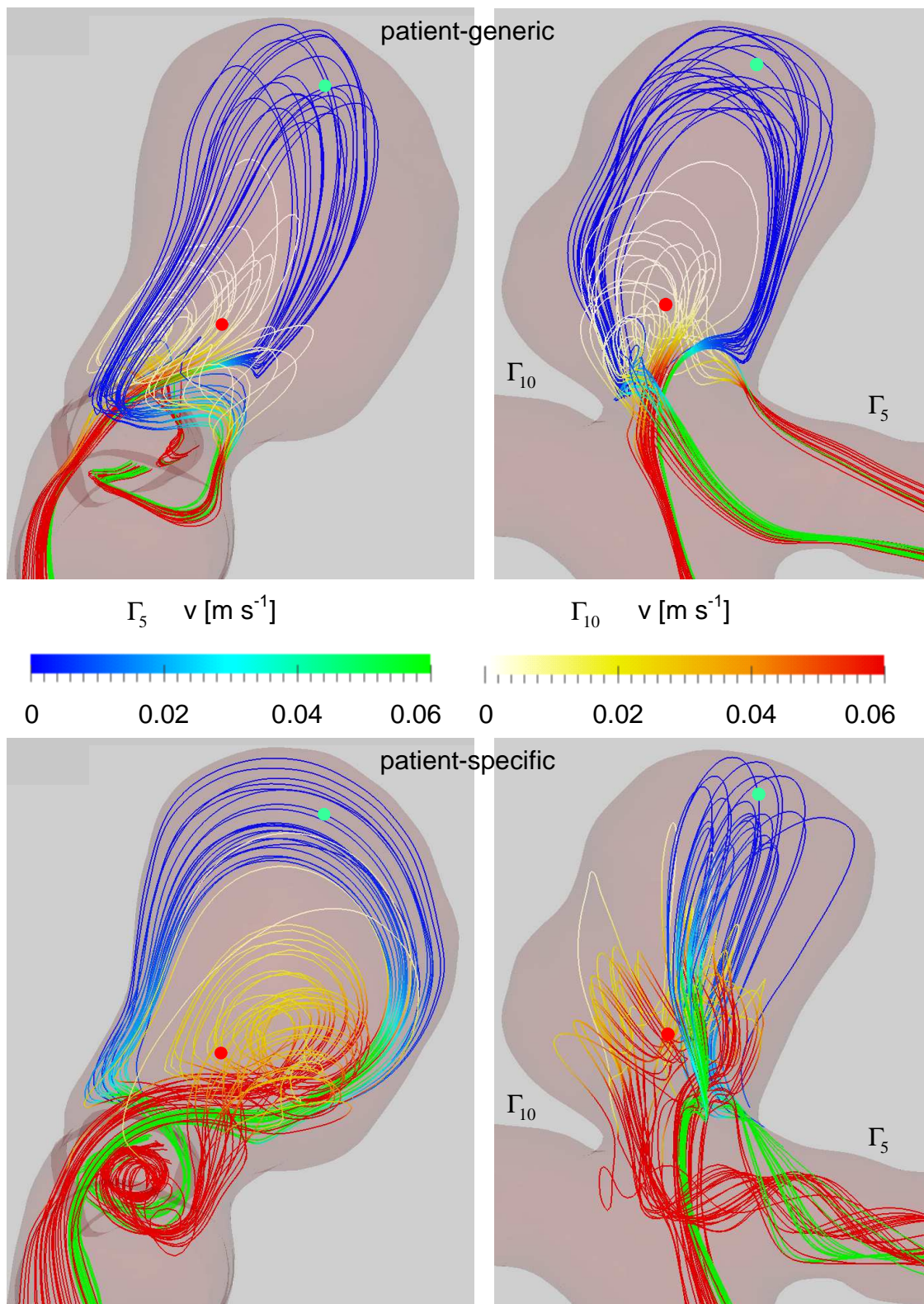


**Figure 4.6:** The intra-aneurysmal streamlines with the boundary conditions based on the (top) RPG model and (bottom) RPS model show the complexity of the aneurysm vortex. The line colours indicate the magnitude of the velocities, and the dots indicate the center of the area where seed points are located (for more information see paraview.org).

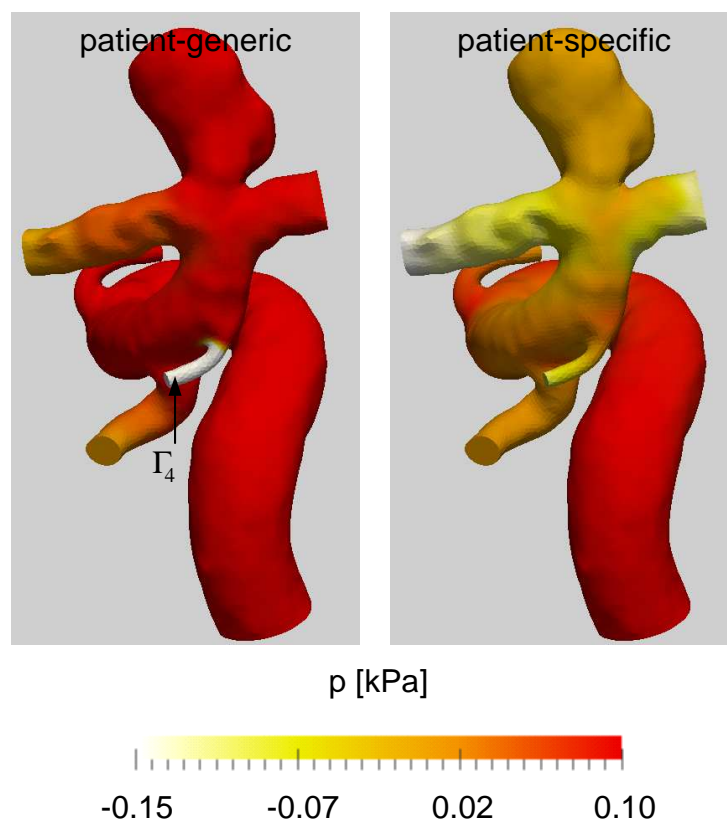


**Figure 4.7:** The pressures throughout the 3D domain with the boundary conditions based on the (top) RPG model and (bottom) RPS model. Note that the offset in pressure has not been defined.

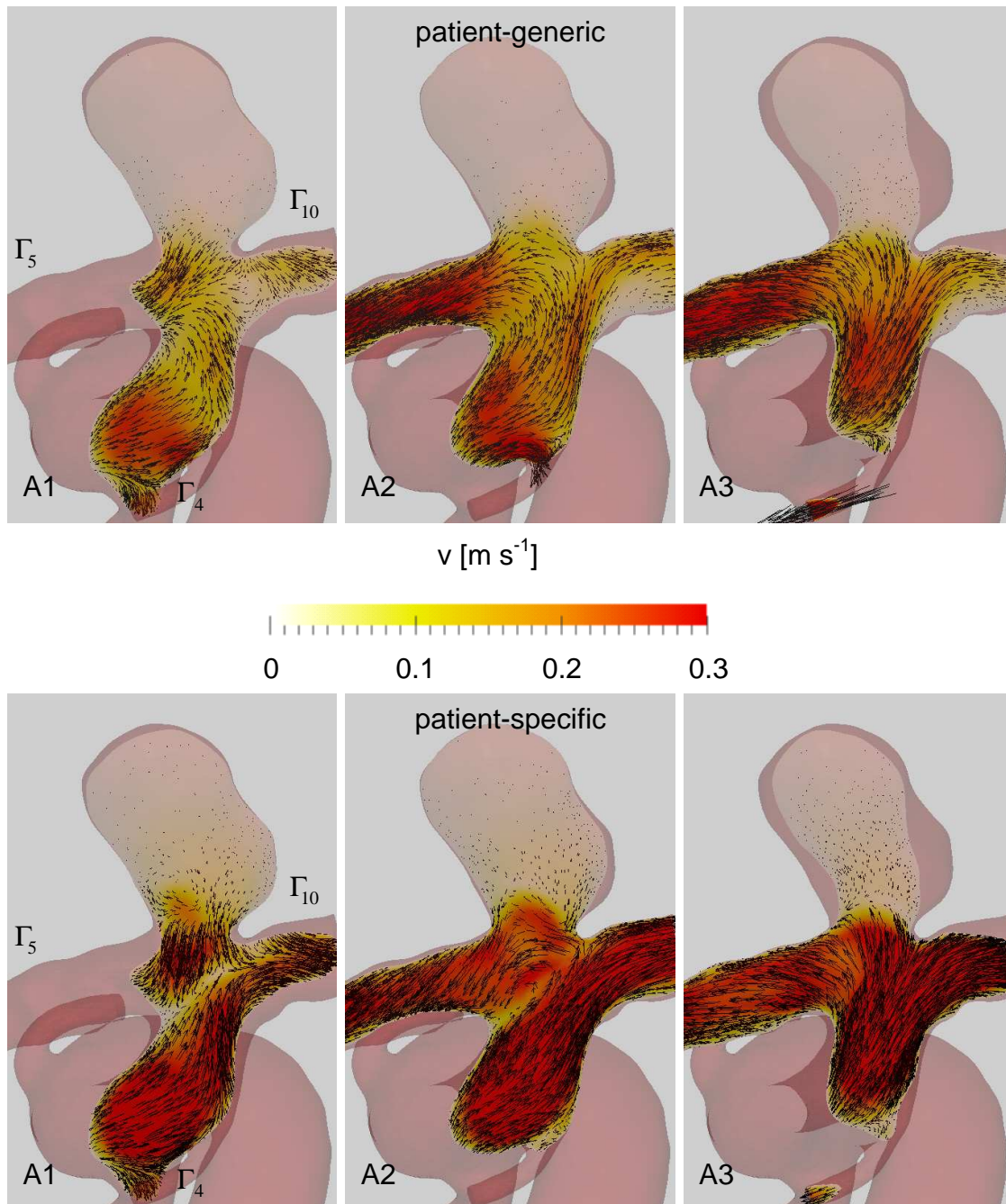


**Figure 4.8:** The velocity field on the vertical slices parallel to the MCA/ACA (A1 – 3; fig 4.4) with the boundary conditions based on the (top) RPG model and (bottom) RPS model.

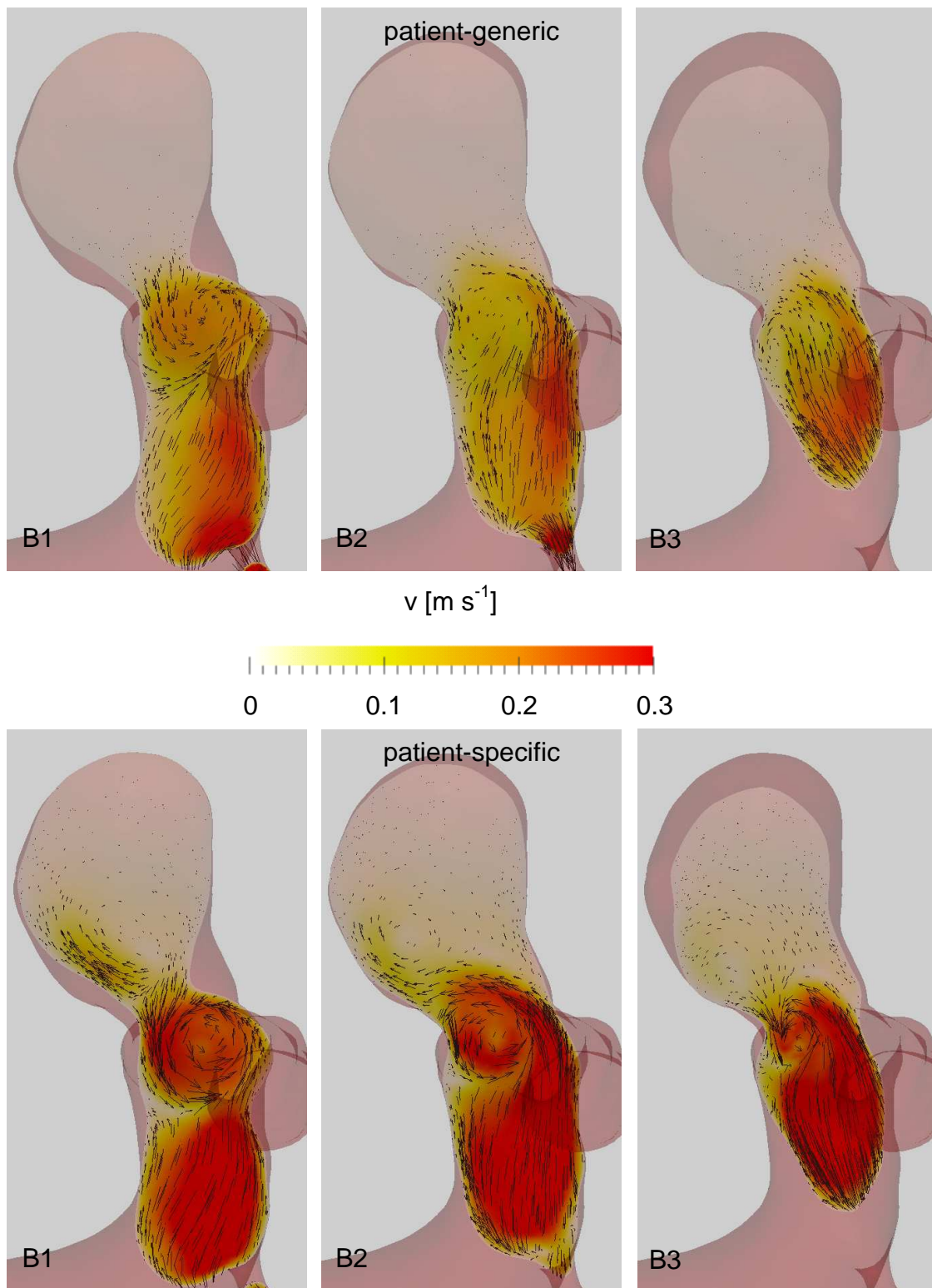


**Figure 4.9:** The velocity field in the vertical slices perpendicular to the MCA/ACA (B1 – 3; fig 4.4) with the boundary conditions based on the (top) RPG model and (bottom) RPS model.

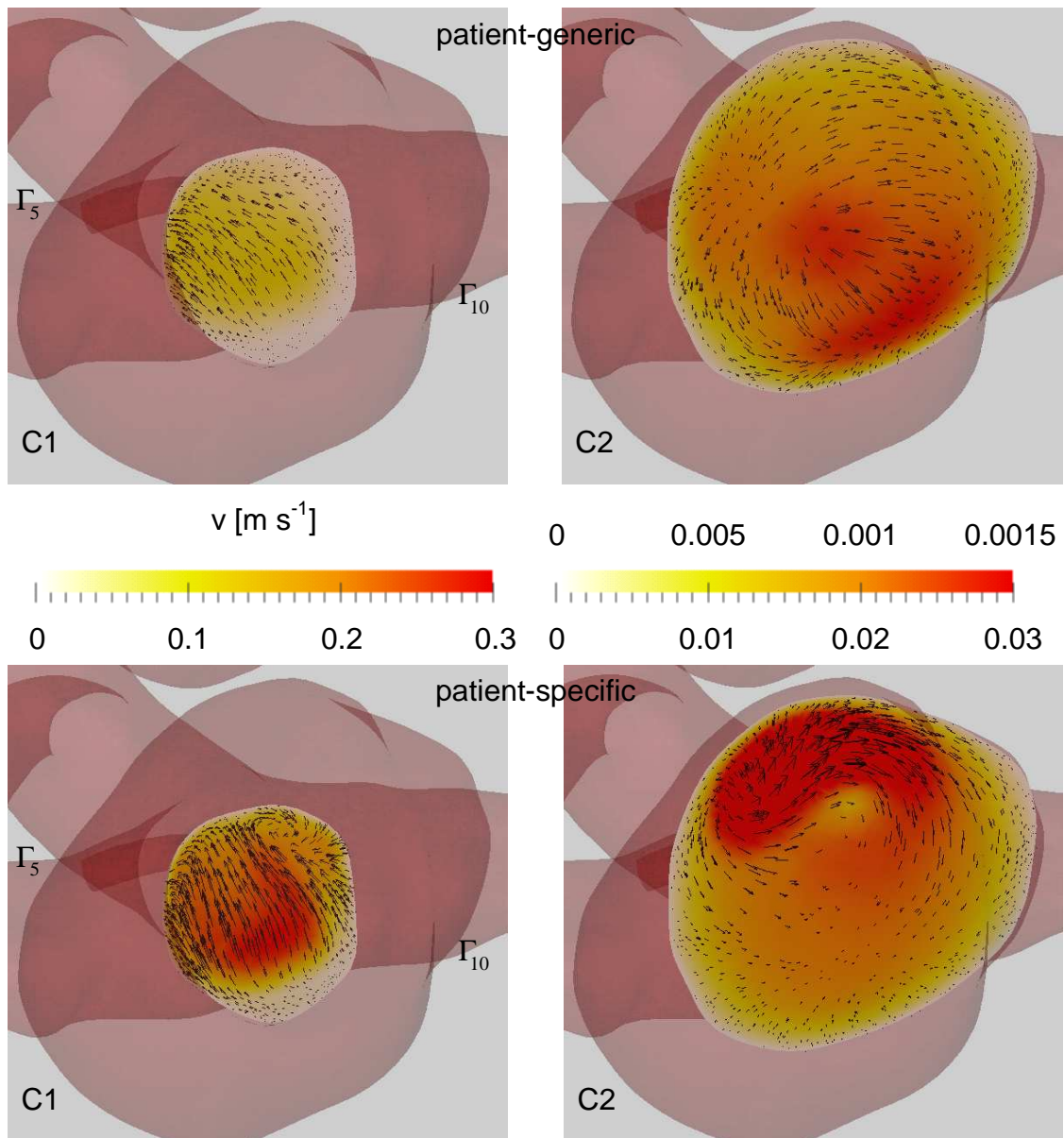


**Figure 4.10:** The velocity field in the neck and the aneurysmal sac (C1, 2; fig 4.4) with the boundary conditions based on the (top) RPG model and (bottom) RPS model. Note the differences in scaling needed to visualise the data.

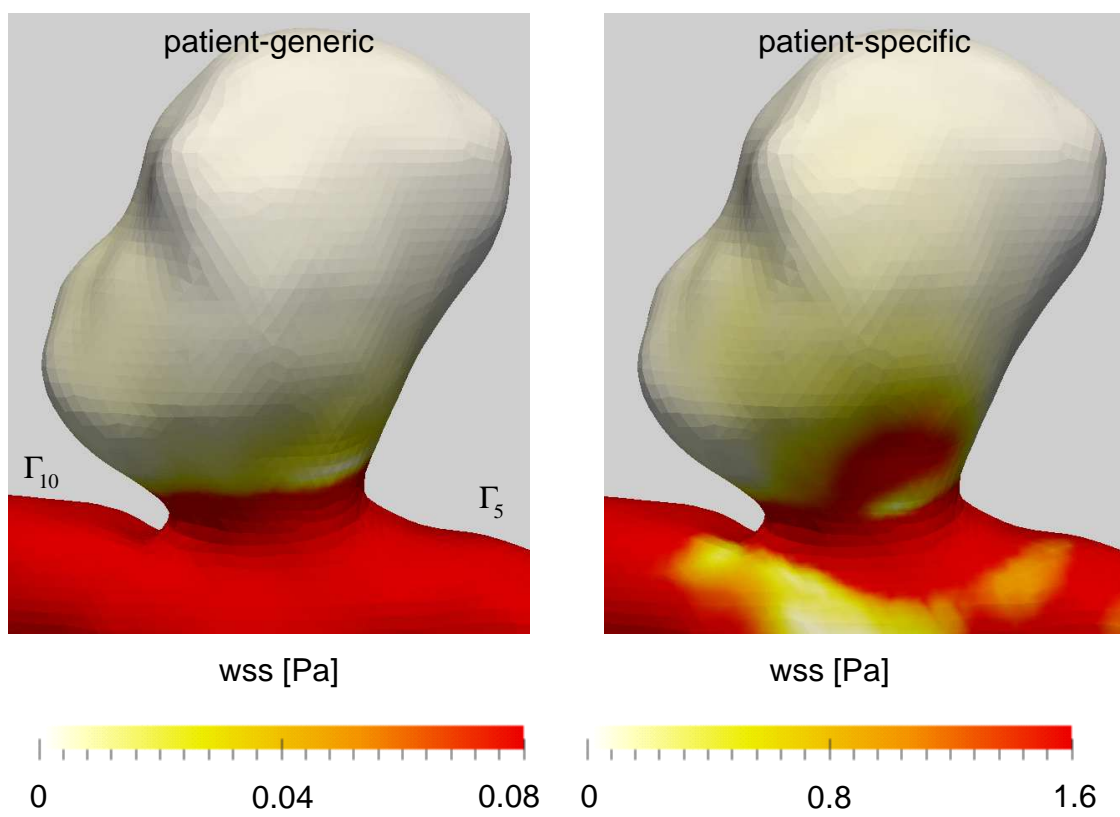


**Figure 4.11:** The wall shear stress with the boundary conditions based on the (top) RPG model and (bottom) RPS model. Note the difference in scaling.

## 4.4 Discussion and conclusions

The differences observed in the boundary conditions prescribed were expected to affect the velocity field and pressure throughout the 3D geometry in several ways (see the discussion in chapter 3). Overall, the mean flows in the patient-generic (RPG) model are lower than those in the patient-specific (RPS) model (fig 4.2 and table 4.1), with the exception of the flow through the PCoA and anterior choroidal artery (outlets 3 and 4). Indeed, the mismatch between the geometry and the boundary conditions results in an unrealistic pressure distribution when the flows from the RPG model are prescribed. The flow distribution over the branches adjacent to the aneurysm neck, the ACA and MCA (outlets 5 and 10), differs (table 4.1); the flow through the MCA is relatively low in the PG model. This causes a difference in flow pattern just proximal to the neck, e.g., the shear layer between the flow into the ACA and MCA observed in the RPS model. Moreover, the secondary flow in the ACA and MCA is stronger in the RPS model. Altogether, this results in higher velocities and a more complex vortex structure in the aneurysmal sac when prescribing RPS boundary conditions.

The velocities in the aneurysmal sac are low relative to the velocities in the parent arteries, especially in the RPG model. Considering the magnitude of the intra-aneurysmal velocities, small differences in modelling assumptions can have a significant effect on the resulting velocities and derived quantities such as the wall shear stress. For example, Torii et al. (2007) and Torii et al. (2009) reported that including wall distensibility may significantly affect the observed velocities and wall shear stresses if the intra-aneurysmal velocities are low.

Cebral et al. (2005b,c) suggested that the stability and complexity of the intra-aneurysmal vortex structure is an indicator for aneurysm stability. Other factors that have been associated with an increased rupture risk are the size of the impingement region caused by the inflow jet and locally high/low wall shear stresses or shear rates. Even considering only the end-diastolic flow, the complexity and strength of the intra-aneurysmal vortices is higher in the RPS model. The magnitude of the velocities, and therefore the wall shear stress, are a factor 20 lower in the RPG model. Finally, the region of high wall shear stress near the aneurysm neck observed in the RPS model is not present in the RPG model.

The end-diastolic flow was prescribed in order to reduce the complexity of the analysis. As the end-diastolic flow distribution is similar to the distribution of the mean flows, prescribing mean flows should give similar conclusions regarding patient-specific versus patient-generic modelling. Actually, the mean flows in the RPS model are even higher relative to the RPG model compared to diastolic flows (the RPG inflow through ICA is 78% of the RPS inflow in end-diastole, versus 62% when comparing the mean inflows), which would only enhance the differences in the velocity field shown here. In a pulsatile case, the differences can be expected to be even more pronounced as the amplitude is higher in the RPS model. The authors therefore believe, considering the differences already present when prescribing the end-diastolic flow, the pulsatile flow boundary conditions will only confirm and augment the differences presented here.

## 4.5 Conclusion

The intra-aneurysmal vortex and wall shear stress distribution shows remarkable differences, indicating patient-generic boundary conditions are not suitable to obtain a realistic representation of the intra-aneurysmal velocity field. Hence, the presented case study indicates that prescribing a different set of flow boundary conditions, which both appear to be within reasonable physiological limits, affect the characteristics of the intra-aneurysmal velocity field. This rises the question about the errors induced when prescribing boundary conditions based on patient-generic data. Therefore, more patients should be evaluated in order to establish with statistical relevance whether patient-specific data are required to obtain a reliable representation of the factors that are thought to be involved in aneurysm stability. Obviously, the influence of measurement and postprocessing errors should also be considered in this survey, as the introduction of patient-specific modelling is only relevant if the parameters needed can be obtained with an accuracy that exceeds the inter-patient variability. Considering the significant variations in vascular geometry observed *in vivo* David and Moore (2008), this inter-patient variability is expected to be high enough to induce a significant inter-patient variability of the flow.

### 4.5.1 Acknowledgement

The authors gratefully acknowledge the contribution Richard Lycett from the University of Sheffield.

## CHAPTER FIVE

# The influence of contrast agent injection on physiological flow in the circle of Willis<sup>I</sup>

---

X-ray videodensitometry allows *in vivo* flow measurements from gradients in contrast agent concentration. However, the injection of contrast agent alters the flow to be measured. Here, the temporal, spatial, and inter-patient variability of the response to injection are examined. To this purpose, an injection is prescribed in the internal carotid in a 1D wave propagation model of the arterial circulation. Although the resulting effect of injection is constant over a cardiac cycle, the response does vary with the location within the cerebral circulation and the geometry of the circle of Willis. At the injection site, the injection partly suppresses the incoming blood flow, such that the distal flow is increased by approximately 10%. This corresponds to approximately 20% of the injection rate added to the blood flow during injection, depending on the vascular geometry. In the communicating arteries, the flow direction is reversed during injection. Since the measured flow is not equal to the physiological blood flow, the effect of injection should be taken into account when deriving the flow from travelling contrast agent.

---

<sup>I</sup> *Reproduced from:* G. Mulder, A. C. B. Bogaerds, P. Rongen, F. N. van de Vosse (2011). The influence of contrast agent injection on physiological flow in the circle of Willis *Medical Engineering and Physics*, 33, p. 195–203.

## 5.1 Introduction

The influence of local haemodynamic parameters, such as wall shear stress, on the initiation and progression of various cardiovascular diseases, has been widely accepted (Caro et al., 1978). Since most of these parameters cannot be measured *in vivo*, models describing local flow provide useful information in understanding of the disease progression and the planning of disease treatment. However, the arterial tree is a complex system of compliant vessels of which the diameter decreases significantly towards the peripheral circulation. Furthermore, local pressure and flow waves are altered by wave reflections from transitions (e.g., bifurcations and variations in wall properties) elsewhere in the arterial tree. Since these features are not easily captured by one single-scaled mathematical model, a multi-scale approach is frequently applied.

Detailed velocity fields in an arterial segment (i.e., a small longitudinal section of the arterial tree) can be obtained with 3D patient-specific models (David and Moore, 2008; Cebal et al., 2005b; Castro et al., 2005). However, since these models are computationally expensive, and can only be feasibly applied to small to medium sized arterial segments, a 1D wave propagation model is more suitable for the computation of pressure and flow waves throughout the arterial tree (Hughes and Lubliner, 1973; van de Vosse and Stergiopulos, 2011). In the multi-scale approach, a 0D or lumped-parameter model describes the peripheral circulation, providing boundary conditions for the truncated arteries of the 1D model (Stergiopulos et al., 1992; Bessems et al., 2007; Sherwin et al., 2003). The 1D model, in turn, provides boundary conditions for the 3D patient-specific geometry (Passerini et al., 2009; Vignon-Clementel et al., 2006).

Recognising the relevance of appropriate pressure and flow boundary conditions for 3D patient-specific geometries, several groups (see e.g., Alastruey et al. (2007b) and Raymond et al. (2009)) adopted this multi-scale approach in order to model the cerebral vasculature. However, the 1D geometry and boundary conditions are commonly based on patient-generic data. A true patient-specific model requires, apart from its geometry, patient-specific flow and pressure boundary conditions. Therefore, *in vivo* pressure and flow measurements are needed.

For the cerebral circulation, several *in vivo* flow measurements techniques are available, such as Trans-Cranial Doppler ultrasonography (TCD) (Bartels, 2002), Phase-Contrast MR imaging (PC-MR) and videodensitometry from x-ray images (Shpilfoygel et al., 2000; Waechter et al., 2008). In TCD, the velocities in the arteries of interest cannot be measured simultaneously. Furthermore, this method is highly handler-dependent, and 10 – 15% of the patients lack the temporal window required in TCD (Tsivgoulis et al., 2009). Although PC-MR does allow simultaneous velocity measurements in large arteries (Tanaka et al., 2006; Ford et al., 2005a), velocities in small arteries further down the arterial tree cannot be retrieved accurately due to saturation and the small amount of pixels covering the lumen (Tanaka et al., 2006).

X-ray can be applied in all patients, and its high temporal and spatial resolution allow flow measurements even in the small arteries (Shpilfoygel et al., 2000). Several methods to extract flow data from x-ray cines are available, each with their own advantages and

drawbacks. However, since all videodensitometric methods rely on the propagation of contrast agent facilitated by the blood flow, an injection of contrast agent is required which is known to affect haemodynamics *in vivo* (Schröder et al., 1981; Spiller et al., 1983). This study focusses on the effect of this injection on the physiological blood flow using a 1D wave propagation model.

A contrast agent injection affects the blood flow at three time-scales (Schröder et al., 1981; Nornes et al., 1990; Morcos et al., 1998). Firstly, the total volumetric flow is increased instantaneously due to the injected volume, which is referred to as the direct effect. Secondly, the viscosity effect is the increase in peripheral resistance as the viscous contrast agent reaches the microcirculation. The magnitude and timing, typically a few seconds after the start of the injection, depend on the viscosity of the contrast agent and the location of injection. Finally, the pharmacological effect refers to the increase in flow due to vasodilation induced by the contrast agent. Again, the magnitude and timing, typically a few minutes after the start of injection, vary with different contrast agents, while the injected volume plays a role as well. In this study, only the direct effect is taken into account, as this is considered most relevant in the short period in which the flow measurements take place.

At the injection site, the injection partly suppresses the incoming blood flow, resulting in a distal flow increase which is smaller than the injection rate. The actual flow increase due to injection depends on the injection rate, as well as the peripheral resistance and compliance of the arterial tree. This indicates the increase in flow is not only patient-specific, but also depends on the site of injection and the site of measurement. In order to quantify the effect of the injection on the original blood flow, the ratio of the increase in flow and the original blood flow could be useful. However, since the blood flow tends to be very low at certain sites in the circle of Willis, this factor would become futile.

The flow increase during injection is directly related to the injection rate (Levin et al., 1977). In this study, it is assumed that the flow increase equals the fraction of the injection rate that adds to the physiological blood flow, i.e., the flow increase during injection is proportional to the injection rate. The factor of proportionality is used to examine spatial, temporal, and inter-patient variations of the response to an injection in the internal carotid artery. In order to examine inter-patient variations, three virtual patients are considered, the first having a complete circle of Willis. The other geometries tested are lacking either the anterior communicating artery or the posterior communicating artery, for those are variations of the circle of Willis commonly seen in patients (David and Moore, 2008).

## 5.2 Materials and methods

### 5.2.1 Governing equations for a single vessel

The governing equations for 1D wave propagation in incompressible fluids through distensible tubes, derived by Hughes and Lubliner (1973), are rewritten such that the pres-

sure  $p$  and flow  $q$  are the parameters for which the set of equations is solved. When considering an arterial segment with cross-sectional  $A(z, t)$  at axial position  $z$  and time  $t$ , the conservation of mass becomes

$$\frac{\partial A}{\partial t} + \frac{\partial}{\partial z}(A\bar{v}) + \Psi = 0, \quad (5.1)$$

where  $\bar{v}$  is the average velocity over the cross-sectional area. The source term  $\Psi$  enables modeling of small side branches. The cross-sectional area can be derived from the pressure using the relation

$$A(z, t) = A_0 + C_0(p - p_0) \quad \text{with} \quad C_0 = \frac{2\pi(1 - \mu^2)a_0^3}{hE}, \quad (5.2)$$

where in this study the compliance per unit length  $C_0$  is based on thin-walled cylinder theory for linear elastic materials. The Poisson ratio  $\mu$  and Young's modulus  $E$  characterise the mechanical properties of the wall material, while the geometrical parameters  $h$  and  $a_0$  are the wall thickness and vessel radius at the initial pressure  $p = p_0$ . By the substitution of (5.2),  $A\bar{v} \equiv q$ , and assuming  $\Psi = 0$ , (5.1) is written in terms of  $p$  and  $q$

$$C_0 \frac{\partial p}{\partial t} + \frac{\partial q}{\partial z} = 0. \quad (5.3)$$

In the derivation of the momentum balance, the velocity profile over the cross-sectional area is needed to estimate the frictional forces and the non-linear convection term (Hughes and Lubliner, 1973). Bessems et al. (2007, 2008) derived a velocity profile function assuming an inertia-dominated flow in the central core and friction-dominated flow near the vessel wall. After substitution of this velocity profile function, and neglecting body forces, the momentum balance becomes

$$\frac{\partial q}{\partial t} + \frac{\partial}{\partial z} \left( \delta_1 \frac{q^2}{A} \right) + \frac{A}{\rho} \frac{\partial p}{\partial z} = \frac{2\pi a}{\rho} \tau_w + \frac{\eta}{\rho} \frac{\partial^2 q}{\partial z^2}, \quad (5.4)$$

where  $\rho$  and  $\eta$  are the fluid density and dynamic viscosity respectively, and  $a$  is the local lumen radius. The wall shear stress  $\tau_w$ , which can be derived from the velocity profile function assuming axisymmetry (Bessems et al., 2007), reads

$$\tau_w = -\frac{2\eta}{(1 - \zeta_c)a} \frac{q}{A} + \frac{a}{4}(1 - \zeta_c) \frac{\partial p}{\partial z} \quad \text{with} \quad \zeta_c = (\max[0, 1 - \sqrt{2}/\alpha])^2, \quad (5.5)$$

where  $\zeta_c$  represents the square of the ratio between the radius of the inertia-dominated core  $a_c$  and lumen radius  $a$ . In large arteries, the Womersley number  $\alpha = a\sqrt{\rho\omega/\eta}$ , with  $\omega$  the angular frequency, is high (i.e.,  $\zeta_c \rightarrow 1$ ), and the flow is inertia dominated ( $a_c \rightarrow a$ ). Moreover, for low Womersley numbers ( $\zeta_c \rightarrow 0$ ) the flow is friction-dominated ( $a_c \rightarrow 0$ ).

The constant  $\delta_1$  is related to the velocity profile, and therefore to  $\zeta_c$ , according to

$$\delta_1 = \frac{2 - 2\zeta_c(1 - \ln\zeta_c)}{(1 - \zeta_c)^2}. \quad (5.6)$$

For large arteries ( $\zeta_c \rightarrow 1$ ) the influence of the non-linear term is important and  $\delta_1 \rightarrow 1$ , resulting in a non-linear term similar to the ones used in other studies, e.g Sherwin et al. (2003).

After substitution of (5.5), and (5.6) in (5.4), the  $(p, q)$ -system can be written as

$$\frac{\partial}{\partial t} \begin{bmatrix} p \\ q \end{bmatrix} + \mathbf{N} \frac{\partial}{\partial z} \begin{bmatrix} p \\ q \end{bmatrix} - \mathbf{D} \frac{\partial^2}{\partial z^2} \begin{bmatrix} p \\ q \end{bmatrix} + \mathbf{H} \begin{bmatrix} p \\ q \end{bmatrix} = \mathbf{f}, \quad (5.7)$$

with

$$\mathbf{N} = \begin{bmatrix} 0 & C_0^{-1} \\ \frac{A}{2\rho}(1 + \zeta_c) - \delta_1 \frac{q^2}{A^2} C_0 & \delta_1 \frac{2q}{A} \end{bmatrix}, \quad \mathbf{D} = \begin{bmatrix} 0 & 0 \\ 0 & \frac{\eta}{\rho} \end{bmatrix}, \quad (5.8)$$

$$\mathbf{H} = \begin{bmatrix} 0 & 0 \\ 0 & \frac{4\pi\eta}{\rho A(1 - \zeta_c)} + \frac{q}{A} \left( \frac{\partial \delta_1}{\partial z} - \frac{\delta_1}{A} \frac{\partial A_0}{\partial z} \right) \end{bmatrix}, \quad \mathbf{f} = \begin{bmatrix} 0 \\ 0 \end{bmatrix}.$$

To solve this set of equations, a Galerkin weighted residuals method is employed by discretisation of the spatial domain  $\Omega$  using sixth-order spectral elements. Time discretisation is achieved using a second-order backward differencing scheme and at each time step a Newton-Raphson iterative scheme is used to handle the non-linear terms.

## 5.2.2 Arterial network

At branching sites, three elements (i.e., three nodal points) need to be coupled in a single point. For laminar flow, the pressure and flow will not change over the transition, provided the length of the transition (e.g., a bifurcation) is much smaller than the wave length of the pressure and flow waves and the transition can be considered to be discrete (Reuderink, 1991). Therefore, the coupling constraints for the pressures  $p_i$  and flows  $q_i$ , with  $i = 1, 2, 3$ , of the adjacent elements are

$$\begin{cases} p_1 = p_2 = p_3, \\ \sum_{i=1}^3 \kappa_i q_i = 0, \end{cases} \quad (5.9)$$

representing continuity of pressure and conservation of mass respectively. The constants  $\kappa_i$  ( $\kappa = \pm 1$ ) relate the internal coordinate direction of the 1D spectral element under consideration to the position of the branching point. Here,  $\kappa_i = 1$  when the branching

site is connected to the last nodal point of the 1D element, while  $\kappa_i = -1$  when it is connected to the first.

### 5.2.3 Boundary conditions

At the aortic root the flow pulse as measured by Olufsen et al. (2000) is prescribed, whereas the terminal impedance is prescribed at the distal end of each truncated artery. The terminal impedance is modelled using a three-element windkessel model (Stergiopoulos et al., 1992; Westerhof et al., 2009), consisting of a resistance  $Z$  in series with a parallel combination of a capacitor  $C$  and another resistance  $R$ . Hence, the pressure and flow at the truncated arteries are related according to

$$\frac{\partial q}{\partial t} = \frac{1}{Z} \frac{\partial p}{\partial t} + \frac{p}{ZRC} - \left( \frac{Z}{R} + 1 \right) \frac{q}{ZC}, \quad (5.10)$$

and  $Z + R$  corresponds to the total peripheral resistance of the truncated branch,  $R_t$ . In order to minimise high frequency reflections at the transition from the 1D to the 0D domain, the characteristic resistance  $Z$  is chosen equal to the characteristic impedance of the truncated artery (Westerhof et al., 1971), hence

$$Z \equiv Z_0 = \sqrt{\frac{\rho h E}{2\pi^2(1-\mu^2)a_0^5}}. \quad (5.11)$$

The wall shear stress can be used to estimate the peripheral resistances per outlet (Murray, 1926). However, it is well-known that the wall shear stress is only constant throughout the body in rough approximation. Therefore, a physiological flow distribution is ensured by estimating the peripheral resistance per body part  $R_{BP}$  (Alastruey et al., 2007b), which is given by

$$R_{BP} = \frac{R_T}{\alpha_{BP}}, \quad (5.12)$$

where  $R_T$  is the total peripheral resistance of the human arterial system in normal conditions ( $R_T = 1.34 \cdot 10^8 \text{ Pa s m}^{-3}$ ; Stergiopoulos et al. (1992)) and  $\alpha_{BP}$  is the physiological fraction of the cardiac output entering each body part (table 5.1). Secondly, within a body part comprising  $N$  truncated arteries, it is assumed that the outflow of each truncated artery is proportional to its respective initial radius cubed  $a_0^3$  (Murray, 1926). The total resistance is then defined as

$$R_t = R_{BP} \frac{a_t^3}{a_0^3} \quad \text{with} \quad a_t^3 = \sum_{i=1}^N a_{0,i}^3. \quad (5.13)$$

Furthermore, the terminal compliance  $C$  for each truncated artery is assumed to be proportional to the flow fraction,  $R_T/R_t$ . Given that the sum of the compliances of the 1D segments and all 0D windkessel models equals the total compliance of the human body

**Table 5.1:** The fraction of the cardiac output CO supplying each body part.

Body part	fraction CO [-]	Reference
intercostals	0.07	
celiac trunc	0.13	Stergiopoulos et al. (1992)
kidneys	0.22	Guyton and Hall (1996)
mesenteric	0.18	Perko (2001)
legs	0.20	Itzchak et al. (1975)
arms	0.05	Amundsen et al. (2002); Gault et al. (1966)
head	0.15	Guyton and Hall (1996); Alastruey et al. (2007b)

(i.e.,  $C_T = C_{1D} + C_{0D}$ ), the terminal compliance is defined as

$$C = C_{0D} \frac{R_T}{R_t}, \quad (5.14)$$

with  $C_T = 10^{-8} \text{m}^3 \text{Pa}^{-1}$  (Chemla et al., 1998; Simon et al., 1979).

### 5.2.4 Virtual patients

The geometry (fig 5.1) consists of 60 arterial segments, which are defined by the lengths  $L$ , proximal and distal radii  $a_p$  and  $a_d$ , wall thickness  $h$  and elastic modulus  $E$  (table 5.3). An exponential reduction in radius over the length of an arterial segment has been observed in dogs (Anliker et al., 1971). However, as this relation does not hold for the more irregular tapering in man (Pedley, 1980), linear tapering is assumed here. For all arteries up to the neck, the radii are derived from the compliances of each segment given by Stergiopoulos et al. (1992) assuming thick-walled segments. Since our model assumes thin-walled segments, the wall thickness is derived from the segment compliances and radii using (5.2). The length and radii of the intracranial arteries are as described by Alastruey et al. (2007b) and David and Moore (2008), while the wall thickness is assumed to be 25 % of the initial radius (Alastruey et al., 2007b). Since the wall is considerably stiffer in the cerebral circulation (Hayashi et al., 1980), a Young's modulus  $E = 1.6 \text{MPa}$  is assumed for all intracranial arteries. The windkessel parameters (table 5.4) for each truncated artery are derived from the physiological flow distribution (table 5.1) and the arterial properties in table 5.3. Furthermore, a blood density  $\rho = 1.05 \cdot 10^3 \text{kg m}^{-3}$  and dynamic viscosity  $\eta = 4.5 \cdot 10^3 \text{Pa} \cdot \text{s}$  are used.

The parameter settings described above represent virtual patient I, who has a complete circle of Willis. Virtual patients II and III differ from I only in the geometry; the left PCoA (segment number 50; represents patient 2) and ACoA (segment number 60; represents patient 3) are absent. Since the flow through the communicating arteries usually is low, the radii of the adjacent arteries have not been altered to facilitate the slight increase in flow.

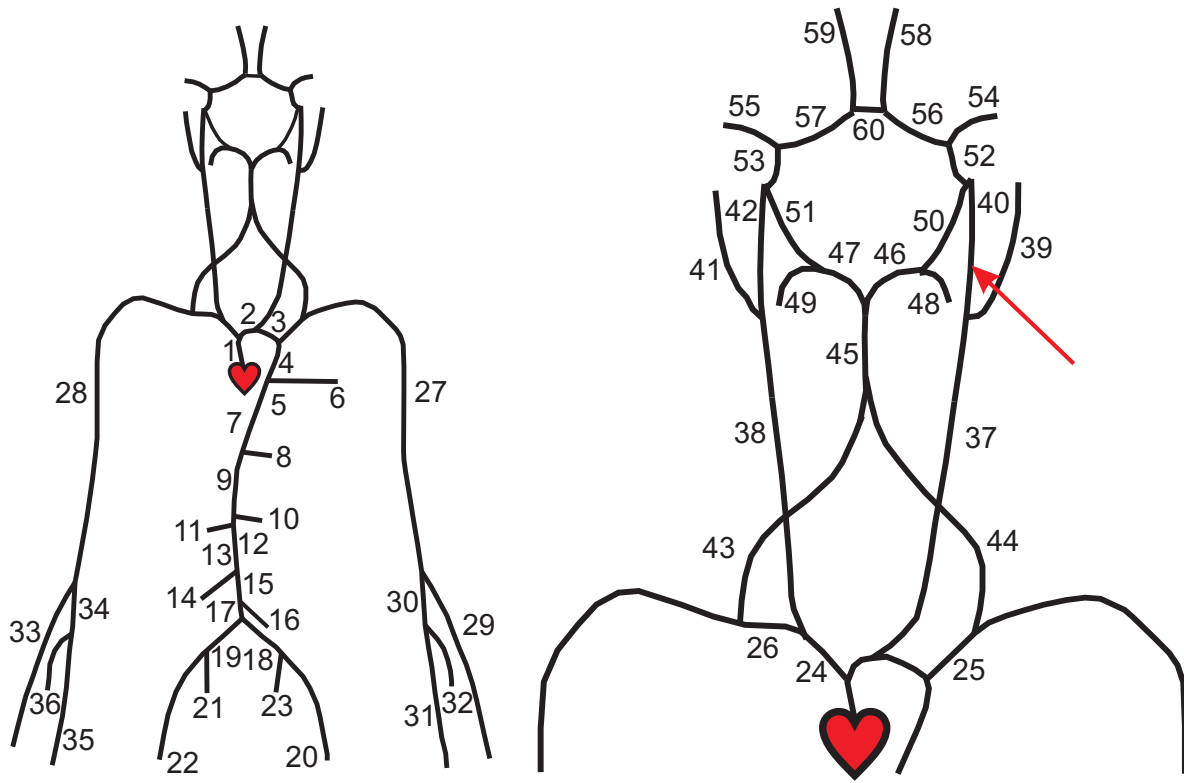


Figure 5.1: The geometry of the 1D model, where the segment numbers correspond to those in table 5.3. The arrow indicates the injection point.

### 5.2.5 Injection

During injection, the physiological flow is partly substituted by contrast agent, or equivalently, only a fraction of the injection rate is added to the original blood flow. This fraction is referred to as the  $m$ -factor (Waechter et al., 2008). Therefore, the flow during injection  $q_D$  at time  $t$  and location in the arterial tree  $x$  is described by

$$q_D(x,t) = q_B(x,t) + m(x,t)q_I(t), \quad (5.15)$$

where  $q_B$  is the physiological flow before injection, and  $q_I$  the injection rate. For  $0 < m < 1$ , the flow is elevated due to the injection, whereas  $m < 0$  indicates a reduction or reversal relative to the physiological flow.

The prescribed injection is described by

$$q_I(t) = \begin{cases} \frac{1}{2}q_{I,m}(\tanh(\beta(t-t_b)) - \tanh(\beta(t-t_e))), & \text{if } t_b \leq t \leq t_e, \beta \ll 1/(t_e - t_b); \\ 0, & \text{otherwise.} \end{cases} \quad (5.16)$$

Here,  $q_{I,m}$  is the maximum injection rate, and  $\beta$  describes the rate of increase and decrease (i.e., a measure of the acceleration) of  $q_I$  at the beginning and end of the injection

(times  $t_b$  and  $t_e$ , respectively). In order to test the validity of (5.15), several injections have been simulated (rates  $q_{I,m} = 1.0; 1.5; 2.0 \text{ ml s}^{-1}$  over  $t_e - t_b = 3$  seconds), which are modelled as extra inflow via a side branch in the ICA. In order to examine the time-constant involved in the response of the arterial model, the acceleration of the injection was varied ( $\beta = 5; 10 \text{ s}^{-1}$ ). Furthermore, the temporal and spatial variations of the  $m$ -factor are considered, using virtual patient I as described in the previous section. Since the effect of injection is also expected to be patient-specific, the influence of an absent PCoA or ACoA on the  $m$ -factors throughout the circle of Willis is examined.

### 5.3 Results

The flow and pressure curves (fig 5.2) in the aorta and arm are plotted at sample distances from the aortic root that are based on those used by Schaaf and Abbrecht (1972). Several features found in *in vivo* measurements are also observed in the numerical results. For increasing distance from the aortic root, indicated by the arrow, the pulse pressure increases whereas the peak flow decreases. The pressure pulse shows a dicrotic notch at end systole, after which the pressure gradually decays in diastole. At the aortic root, the systolic and diastolic pressure are approximately 130 and 70 mmHg, respectively. In the subclavian, two peaks in the pressure pulse become more distinct with increasing distance from the aortic root. Furthermore, the end-systolic back flow in the subclavian corresponds to the numerical results obtained by Schaaf and Abbrecht (1972).

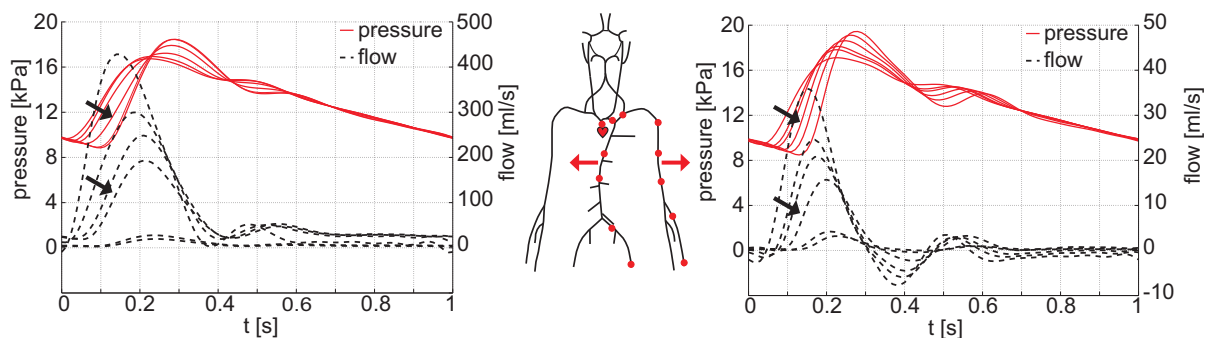


**Figure 5.2:** The pressure (solid) and flow (dashed) curves at several points (middle) in the aorta (left) and arm (right). The arrow indicates an increasing distance from the aortic root.

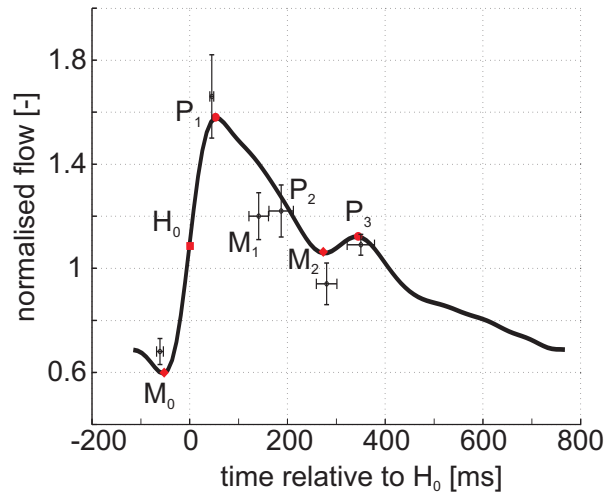


**Figure 5.3:** The normalised flow wave form in the ICA. The time is scaled to the average heart rate observed by Ford et al. (2005a).

**Table 5.2:** Characteristic points of flow curves in the ICA and VA; model vs. Ford et al. (2005a).

	Timing [ms]			Normalised flow [-]		
	model	Ford et al. (2005a) mean	$\sigma$	model	Ford et al. (2005a) mean	$\sigma$
M0	-53	-61	7	0.60	0.68	0.05
P1	53	45	4	1.58	1.66	0.16
M1	x	141	20	x	1.20	0.09
P2	x	187	25	x	1.22	0.10
M2	274	280	21	1.06	0.94	0.08
P3	344	350	28	1.12	1.09	0.04

Ford et al. (2005a) defined characteristic points in both the ICA and VA waveforms (fig 5.3), which have been normalised with their respective mean flows. Although they observed an extra peak just after the first peak P1, both the timing and magnitude of the other maxima and minima coincide (table 5.2). Similar observation could be made for the VA wave forms. Furthermore, the mean and peak flows ( $q_m = 4.6 \text{ ml s}^{-1}$  and  $q_p = 7.3 \text{ ml s}^{-1}$ ) in the ICA are within the reported range (Cebal et al., 2008; Ford et al., 2005a; Deane and Markus, 1997). The flow distribution over the inlets of the circle of Willis of ICA:BA = 40 : 20 corresponds to the *in vivo* flow division (Hendrikse et al., 2005; Tanaka et al., 2006), while the flow distribution over the outlets resembles that found by Tanaka et al. (2006).

During a  $2.0 \text{ ml s}^{-1}$  injection in the left ICA (arrow in figure 5.4), part of the physiological flow is suppressed by the contrast agent injection, resulting in a reduction of blood flow proximal to the site of injection (solid line). Obviously, the increase in flow distal to the point of injection (dashed line) does not correspond to the injection rate (dotted line),

confirming only a small part of the injection is added to the original flow.

During injection, the flow waveform corresponds to that before injection, suggesting the  $m$ -factor varies little in time. Indeed, when plotting the  $m$ -factor in time for several locations within the circle of Willis (fig 5.5), it is virtually constant over the cardiac cycle, indicating time-averaged flows can be used in (5.15). After the injection starts, the  $m$ -factor converges to its stable value within a cardiac cycle. Differences in acceleration  $\beta$  (dotted vs. solid) result in similar responses. Furthermore, the  $m$ -factor is independent of the injection rate for the range tested here ( $q_{I,m} = 1.0; 1.5; 2.0 \text{ ml s}^{-1}$ ).

The pressure increases slightly at the injection site, inducing an increase in pressure difference between the injection site and the arteries of the circle of Willis. However, as the Womersley number  $\alpha \simeq 1$  in the ICA, changes in pressure due to the injection travel with the relatively high wave speed  $c \simeq \frac{1}{2}\alpha c_0 = O(5 \text{ m s}^{-1})$ , where  $c_0$  the Moens-Korteweg wave speed (Pedley, 1980). Since the distance between the site of injection and the outlets of circle of Willis is typically smaller than 15 cm, the pulse caused by the injection should travel through the circle of Willis within 30 ms. Hence, the influence of the injection-induced extra pressure on the pressure differences will be short-lived, which corresponds to the overshoot observed in the  $m$ -factor, i.e., flow increase due to injection (fig 5.5).

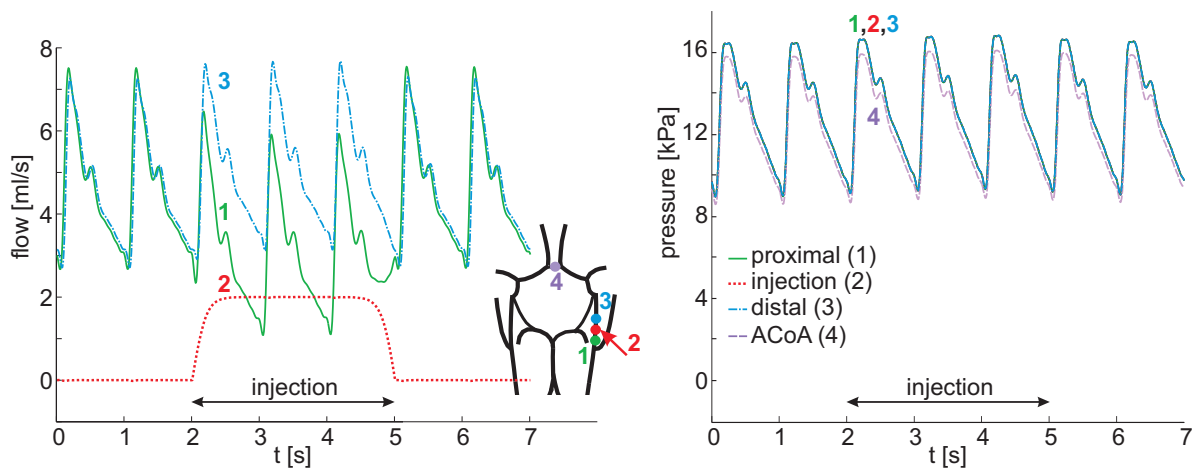


**Figure 5.4:** Flow curves (left) proximal (1) and distal (3) to the point of injection (2), while  $2.0 \text{ ml s}^{-1}$  is injected for 3 seconds. The influence of injection on the pressure curves (right) is small at the injection site (1, 2 and 3), as well as further down the tree (e.g. in the ACoA; 4).

Spatially, the  $m$ -factor shows significant variations (fig 5.6). In the left internal carotid, the injection results in a reduced inflow ( $m < 0$ ) proximal and increased total flow ( $m > 0$ ) distal to the injection site, which is in agreement with figure 5.4. Although the injection induces an increase in pressure in the order of magnitude  $10^1 - 10^2 \text{ Pa}$ , the change in pressure difference between the injection site and the outlets is about 10 Pa. The pressure difference between the outlets and their respective veins is in the order of magnitude 10 kPa, as the venous pressure is approximately zero. Within the circle of Willis however, the pressure differences are smaller. Therefore, the effect of injection is more noticeable

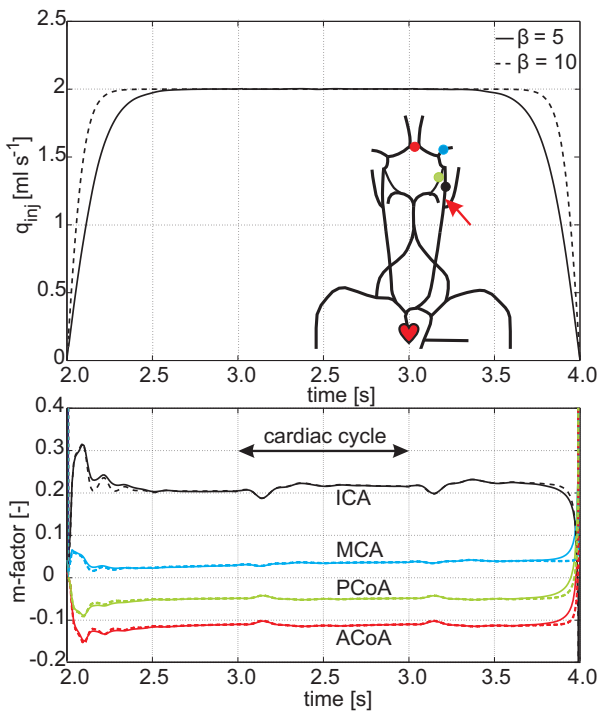


**Figure 5.5:** Temporal variations of the  $m$ -factor (bottom) at various locations (dots), while injecting (top) in the left ICA (arrow). Over the cardiac cycle used in all analyses, injection acceleration  $\beta$  has no significant effect on the  $m$ -factor.

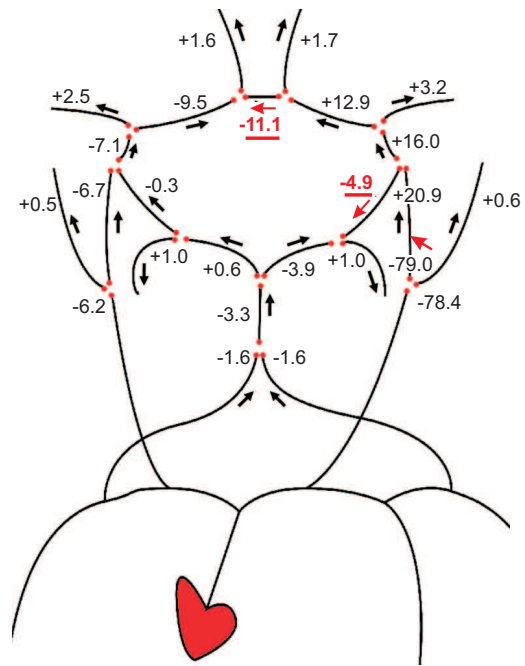


**Figure 5.6:** The  $m$ -factor [%] varies with the location. If the flow directions during injection (arrows) are reversed relative to those before injection, this is indicated by the underlined numbers.

within the circle of Willis, and the resulting redistribution of the flow allows the flow through all outlets to remain relatively unaffected.

Since the communicating arteries play an important role in counterbalancing the effect of injection, as indicated by the flow reversal, an absent or hypoplastic ACoA or PCoA will influence the  $m$ -factors throughout the circle of Willis. If either of the two communicating arteries is absent, the inflow through the left ICA proximal to the injection site is reduced even more (fig 5.6 vs. 5.7).

If the left PCoA is absent, the anterior circulation plays a more prominent role in counterbalancing the effect of injection, as indicated by the increased effect in ACAs and ACoA (fig 5.6 vs. 5.7a). Via the anterior circulation, the flow in the posterior arteries is affected. The flow through the right PCoA is reduced, while the flow entering the circle of willis through the BA remains unchanged. This results in a increased outflow through the PCA P2 segments, similar to the increase observed in a complete circle of Willis.

The absence of the ACoA results in an slightly increased response in the MCA, while the difference in response in the PCoA and the ICA proximal to the injection site is more pronounced (fig 5.6 vs. 5.7b). The blood flow towards the contralateral side of the circle of Willis is increased, reducing the inflow from the BA. Furthermore, the inflow through the contralateral ICA is increased.

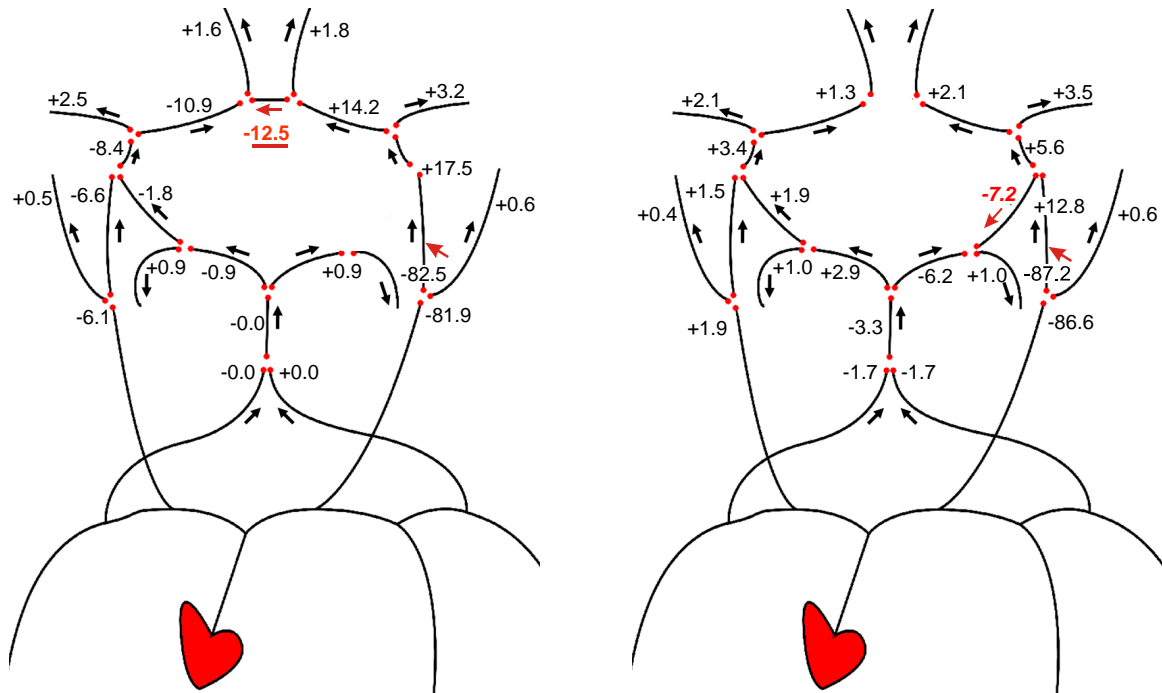


**Figure 5.7:** The influence of an absent (left) PCoA or (right) ACoA on the  $m$ -factor [%], for an injection rate of  $2.0 \text{ ml s}^{-1}$ . If the flow directions during injection (arrows) are reversed relative to those before injection, this is indicated by the underlined numbers.

In all three geometries considered here, mainly the outflow through the ACA A2 segments changed, whereas the rest of the outflows responded similarly due to the capacity of the circle of Willis to redirect flow. However, the response flow within the circle of Willis depends significantly on the geometry.

## 5.4 Discussion

The injection is modelled by prescribing an extra inflow in the internal carotid artery, where the injected fluid has the same properties as the blood. Although the dynamic viscosity  $\eta$  and density  $\rho$  of radio-opaque contrast agents usually differ from those of blood, in our model only the kinematic viscosity  $\nu = \eta/\rho$  is relevant in defining the fluid properties (equation 5.4 and 5.5). Since contrast agents often used in cerebral angiography (e.g., Ultravist<sup>®</sup> 300 and Omnipaque<sup>™</sup> 300) have kinematic viscosities that resemble that of blood ( $3 - 5 \cdot 10^{-6} \text{ m}^2 \text{ s}^{-1}$ ), the assumption of the injected fluid being the same as blood is reasonable. Furthermore, the effects of the presence of the catheter and its cross-sectional positioning in the artery on the local velocity fields (Mabon et al., 1978) are assumed to have a negligible effect on the flow and pressure waveforms throughout the arterial tree.

The shape of the injection rate used here differs from that used in literature, e.g., exponential decay (Waechter et al., 2008). However, the time-constant involved in the response to injection is small and the  $m$ -factor at a certain location is independent of the

injection rate, i.e., the  $m$ -factor converges to its stable value within a heartbeat regardless the acceleration. This indicates the shape of the injection curve used, does not affect the resulting  $m$ -factors.

As mentioned in the introduction, an injection of a radio-opaque contrast agent causes a response on three time-scales (Stoeter et al., 1984). The first part of the response is an increase of total flow due to the added volume flow during injection. This part of the response depends on the injection rate and the compliance and resistance of the vasculature, and can be modelled as described here. However, autoregulation controls the peripheral resistances in order to maintain sufficient blood flow to the brain. Typically, autoregulation restores the blood flow within 3 – 5 seconds after a disturbance (Aaslid et al., 1989; Aaslid, 2006; Moore et al., 2006), which indicates it would influence the  $m$ -factor at the end of a 3 second injection. Therefore, autoregulation should be incorporated by regulating the peripheral resistances in the windkessel models (Olufsen et al., 2002; Alastruey et al., 2007a).

About 1 to 1.5 seconds after injecting in the ICA (Stoeter et al., 1984), the more viscous contrast agent reaches the micro-circulation, resulting in an increase in peripheral resistance. This leads to a decrease in flow, and therefore, a decrease of the  $m$ -factor. However, since the significance of the viscosity effect is strongly related to the viscosity of the contrast agent used (Morris et al., 1982), this effect is not considered here.

Both the time of onset and duration of the pharmacological effect differ between different contrast agents. In general, this effect is not observed earlier than 5 seconds after the start of injection, while the duration varies from several seconds (Stoeter et al., 1984) up to several minutes (Pugh, 1996). As long as the measurements are performed within 5 seconds after starting the injections, and the time between two subsequent measurements is a few minutes (Schmitt et al., 2005), the pharmacological effect can be neglected as well.

Although several papers reported that contrast agent injection alters the physiological blood flow (Schröder et al., 1981; Warelius, 1967; Spiller et al., 1983), later studies tend to ignore this (Shpilfoygel et al., 2000; Schmitt et al., 2005; Tenjin et al., 1998). The results presented in this paper clearly show that, although the temporal variations of the  $m$ -factor can be neglected (fig 5.5), the spatial variations cannot (fig 5.6). Since the change in flow is proportional to the change in pressure difference, a small increase in pressure difference allows only for a small increase in total flow. This accounts for the reduced inflow proximal to the injection site and relatively small effect on the flow through the outlets. The flow is redistributed via collateral pathways, thereby inducing a flow reversal in the communicating arteries. *In vivo* pressure measurements during injection support the negligible pressure increase predicted by the model presented here (appendix B).

Evaluation of the effect of the results obtained with the present model on the flow extracted by means of videodensitometry is possible when the concentration profiles are included in the model. Taylor dispersion allows definition of an effective diffusion constant, accounting for shear augmented transport. This can be extended to more general velocity profiles and pulsatile flow, where axisymmetry is assumed (Azer and Peskin, 2007). However, secondary flow profiles induced by the for example high curvature in ICA will

affect the mixing of blood and contrast agent (Pedley and Kamm, 1988). Estimation of the effective diffusivity will not be straightforward due to the characteristics of the flow in the cerebral vasculature, e.g., variations of the secondary streamline patterns due to the high Dean number and the influence of the numerous junctions present. This geometrical complexity, and the idealisations required in the derivation of the effective diffusivity, result in no more than a rough qualitative indication (Pedley and Kamm, 1988), which is not suitable for quantitative modelling.

The  $m$ -factor depends on the vasculature, and therefore, is patient-specific. This means that the  $m$ -factor should be derived from patient measurements. Considering (5.15), the obvious measurement method would be to record two x-ray sequences, each with different injection rates. However, preliminary results on patient-specific measurement of the  $m$ -factor using this method are not promising, as the range of injection rates suitable for x-ray videodensitometric methods is small, and patient-dependent. If the injection rate is too low, the signal-to-noise ratio is too low; if the injection rate is too high, the lumen is completely opacified and the gradients in contrast agent concentration necessary in videodensitometry are lost.

The effect of injection on the flow is diminished within one cycle (fig 5.4). The time needed for the concentration agent to wash out of the ICA, estimated from the convection and length of the ICA, is about half a heartbeat. However, even though the contrast agent within the core of the ICA flow will have vanished within one cycle, some contrast agent may remain in the boundary layer. The transport of contrast agent in the boundary layer is related to the blood flow in the core, however, the variations will be smaller. Furthermore, it is unlikely that enough contrast agent remains to allow reliable flow curve extraction, especially since the secondary flow profiles increase the transport from the boundary layer to the core of the flow. More precise analysis is only possible with the aid of 3D models (virtual angiography, see e.g., Ford et al. (2005b)).

Even if the  $m$ -factors cannot be measured, the effect of injection should be taken into account when deriving the flow from travelling contrast agent, as the measured flow is not equal to the physiological blood flow. The injection might affect the results in both qualitative (e.g., virtual angiography (Cebral et al., 2007; Castro et al., 2006b; Ford et al., 2005b)), and quantitative studies (Asakura et al., 2003). For instance, *in vivo* flow measurements may be performed with the aim of obtaining patient-specific boundary conditions for a 3D arterial segment. In the internal carotid artery, ignoring the effect of injection would lead to an overestimation of about 10%. However, if flow reversal occurs, this will affect the velocity field in the 3D segment of interest. A 1D model is a suitable tool in examining the effects of a disturbance on the flow and pressure waves throughout an arterial tree, allowing improvement of the accuracy with which *in vivo* flow is measured with x-ray videodensitometric methods.

## 5.5 Conclusion

A 1D wave propagation model has been used to investigate the influence of contrast agent injection on the flow in the circle of Willis. The simulations show that the flows in the different branches are significantly affected by the contrast injection. A factor introduced to correct for this effect can be assumed constant over a cardiac cycle. However, spatial variations cannot be neglected, as the response to injection varies strongly throughout the vasculature and between patients. As a consequence, x-ray based assessment of flow in the circle of Willis should be interpreted with the greatest care.

**Table 5.3:** Geometrical data of the arterial tree (top; Stergiopoulos et al. (1992)) and the circle of Willis (bottom; Alastruey et al. (2007b); David and Moore (2008)).

Nr.	artery name	L [cm]	$a_p$ [cm]	$a_d$ [cm]	h [10 <sup>-2</sup> cm]	E [10 <sup>6</sup> Pa]
1	ascending aorta	4.00	1.470	1.440	13.9	0.4
2	aortic arch A	2.00	1.120	1.120	10.8	0.4
3	aortic arch B	3.90	1.070	1.070	9.9	0.4
4	thoracic aorta A	5.20	0.999	0.999	8.7	0.4
5	thoracic aorta B	10.4	0.675	0.645	8.1	0.4
6	intercostals	8.00	0.200	0.150	3.4	0.4
7	abdominal aorta A	5.30	0.610	0.610	7.3	0.4
8	celiac	1.00	0.390	0.390	5.1	0.4
9	abdominal aorta B	1.00	0.600	0.600	6.6	0.4
10/11	l./r. renal	3.20	0.260	0.260	4.0	0.4
12	abdominal aorta C	1.00	0.590	0.590	6.6	0.4
13	abdominal aorta D1	5.30	0.580	0.564	6.3	0.4
14	sup. mesenteric	5.90	0.435	0.435	5.6	0.4
15	abdominal aorta D2	5.30	0.564	0.548	6.2	0.4
16	inf. mesenteric	5.00	0.160	0.160	3.0	0.4
17	abdominal aorta E	1.00	0.520	0.520	5.5	0.4
18/19	l./r. common iliac	5.80	0.368	0.350	4.8	0.4
20/22	l./r ext. iliac	14.4	0.320	0.270	4.2	0.8
21/23	l./r. int. iliac	5.00	0.200	0.200	3.1	1.6
24	brachiocephalic	3.40	0.620	0.620	6.7	0.4
25/26	l./r. subclavian	3.40	0.423	0.423	5.4	0.4
27/28	l./r. brachial	42.2	0.403	0.236	5.0	0.4
29/33	l./r. radial	23.5	0.174	0.142	3.0	0.8
30/34	l./r. ulnar A	6.70	0.215	0.215	3.5	0.8
31/35	l./r. ulnar B	17.1	0.203	0.183	3.4	0.8
32/36	l./r. interosseous	7.90	0.091	0.091	1.9	1.6
37	l. common carotid	20.8	0.370	0.250	6.3	0.4
38	r. common carotid	17.7	0.370	0.250	6.3	0.4
39/41	l./r. ext. carotid	17.7	0.177	0.083	3.8	0.8
40/42	l./r. int. carotid A	17.7	0.200	0.200	5.0	0.8
43/44	l./r. vertebral	14.8	0.136	0.136	3.4	0.8
45	basilar	2.90	0.162	0.162	4.0	1.6
46/47	l./r. post. cerebral artery P1	0.50	0.107	0.107	2.7	1.6
48/49	l./r. post. cerebral artery P2	8.60	0.105	0.105	2.6	1.6
50/51	l./r. post. comm. artery	1.50	0.073	0.073	1.8	1.6
52/53	l./r. int. carotid B	0.50	0.200	0.200	5.0	1.6
54/55	l./r. middle cerebral artery	11.9	0.143	0.143	3.6	1.6
56/57	l./r. ant. cerebral artery A1	1.20	0.117	0.117	2.9	1.6
58/59	l./r. ant. cerebral artery A2	10.3	0.120	0.120	3.0	1.6
60	ant. comm. artery	0.30	0.074	0.074	1.9	1.6

**Table 5.4:** Parameters for the windkessel models prescribed at the truncated arteries.

Nr.	artery name	$Z$ [ $10^9 \text{ Pa s m}^{-3}$ ]	$R$ [ $10^9 \text{ Pa s m}^{-3}$ ]	$C$ [ $10^{-10} \text{ m}^3 \text{ Pa}^{-1}$ ]
6	intercostals	1.12	0.80	2.76
8	celiac	0.13	0.90	5.12
10/11	l./r. renal	0.31	0.91	4.33
14	sup. mesenteric	0.10	0.68	6.75
16	inf. mesenteric	0.91	14.80	0.34
20/22	l./r. ext. iliac	0.40	1.48	2.80
21/23	l./r. int. iliac	1.04	3.60	1.14
29/33	l./r. radial	1.70	16.50	0.29
31/35	l./r. ulnar B	0.96	7.57	0.62
32/36	l./r. interosseous	5.86	63.50	0.08
39/41	l./r. ext. carotid	5.80	14.10	0.27
48/49	l./r. PCA P2	4.09	5.76	0.54
54/55	l./r. MCA	2.22	1.68	1.36
58/59	l./r. ACA A2	3.14	3.46	0.81

## CHAPTER SIX

# Personalisation of CFD-based cerebral aneurysm flow analysis using pressure measurements in the carotid artery

---

It is well established that a 1D wave propagation model can be used to provide the input for a CFD based 3D analysis of intra-aneurysmal flow patterns. In earlier studies (see chapters 3 and 5) the importance of patient-specific versus patient-generic 1D modeling has been shown. At the outflow boundaries of the 1D wave propagation model, the terminal impedance can be prescribed via a 3-element windkessel model of which the terminal resistance and compliance need to be defined (see chapters 3 and 5). The ratio of mean pressure and mean flow defines the terminal resistance, which, together with the time constant describing the exponential decay in the diastolic part of the pressure curve, defines the terminal compliance. Mean pressure and flow as well as the diastolic decay, however, vary throughout the body and between patients. In this chapter the possibility to estimate the patient-specific time constants from measured pressure waveforms in the carotid artery is analysed. Hereto, the intra- and inter-patient variability of the time constant as well as the waveform characteristics are estimated from the pressure curves obtained from the internal carotid artery of 6 patients. The intra-patient variability as obtained from these data shows the feasibility of such a pressure waveform based procedure whereas inter-patient variability indicates its necessity.

## 6.1 Introduction

A 1D wave propagation model can provide boundary conditions for a 3D CFD model in a vascular segment of interest (chapter 3 and 4). Since patient-specific boundary conditions for the 1D model are needed to obtain representative velocity fields, measurements are necessary to obtain model parameters. The 1D boundary conditions used throughout this work are 3-element windkessel models consisting of characteristic impedance, resistance and compliance element. As the characteristic impedance is defined by the input geometry and material parameters, extracting patient-specific boundary conditions is reduced to obtaining the total peripheral resistance and the compliance of each windkessel model. In other studies, the peripheral resistances are often based on the outlet radius (Murray, 1926; Alastruey et al., 2007b). In chapter 3 however, it was shown that the geometry-derived boundary conditions for a 1D model of the cerebral vasculature were sensitive to relative small changes in the radius of the truncated arteries, especially considering the inaccuracies that are inevitably introduced during the processing of the vascular geometry. Alternatively, the resistances at the outlets could be derived from flow measurements. If the flows in all branches are known, the resistance can be estimated with the ratio of the mean pressure in the ICA to the mean flow through each outlet, assuming the pressure drop over the circle of Willis is small compared to the pressure itself. Since the flow distribution over the outlets is defined by the ratios of peripheral resistances at each outlet, the relative flows define the distribution of the total resistance of the cerebral circulation over the outlets of the circle of Willis.

Some studies use a single generic time constant as found in the aorta to estimate the peripheral compliances (Bessemers et al., 2007). However, the time constant depends on the location within the arterial tree; the large arteries are more compliant than those further down the tree, while the peripheral arteries account for most of the resistance. Therefore, the time constant in the outlets of the circle of Willis is expected to be significantly lower than in the aorta. In order to estimate a patient-specific compliance, the pressure curve can be used (Stergiopoulos et al., 1995). The differential equation describing the windkessel model can be integrated over the time, although this method of extracting the compliance requires measurements of both the pressure and flow waveform. Alternatively, the low-frequency impedance method (Laskey et al., 1990) assumes the flow is close to zero in diastole, such that the time constant describing the diastolic decay of the pressure pulse can be used to extract the compliance. In the cerebral circulation however, the diastolic flow is significantly different from zero (fig 3.5), resulting in an error when estimating the compliance in the way described above. In this chapter, it is shown that the estimation is improved noticeably if the diastolic flow is assumed to be some portion of the mean flow over a cardiac cycle.

The diastolic decay observed in the last part of the pressure wave provides enough information to derive boundary conditions for a 1D model of the circulation. However, a 3D model describing the arterial wall, either separately or in conjunction with the blood flow (Fluid Structure Interaction; FSI), requires the pressure curve over the full cardiac cycle. Characterisation of the flow and pressure waveforms in the main arteries could be used to derive boundary conditions for such computational models. Holdsworth et al. (1999)

evaluated the flow waveform in the common carotid artery measured with ultrasound in 11 healthy volunteers. In a similar study, Ford et al. (2005a) analysed the flow waveforms in the internal carotid and vertebral arteries measured with phase-contrast Magnetic Resonance in 17 patients. Characteristic points such as the maxima, minima and inflection point were defined. The characteristic points obtained from the gain-normalised flow waves showed remarkably low inter-patient variability. Moreover, a correlation between the peak flow and the mean flow was found, while an increased cardiac cycle was related to an increased diastolic decay. Both studies suggested that the characteristic waveforms could be used as boundary conditions in numerical simulations due to the scalability of both amplitude and cardiac cycle. However, the pressure waves were not included in these two studies, and these are needed to fully define computational models of the circulation.

In this chapter, the pressure curves obtained from the internal carotid artery of 6 patients were analysed. The objective is twofold: estimate the time constant describing the diastolic decay in order to evaluate the intra- and inter-patient variability, and evaluate the feasibility of deriving a typical pressure waveform in the internal carotid. First, the results from chapter 3 are used to introduce and show the advantage of taking into account the diastolic flow when deriving the time constant from pressure waves. Next, the individual cardiac cycles in each patient are used to evaluate the variability of the time constant. Finally, a preliminary evaluation of the normalised pressure waveforms is presented.

## 6.2 Materials and methods

### 6.2.1 Compliance from the pressure waveform and relative diastolic flow

The 3-element windkessel model is described by

$$\frac{\partial p}{\partial t} + \frac{1}{RC}p = \frac{1}{C} \left( \frac{Z}{R} + 1 \right) q + Z \frac{\partial q}{\partial t}, \quad (6.1)$$

where  $Z$  is the characteristic impedance of the outlet vessel and  $C$  the peripheral compliance relating the pressure  $p(t)$  to the flow  $q(t)$ . The total peripheral resistance  $R + Z$  is the ratio of the mean pressure  $\bar{p}$  and flow  $\bar{q}$ , while the compliance can be derived from the diastolic decay of the pressure by fitting an exponential with time constant  $\tau = RC$ . In the aorta, the diastolic flow is approximately zero, such that the solution to (6.1) becomes

$$p(t) = p_0 e^{-(t-t_0)/\tau}, \quad (6.2)$$

where  $p_0$  is the pressure at onset of the diastolic decay at the time  $t_0$ . However, the zero flow assumption is not valid in the cerebral circulation. In order to improve the accuracy with which the compliance can be extracted, the diastolic flow is assumed to be a fraction of the mean flow over the cardiac cycle, i.e.,  $q_d = \zeta \bar{q} = \zeta \bar{p} / (R + Z)$ . Substituting this

assumption into (6.1) and including the constant in the time derivative yields

$$\frac{\partial(p - \tilde{p})}{\partial t} = -\frac{1}{RC}(p - \tilde{p}), \quad (6.3)$$

with  $\tilde{p} = \zeta \bar{p}$ . After substituting the end-diastolic pressure  $p_1$  at time  $t_1$  into the general solution to this differential equation, i.e.,

$$p(t) - \tilde{p} = (p_0 - \tilde{p})e^{-(t-t_0)/\tau}, \quad (6.4)$$

rewriting gives the time constant

$$\tau = -\frac{t_1 - t_0}{\ln \frac{p_1 - \tilde{p}}{p_0 - \tilde{p}}}. \quad (6.5)$$

In the special case of zero diastolic flow, e.g. in the aorta,  $\zeta = 0$  and (6.4) reduces to (6.2).

In order to evaluate the effect of incorporating a fraction of the mean flow,  $\tau$  has been derived from the pressure curves in outlet 4, 6 and 9 of the patient-specific 3D domain presented in chapter 3 (fig 3.2) as obtained with the patient-specific Alastruey and Raymond models (APS and RPS model, respectively; see chapter 3). For small  $\zeta$ , the decay is underestimated ( $\frac{\partial p}{\partial t}$  too small), i.e.  $\tau$  is overestimated (fig 6.1). The value of  $\zeta$  for which the estimated time constant corresponds to the prescribed time constant, indicated by the dotted lines in figure 6.1, is about 0.5 to 0.6 for the APS and RPS models, respectively. This is in the same order of magnitude but slightly smaller than the computed  $\frac{q_d}{\bar{q}}$ , since the flow decrease during diastole is not taken into account.

The error on the estimated time constant when using  $\zeta = 0.5$  ranges from 1 to 30% for both models, compared to 130 to 230% when  $\zeta = 0$ . Therefore, incorporating the diastolic flow improves the estimated cerebral time-constant  $\tau$  considerably.

## 6.2.2 Data acquisition

In this study, two separate and independently acquired pressure data sets are used. The first set consists of 4 patients in whom the pressure was measured using a fluid-filled catheter situated in the internal carotid at C2-level (Hôpitaux Universitaires de Genève, Geneva). The measurement was performed over 10 seconds. The second data set (2 patients) was obtained with a pressure wire (ComboWire, Vulcano) situated 1 cm distal to the catheter tip (Royal Hallamshire Hospital, Sheffield). The measurement was performed over about 300 seconds. All patients involved gave their informed consent.

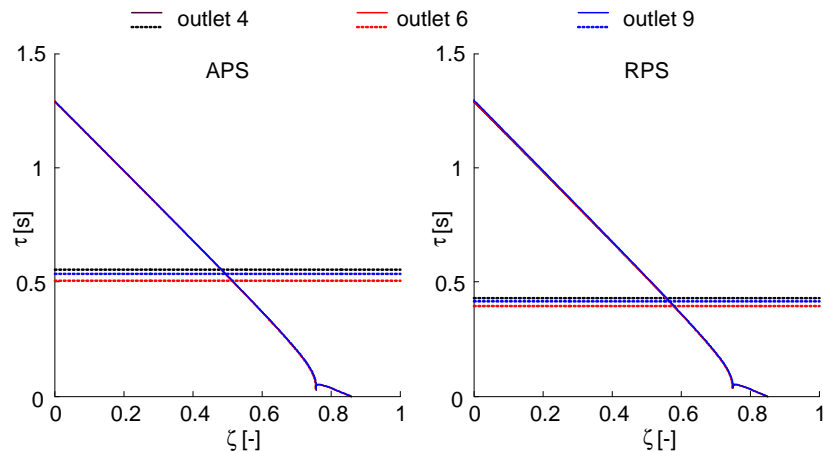


**Figure 6.1:** The estimated time constant  $\tau$  (solid) in the APS model (left) and RPS model (right) decreases as  $\zeta$  increases. For  $\zeta \approx 0.5$  the estimated time constant equals the prescribed time constant (dashed).

### 6.2.3 Data processing

In order to extract the time constant  $\tau$ , the data needs to be split up into cardiac cycles. Each cycle was identified by the end-diastolic minimum ( $M_0$  in figure 5.3). The time-constant describing the diastolic decay was calculated (equation 6.5) for each cycle, where  $t_0$  was defined as the first time step for which the pressure dropped below the cyclic average and  $t_1$  the last time step of the respective cycle. The influence of incorporating the diastolic flow on the calculated time constant was assessed by assuming a diastolic flow of zero ( $\zeta = 0$ ) and half of the mean flow ( $\zeta = 0.5$ ).

In order to assess the intra-patient variability of the waveform, all cycles were gain-normalised with their respective cyclic mean. Furthermore, the time was normalised with the duration of the respective cardiac cycle,  $T$ . The normalised pressure curves were resampled in order to compute an averaged waveform for each patient. These averaged waveforms are compared to evaluate the feasibility of the definition of a characteristic pressure waveform.

## 6.3 Results

### 6.3.1 Gain-normalised pressure waves

The intra-patient variability of the gain normalised pressure wave ( $p/\bar{p}$ ) seems low in all data sets (fig 6.2 and 6.3). Typical features, such as a double systolic peak, observed in the averaged waveforms (solid lines) correspond to the features observed in the individual waveforms (dashed lines). Furthermore, the diastolic decay appears to follow the same curve, indicating the intra-patient variation of the time-constant should small.

As can be depicted from figure 6.4 (left), indeed, the intra-patient variability of the time-constant is low, especially for the case that a non-zero diastolic flow ( $\zeta = 0.5$ ) is used in

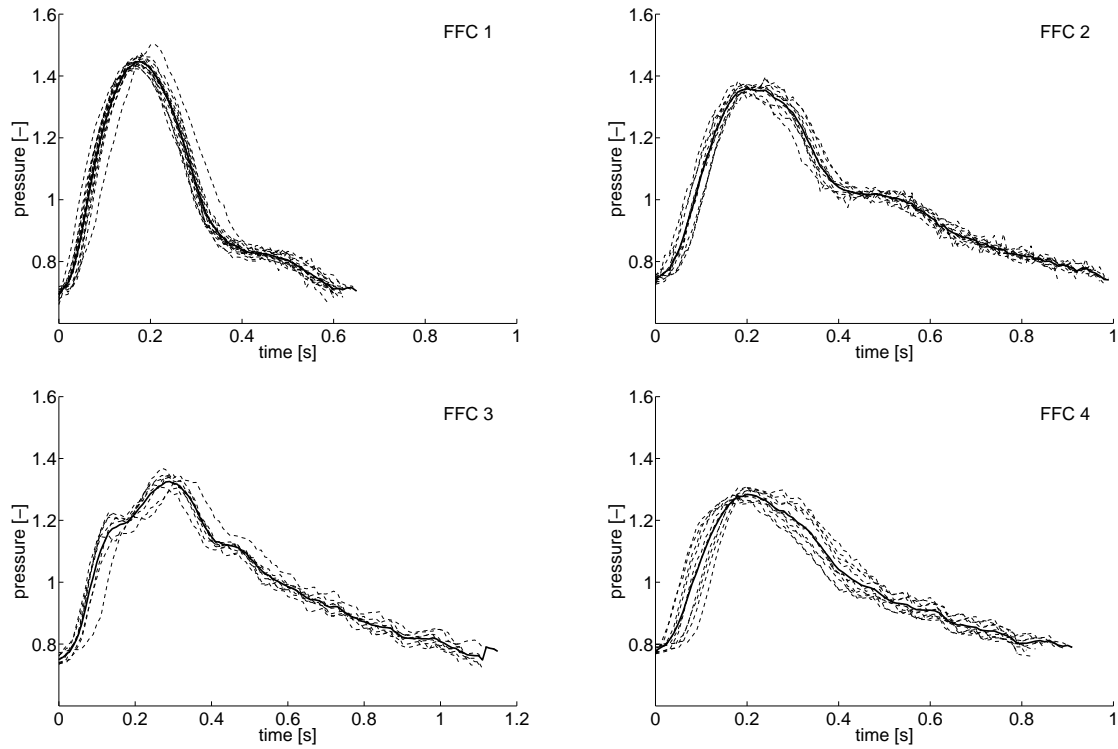


**Figure 6.2:** The gain-normalised pressure over the first 10 cardiac cycles (dashed) and the averaged waveform (solid) derived from the pressure measurements with a fluid filled catheter (4 patients).

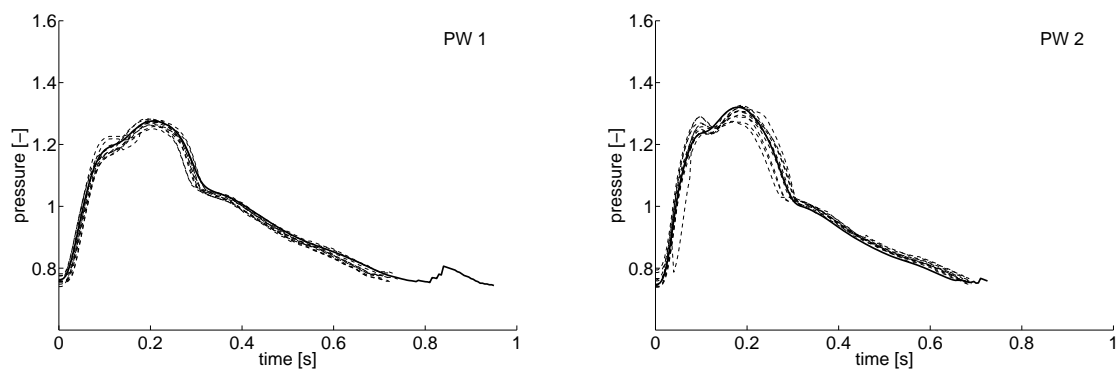


**Figure 6.3:** The gain-normalised pressure over the first 10 cardiac cycles (dashed) and the averaged waveform (solid) derived from the pressure measurements with a pressure wire (2 patients).

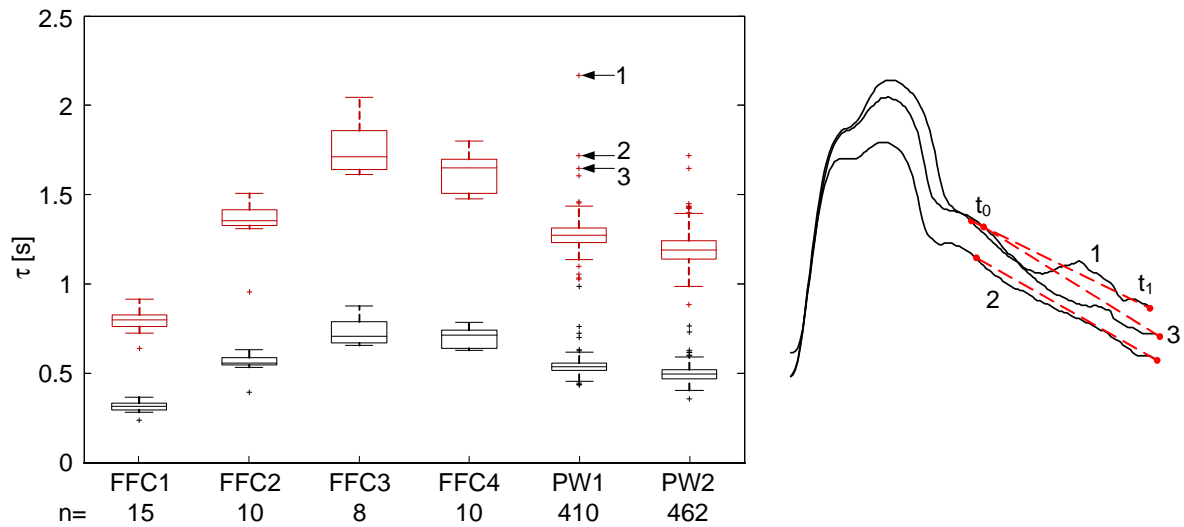


**Figure 6.4:** (left) The time constant  $\tau$  derived from the pressure measurements with a fluid filled catheter (FFC1 – 4) and a pressure wire (PW1,2) calculated from the  $n$  cardiac cycles available in each measurement. Assuming a zero diastolic flow (i.e.,  $\zeta = 0$ ; red) results in significantly higher time constants compared to those obtained with  $\zeta = 0.5$  (black). (right) The waveforms corresponding to 3 outliers observed in the PW1 data, with the dots corresponding to the  $t_0$  and  $t_1$  used in the calculation.

**Table 6.1:** The cyclic mean of the pressure, heart rate and time constant (mean  $\pm$  SD) for two samples of the PW2 data (fig 6.5).

	Pressure [mmHg]	Heart rate [bpm]	Time constant [s]
Sample 1	93 $\pm$ 3.8	88 $\pm$ 0.8	0.52 $\pm$ 0.02
Sample 2	103 $\pm$ 4.6	91 $\pm$ 1.5	0.47 $\pm$ 0.03

its derivation. In the patient with the largest number of cardiac cycles available (PW2) the standard deviation of the blood pressure was 22%, while the variation in the extracted time constant was about 8% when the diastolic flow was taken into account ( $\zeta = 0.5$ ), even including the outliers. Furthermore, the waveforms corresponding to the outliers in the computed time constants show some irregularities in the diastolic decay (fig 6.4 right). Although the number of patients included is too small to allow firm conclusions, the results suggest that the inter-patient variability is significantly lower than the effect of assuming a zero diastolic flow (fig 6.4 left; red  $\zeta = 0$  versus black  $\zeta = 0.5$ ).

In the patients included, the derived time constants are fairly constant in time, except for a jump observed in the PW2 data set (fig 6.5). This jump corresponds to a jump in the pressure, although changes in mean arterial pressure alone do not explain the decrease of the time constant (see equation 6.5). Comparison of two samples (100s; boxes in figure 6.5) reveals that the pressure and heart rate are increased in the second sample, while the time constant appears to be slightly lower (not significant; table 6.1).

**Table 6.2:** The heart rate [bpm] and the corresponding duration of the cardiac cycles (mean $\pm$ SD) per patient (FFC = fluid-filled catheter; PW = pressure wire), the time constant  $\tau$  extracted using  $\zeta = 0$ , and the normalised time constant  $\tau/T$ .

Patient	HR	T [s]	$\pm$	SD	$\tau$ [s]	$\pm$	SD	$\tau/T$ [-]	$\pm$	SD
FFC 1	98	0.61	$\pm$	0.02	0.31	$\pm$	0.03	0.51	$\pm$	0.07
FFC 2	63	0.96	$\pm$	0.04	0.57	$\pm$	0.04	0.59	$\pm$	0.06
FFC 3	55	1.09	$\pm$	0.03	0.73	$\pm$	0.08	0.67	$\pm$	0.09
FFC 4	71	0.85	$\pm$	0.04	0.70	$\pm$	0.06	0.82	$\pm$	0.11
PW 1	80	0.75	$\pm$	0.02	0.54	$\pm$	0.04	0.72	$\pm$	0.07
PW 2	90	0.67	$\pm$	0.02	0.50	$\pm$	0.04	0.75	$\pm$	0.08

### 6.3.2 Time-gain-normalised pressure waves

The end-diastolic averaged pressure waves show some irregularities due to the intra-patient variability of the heart rate (fig 6.3; PW1), which means that averaged pressure at the end of the cycle is dominated by the few relatively long cardiac cycles. In order to avoid these irregularities the time could be normalised. Furthermore, since the heart rates vary significantly between patients (table 6.2), the normalisation of the time is also needed to allow inter-patient comparison of the averaged pressure waves. In figure 6.6 the time-gain-normalised pressure waves averaged over the cycles are presented.

The FFC3, PW1 and PW2 waveforms show a double systolic peak (fig 6.6). The peak in the FFC1 wave is more pronounced with a higher peak value and lower minima compared to the systolic peaks in the other measurements. Furthermore, the systolic peak is wide relative to the duration of the diastolic decay (see also figure 6.2), although this effect is reinforced by the normalisation of the time. Although the diastolic pressure decays of figure 6.6 suggests that a normalised time constant  $\tau/T$  could be used, the data given in table 6.2 illustrate that significant differences are still found.

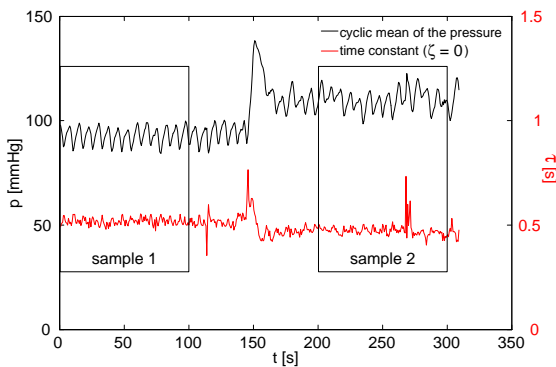


**Figure 6.5:** The cyclic averaged pressure (black) and the time constant (red) both show a jump; the pressure increases while the time constant decreases.

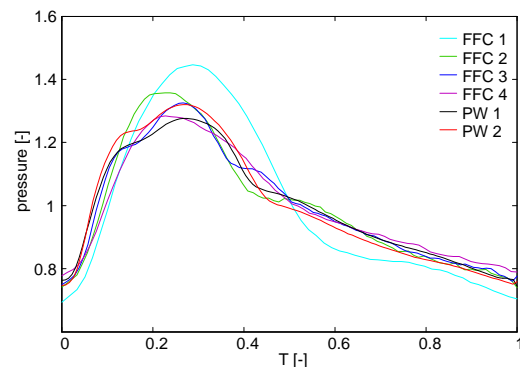


**Figure 6.6:** The averaged waveforms from all patients, i.e., normalised in pressure and time, resampled and averaged.

## 6.4 Discussion

Inter-patient analysis of the averaged extracted waveforms reveals small but notable variations in peak value, peak width and diastolic decay (fig 6.6), with the exception of the FFC1 pressure wave. It should be noted that the time scaling used here is inadequate. In reality, differences in the heart rate typically result in differences in the duration of the diastolic phase, while the scaling used here alters both the diastolic and the systolic phases. The error introduced by this scaling method is most evident in the FFC1 pulse (fig 6.6), as the cardiac cycle in this patient deviates most from 1s (table 6.2).

Intra-patient variations in waveforms are smaller still (fig 6.2 and 6.3), indicating that waveforms are independent of the changes in the mean blood pressure in time (the waves in fig 6.5). This means that any *in vivo* pressure measurements can be short, which promotes measuring the pressure non-invasively via ultrasound assessment of the carotid artery wall motion. Furthermore, the low intra-patient variability suggests the pressure waveform is scalable.

These intra- and inter-patient variations in the extracted time constant are small relative to the effect of assuming zero flow in the diastolic phase. This suggests more research is needed on the assumptions made when deriving boundary conditions for computational models of the circulation. In order to establish the relevance of patient-specific modelling of the peripheral compliance and the assumptions made when extracting the time constant, the sensitivity of the computational models to variations in the compliance should be assessed.

In PW2, a jump of in the time constant was observed, which coincides with a jump in the blood pressure. While changes in the average pressure do not influence the time constant extracted from the measured pressure waveform (see equation 6.5), changes in the pulsatility and duration of the cardiac cycle will. Since an increase of the mean arterial pressure is partially facilitated by an increase in heart rate, the variation in the time constant observed is likely to be related to a change in heart rate. Indeed, in sample 1 the heart rate was significantly lower than in sample 2 (beats per minute), and the average blood pressure the first sample was lower (table 6.1). If the heart rate and blood pressure increase, the linear decrease of the numerator in (6.5) dominates the logarithmic increase of the denominator, resulting in an overall decrease of the time constant.

A major limitation of this study is the small number of patients included. Furthermore, the pressure data was gathered at different institutions and with different devices, and it is well-known that both factors influence patient measurement outcome. The offset in the pressure measurement performed with the fluid-filled catheter might be inaccurate, since a height difference between the catheter ends (one in the patient and one connected to the device) introduces a static pressure. However, even assuming a height difference of 10 cm, the induced pressure would be 1 kPa, which is small compared to the average pressure expected *in vivo* (about 12 kPa). The ComboWire contains a small membrane of which the deformation is translated to a pressure. As the temperature in the body is significantly higher than room temperature, a drift is observed after the wire is inserted. This introduces some inaccuracies as the zero pressure is set outside the body.

## 6.5 Conclusion

The assumption of zero diastolic flow affects the extracted time constant describing the pressure decay significantly. The analysis presented here suggests that the intra-patient variability of both the pressure waveform and the extracted time constant are low, although a larger patient study is needed to confirm this. The low intra-patient variability shows the feasibility of pressure measurements.

The results of this study indicate a patient-generic waveform might be found, provided adequate time-scaling is used. However, a larger patient cohort is needed to substantiate this, and to determine the variability of the waveform characteristics. A sensitivity analysis based on this variability would reveal the possibilities and relevance of patient-generic waveforms and the degree of personalisation needed.

Even if a characteristic pressure waveform can be defined, the time constant describing the diastolic decay is sensitive to variations in waveform, as indicated by the significant inter-patient variations observed. Therefore, the time constant defining the diastolic pressure decay should be determined in a patient-specific way using time resolved measurements of carotid artery pressure and the flow distribution over the outlets.

### 6.5.1 Acknowledgement

The authors gratefully acknowledge the contribution Stuart Coley from the Royal Hallamshire Hospital in Sheffield and Olivier Brina from the Hôpitaux Universitaires de Genève, Geneva.

## CHAPTER SEVEN

### Discussion, conclusions and recommendations

---

## 7.1 General discussion

Cerebral aneurysms are localised dilatations of the arterial wall in the brain, which may be prone to rupture. As the resulting haemorrhage is associated with high mortality and morbidity rates, indicators for the rupture risk are sought. Cerebral aneurysm growth is influenced by haemodynamical factors, which are commonly estimated by means of a Computational Fluid Dynamics (CFD) model of a small 3D patient-specific segment of the arterial tree using patient-generic or partially patient-specific boundary conditions. The aim of this research was to investigate how the reliability of the model-based representation of the velocity field in the aneurysmal sac can be improved by replacing patient-generic boundary conditions with patient-specific ones. Furthermore, since statistical relevance requires the analysis of a large number of patient data, the value of a vortex identification method allowing automated analysis of the 3D velocity field rather than 2D slices was assessed (chapter 2). Although extra insight in the complex intra-aneurysmal flow patterns was obtained, the mesh densities needed to obtain accurately-identified vortex cores are high, which would increase the already high computational costs of 3D patient-specific models.

In literature, boundary conditions applied to the 3D vascular segment of interest modelled with CFD are commonly based on patient-generic data, e.g., averaged waveforms or waves extracted from a 1D wave propagation model with a patient-generic geometry. However, as the geometry of the cerebral vasculature shows significant inter-patient variability (David and Moore, 2008), the flow distribution is likely to show similar inter-patient variations.

In chapter 3, a 1D wave propagation model was used to compute the pressure and flow waves throughout the cerebral circulation, with the cerebral vascular geometry based on either patient-generic data (Alastruey et al., 2007b; Reymond et al., 2009) or patient-specific data (Mulder et al., 2011a). The presented model setups resulted in different flow distributions and waveforms, i.e., different boundary conditions for the 3D vascular segment of interest. In order to assess the influence of those differences on the 3D intra-aneurysmal velocity field, the end-diastolic flows extracted from a patient-generic and a patient-specific model were prescribed at the truncated arteries of the 3D segment (chapter 4). The intra-aneurysmal velocity fields showed significant differences, e.g., the strength and complexity of the intra-aneurysmal vortex. Furthermore, an area of relatively high wall shear stress was observed only in the patient-specific model.

The striking differences indicate that more reliable model assumptions based on patient-specific data are needed. In order to validate these modelling assumptions, *in vivo* measurements of blood flows is necessary. Several methods to measure blood flow or velocities are being developed, each with different strengths and drawbacks. If, for instance, x-ray videodensitometric methods are used, the injection of contrast agent needed to visualise the blood affects the physiological blood flow. Due to the collateral pathways in the cerebral circulation, connecting the major arteries, estimating the effect of injection on the physiological flow is not straightforward. In chapter 5, the 1D wave propagation model is used to estimate the spatial and temporal variations due to the injection. The

flows over the outlets were affected equally, while the effect on the flows through the segments within the circle of Willis was less consistent. Furthermore, the variations in vascular geometry, for example a missing communicating artery, alter the effect of injection. The model predicted an insignificant increase in pressure during injection, which corresponds to the *in vivo* measurements presented in appendix B.

Characteristic gain-normalised flow waveforms in the supplying arteries have been defined by Ford et al. (2005a) and Holdsworth et al. (1999), which can be scaled with patient measurement of the mean flow providing boundary conditions for numerical models. Pressure waves could aid the definition of the boundary conditions for patient-specific 1D wave propagation models, and are needed when the loading state of the arterial wall is of interest. No well-defined typical pressure waveform is available in literature. The preliminary results in chapter 6 indicate the possible definition of such a typical pressure waveform. Although the number of patients included was too small for any statistical relevance, the results suggest that a typical waveform can be defined provided the cardiac cycle is scaled such that the systolic phase remains unchanged.

As reported by Singh et al. (2009), clinicians distrust the results obtained with CFD models. The results presented in chapter 3 and 4 indicate that indeed more research is needed to obtain reliable models that can be introduced into clinical practice with confidence. In order to define and validate modelling approaches, *in vivo* measurements are needed. A possible work flow for those measurements is discussed in the following section.

## 7.2 Work flow

The velocity field in the aneurysmal sac can be obtained with a 3D CFD model. Considering clinical practice and the limitations of current technology, measuring the flow and pressure at the boundaries of the 3D arterial segment of interest in each patient is undesirable and often not possible. Furthermore, in order to minimise the risk of rupture during the procedure, performing the pressure and flow measurements either non-invasively at more accessible locations or at a reasonable distance from the aneurysm is preferable. A 1D wave-propagation model facilitates the computation of pressure and flow pulses throughout the cerebral circulation, allowing extraction of local boundary conditions given a geometry and pressure and flow waves at some distant location.

The vascular tree can be extracted from 3D-RA, CTA or MRA data, defining the geometry of the 1D model. Although contrast-enhanced Magnetic Resonance Angiography (MRA) provides high resolution images, the measurement-time is significantly longer than that of 3D-RA. A problem involved in this method is the enhancement of the veins, and again an injection of contrast agent is required. This can be circumvented by time-of-flight MRA, but this method relies on high flows and is therefore known to miss partially large aneurysms. The advantage of MRA is the possibility to measure the flow distribution over the supplying arteries with phase-contrast MRA. Unfortunately, the flow distribution over the small outlet branches cannot be measured due to resolution issues. Applying videodensitometry to a x-ray sequence does allow flow measurements in small

arteries, although the required injection does alter the flow to be measured. Fortunately, 1D models in which the injection was included suggested that the influence of the injection on the flow through afferent arteries of the circle of Willis was in the same order of magnitude (Mulder et al., 2011a). This allows measuring the flow distribution over the outlets within the field of view, and therefore, estimation of the boundary conditions as described below.

At each outlet of the 1D model, the three-element windkessel model (Westerhof et al., 1971) can be prescribed, consisting of a resistance in series with a parallel combination of a capacitor and another resistance. This model reduces errors associated with the reflection of high frequency waves observed when the original two-element windkessel model as introduced by Frank (1899) is prescribed. Furthermore, all parameters can be estimated from the geometry, flow and pressure measurements. Although the model proposed by Stergiopoulos et al. (1999) offers further improvement, by reducing errors associated with the reflection of low frequency waves, this introduces an additional parameter which is not defined by the available patient data.

The first resistance is defined by the input geometry and material parameters, since this resistance is equal to the characteristic impedance of the truncated artery in order to avoid high frequency reflections at the outlet (Westerhof et al., 1971). Therefore, extracting patient-specific boundary conditions is limited to fitting the other resistance and the compliance of each windkessel model.

In order to estimate the second resistance, the sum of the two resistances at each outlet is determined, since this represents the peripheral resistance per outlet. The peripheral resistances are commonly based on the outlet radius (Murray, 1926; Alastruey et al., 2007b) or a patient-generic flow distribution (Reymond et al., 2009). The former is highly sensitive to small variations of the outlet radius, and therefore, to inaccuracies in the geometry. The latter is patient-generic, and therefore unsuitable in defining a patient-specific model as was aimed for here. Instead, the resistances at the outlets should be derived from flow measurements. If the absolute flows are known, the resistance can be estimated with the ratio of the mean pressure in the ICA and the mean flow through each outlet, assuming the pressure drop over the circle of Willis is small compared to the measurement error. However, since the flow distribution over the outlets is defined by the ratios of peripheral resistances at each outlet, the relative flows define the distribution of the total resistance of the head over the outlets of the circle of Willis. This reduces the effect of measurement errors, such as induced by the increase of flow due to the injection of contrast agent (Mulder et al., 2011a). Furthermore, the actual flows will vary with the cardiac output and body positioning, while the variations in flow distribution over the main outlets is assumed to be relatively low.

Several methods are available to estimate the peripheral compliances in three-element windkessel models from a measured pressure pulse  $p(t)$  (Stergiopoulos et al., 1995), such as the low-frequency impedance method (Laskey et al., 1990), distribution of the peripheral compliance according to the flow distribution (Alastruey et al., 2007b), and the integral method (Shim et al., 1994). The first method assumes the flow is close to zero in diastole, such that the time constant describing the diastolic decay of the pressure pulse

can be used to extract the compliance. Some studies use a single generic time constant as found in the aorta to estimate the peripheral compliances (Bessems et al., 2007). However, the time constant depends on the location within the arterial tree; the large arteries are more compliant than those further down the tree, while the peripheral arteries account for most of the resistance. Therefore, the time constant in the outlets of the circle of Willis is expected to be significantly lower than in the aorta. The main advantage of this approach is that a pressure measurement in the internal carotid artery would suffice. In the cerebral circulation however, the diastolic flow is not equal to zero (fig 3.5), resulting in an error when estimating the compliance. The estimation is improved significantly if the diastolic flow is assumed to be some portion of the mean flow over a cardiac cycle (chapter 6). Alternatively, the differential equation describing the windkessel model can be integrated over the time. This method allows retrieving the prescribed compliance when testing it with the model, but does require both the pressure and flow waveform.

Visualisation and treatment procedures that require the insertion of a catheter enable invasive pressure measurements by means of a pressure wire. However, less invasive and less expensive alternatives should be considered in other cases. The pressure waveform can be approximated from the change in diameter of the Common Carotid Artery (CCA) over a cardiac cycle and pressure measurements at a more accessible location, such the brachial artery (Vermeersch et al., 2008). Another reason to measure the pressure is the fact that it defines the stress state of the arterial wall. Even though it is not possible to measure the wall properties *in vivo*, recording the aneurysmal wall displacement over a cardiac cycle while measuring the pressure allows estimation of the stiffness. In the future, this approach would allow monitoring of adaptation of the wall, thereby providing information on the stability of the aneurysm. Hence, this could be a key indicator in the decision whether or not to intervene.

## 7.3 Conclusions

Intra-aneurysmal flow patterns and wall shear stresses are both candidates parameters for aneurysm stability assessment. These parameters vary when obtained by 3D CFD using patient-generic boundary conditions, rather than patient-specific boundary conditions. Thus it is the critical conclusion of this work that patient-generic boundary conditions may lead to erroneous conclusions regarding aneurysm stability assessment.

Based on the case study presented in this work, it is recommended to include more patients in order to determine the significance of these differences. Furthermore, only the 1D geometry was extracted from patient data. A patient-specific 1D model would be improved by flow and pressure measurements to estimate the boundary conditions and will be required for validation of models describing the cerebral blood flow.

This additional research would compliment the conclusions of this work, as summarised by the proposed work flow illustrated in figure 7.1, which requires three input parameters: geometry, flow and pressure. Firstly, the vascular geometry is extracted from imaging data such as 3D-RA or MRA data. Assuming a patient-generic Young's modulus,

the characteristic impedance  $Z$  can be derived. Secondly, the mean flow distribution over the outlets is determined using video-densitometry in order to obtain the peripheral resistances. Finally, the pressure in the carotid artery is assessed non-invasively. The latter two data sets can be used to calculate the cerebral time-constant  $\tau$ , defining the compliances of the peripheral vasculature at each outlet. These steps have been shown here to offer improvements in the modelling of cerebral aneurysms in each of their respective areas, the combination of which leads to an improved model for aneurysm stability assessment.

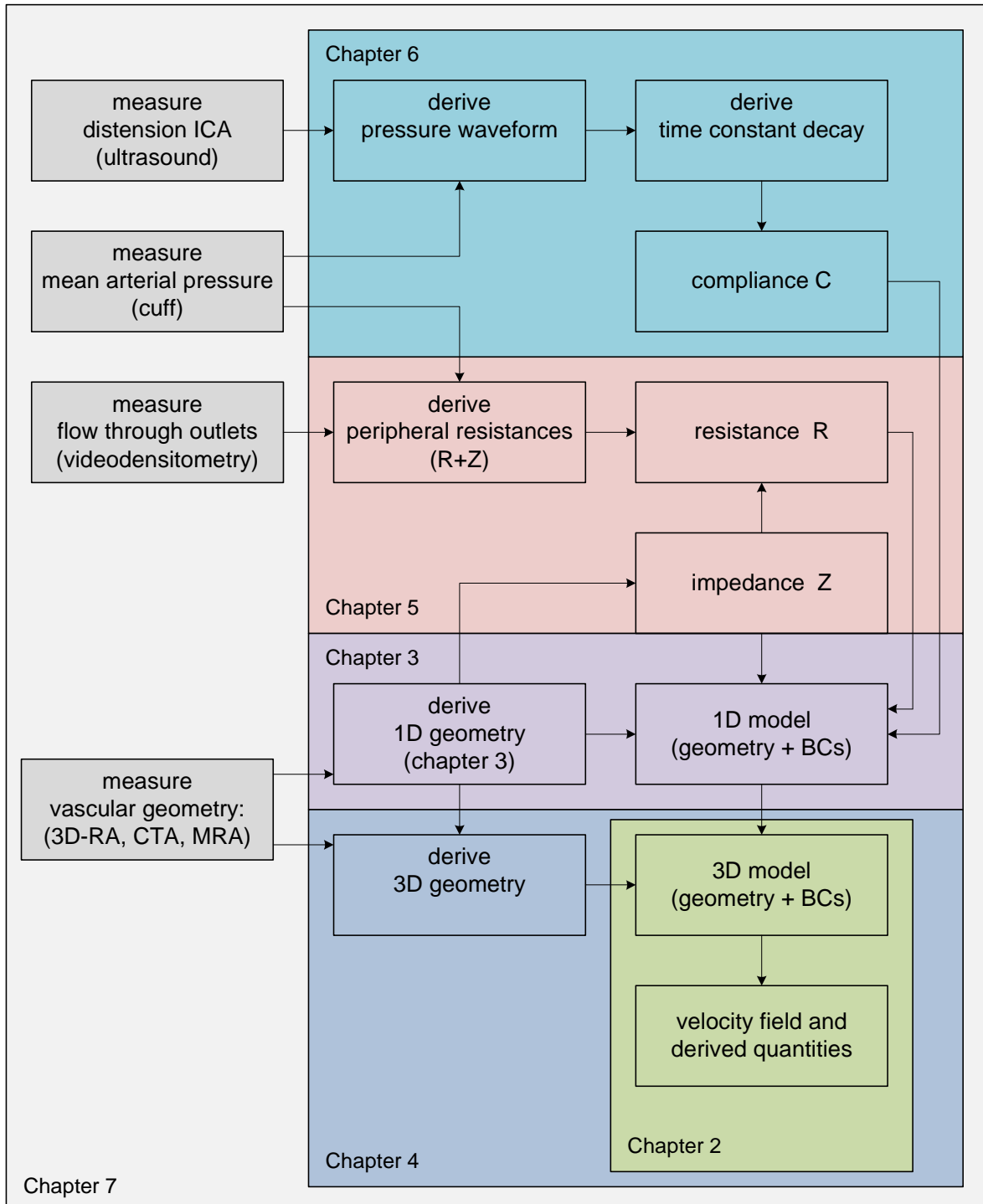


**Figure 7.1:** Overview of the proposed work flow, the measurements required (gray blocks; left), and the relation to the chapters in this thesis.



## APPENDIX A

### Geometry and boundary conditions of the 1D model

---

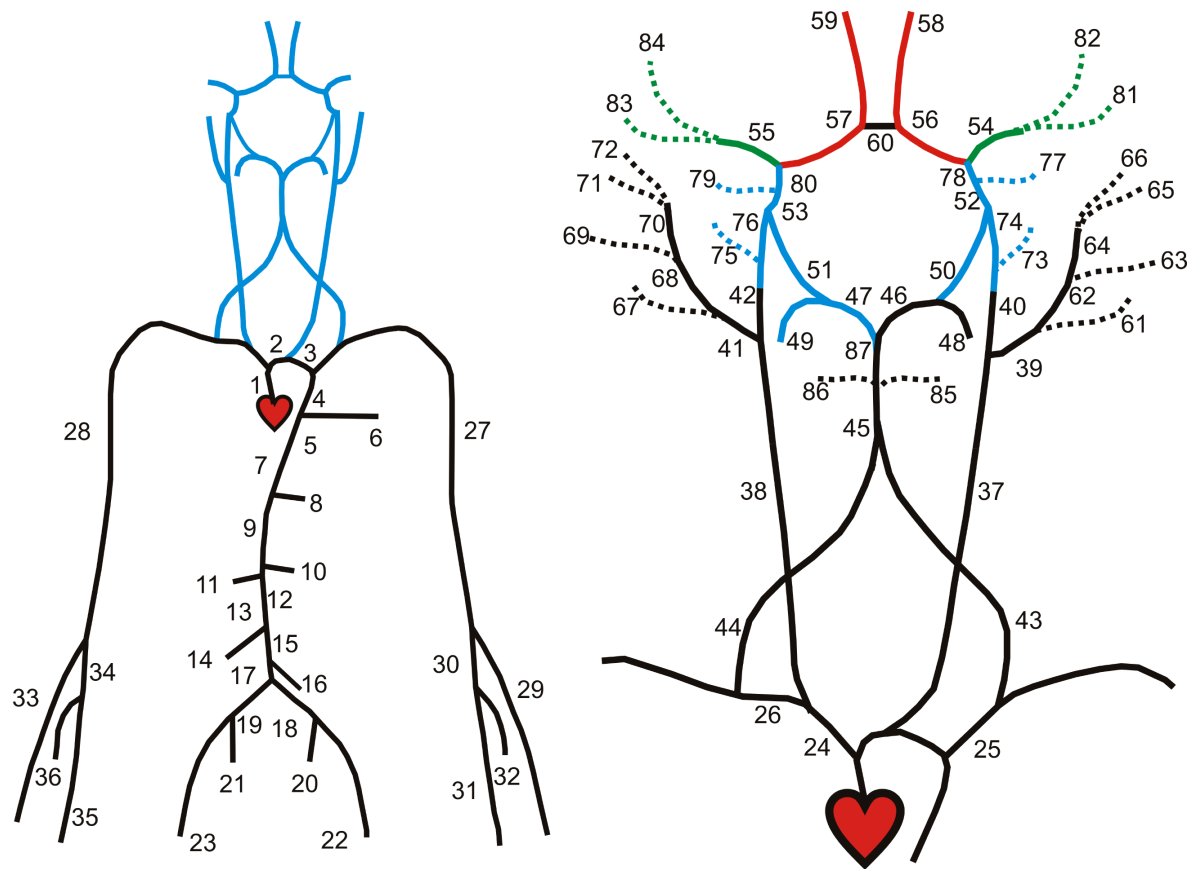


Figure A.1: The arterial segments in the patient-generic model.

The model parameters describing the geometry and boundary conditions applied are given in table A.1 (the abbreviations used are provided in table A.2). The lengths and radii are based on patient-generic from literature or the patient-specific data presented in this paper. The Young's moduli are based on literature (Westerhof et al., 1969; Alastruey et al., 2007b). The wall-thickness in the cerebral circulation is based on the radii of the segments, whereas the wall-thickness in the rest of the rest of the circulation is computed to match the compliances published by Stergiopoulos et al. (1992). The peripheral resistances and compliances are derived from the geometry as described in the methods section of this paper.

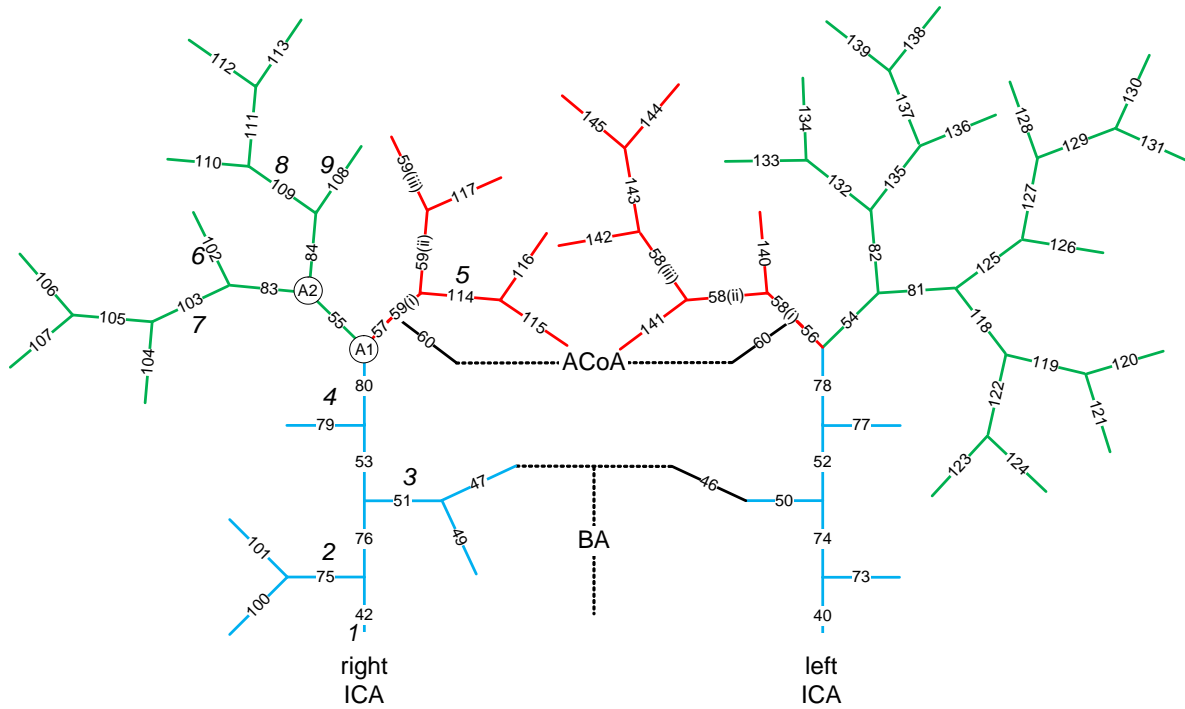


Figure A.2: The arterial segments in the patient-generic model.

**Table A.1:** Geometrical parameters and boundary conditions based on wall shear stress, so proportional to  $a^3$ . The vascular segments are visualised in figures A.1 and A.2 (patient-generic and patient-specific, respectively). Note, following convention in literature, the number of decimals given is higher than justified by the measurement and postprocessing methods in order to avoid rounding errors. The starts indicate a slight deviation from the reported geometry for stability reasons.

Name	Nr.	$l$ [mm]	$a_p$ [mm]	$a_d$ [mm]	$h \cdot 10$ [mm]	E [MPa]	$R \cdot 10^{-9}$ [Pa s m <sup>-3</sup> ]	$C \cdot 10^{10}$ [m <sup>3</sup> Pa <sup>-1</sup> ]
<b>Stergiopoulos et al. (1992)</b>								
ascending aorta	1	40	14.70	14.40	13.90	0.4		
aortic arch A	2	20	11.20	11.20	10.80	0.4		
aortic arch B	3	39	10.70	10.70	9.88	0.4		
thoracic aorta 1	4	52	9.99	9.99	8.68	0.4		
thoracic aorta 2	5	104	6.75	6.45	8.12	0.4		
intercostals	6	80	2.00	1.50	3.41	0.4	1.91	2.76
abdominal aorta A	7	53	6.10	6.10	7.34	0.4		
celiac	8	10	3.90	3.90	5.11	0.4	1.03	5.12
abdominal aorta B	9	10	6.00	6.00	6.64	0.4		
l./r. renal	10/11	32	2.60	2.60	4.03	0.4	1.22	4.33
abdominal aorta C	12	10	5.90	5.90	6.62	0.4		
abdominal aorta D1	13	53	5.80	5.64	6.25	0.4		
sup. mesenteric	14	59	4.35	4.35	5.55	0.4	0.78	6.75
abdominal aorta D2	15	53	5.64	5.48	6.22	0.4		
inf. mesenteric	16	50	1.60	1.60	3.03	0.4	15.71	0.34
abdominal aorta E	17	10	5.20	5.20	5.46	0.4		
l./r. common iliac	18/19	58	3.68	3.50	4.77	0.4		

Table A.1: continued

	Name	Nr.	$l$	$a_p$	$a_d$	$h \cdot 10$	E	$R \cdot 10^{-9}$	$C \cdot 10^{10}$
l./r.	internal iliac	20/21	50	2.00	2.00	3.06	1.6	4.64	1.14
l./r.	external iliac	22/23	144	3.20	2.70	4.15	0.8	1.88	2.80
	brachiocephalic	24	34	6.20	6.20	6.68	0.4		
l./r.	subclavian	25/26	34	4.23	4.23	5.39	0.4		
l./r.	brachial	27/28	422	4.03	2.36	5.04	0.4		
l./r.	radial	29/33	235	1.74	1.42	3.02	0.8	18.20	0.29
l./r.	ulnar A	30/34	67	2.15	2.15	3.46	0.8		
l./r.	ulnar B	31/35	171	2.03	1.83	3.36	0.8	8.53	0.62
l./r.	interosseous	32/36	79	0.91	0.91	1.89	1.6	69.36	0.08
Alastruey et al. (2007b)									
l.	CCA	37	208	2.50	2.50	6.25	0.4		
r.	CCA	38	177	2.50	2.50	6.25	0.4		
l./r.	ECA	39/41	177	1.50	1.50	3.75	0.8	4.86	1.36
l./r.	ICA	40/42	177	2.00	2.00	5.00	0.8		
l./r.	VA	43/44	148	1.36	1.36	3.40	0.8		
	BA	45	29	1.62	1.62	4.05	1.6		
l./r.	PCA P1	46/47	5	1.07	1.07	2.67	1.6		
l./r.	PCA P2	48/49	86	1.05	1.05	2.62	1.6	14.17	0.47
l./r.	PCoA	50/51	15	0.73	0.73	1.82	1.6		
l./r.	ICA B	52/53	5	2.00	2.00	5.00	1.6		
l./r.	MCA	54/55	119	1.43	1.43	3.58	1.6	5.61	1.18
l./r.	ACA A1	56/57	12	1.17	1.17	2.93	1.6		
l./r.	ACA A2	58/59	103	1.20	1.20	3.00	1.6	9.50	0.70
	ACoA	60	3	0.74	0.74	1.85	1.6		
Reymond et al. (2009)									
l.	CCA	37	139	6.00	3.00	11.30	0.4		
r.	CCA	38	94	6.75	3.50	12.82	0.4		
l.	ECA A	39	41	2.35	2.15	5.63	0.8		
r.	ECA A	41	41	2.50	2.25	5.94	0.8		
l./r.	sub. thy. asc.	61/67	101	1.00	0.50	1.88	0.8	45.30	0.11
l./r.	ECA B	62/68	61	2.00	1.75	4.69	0.8		
l./r.	maxillary	63/69	91	1.10	0.50	2.00	0.8	45.40	0.11
l./r.	sup. temporal	64/70	61	1.60	1.50	3.88	0.8		
l./r.	sup. temp. pa.	65/71	101	1.10	0.70	2.25	0.8	16.53	0.30
l./r.	sup. temp. fr.	66/72	100	1.10	0.70	2.25	0.8	16.53	0.30
l.	ICA A	40	178	2.65	2.05	5.88	0.8		
r.	ICA A	42	178	2.85	2.15	6.26	0.8		
l./r.	OphtA*	73/75	11	0.50	0.30	1.00	0.8	210.30	0.02
l./r.	ICA sinus	74/76	11	2.15	1.95	5.12	0.8		
l.	VA	43	148	1.85	1.40	4.06	0.8		
r.	VA	44	149	1.85	1.40	4.06	0.8		
	BA 1a*	45	15	2.00	1.85	4.81	1.6		
	BA 1b*		5	1.80	1.80	4.50	1.6		
l./r.	sub. cerebellar	85/86	10	0.85	0.70	1.94	1.6	16.49	0.30
	BA 2*	87	5	1.55	1.55	3.87	1.6		
l./r.	PCA P1	46/47	2	0.95	0.95	2.37	1.6		
l./r.	PCA P2	48/49	59	1.00	0.90	2.38	1.6	7.78	0.63

Table A.1: continued

	Name	Nr.	$l$	$a_p$	$a_d$	$h \cdot 10$	E	$R \cdot 10^{-9}$	$C \cdot 10^{10}$
l./r.	PCoA	50/51	4	0.60	0.60	1.50	1.6		
l./r.	ICA B1	52/53	2	1.95	1.90	4.81	1.6		
l./r.	ICA B2	78/80	2	1.90	1.90	4.75	1.6		
l./r.	AChorA	77/79	36	0.75	0.65	1.75	1.6	20.67	0.24
l./r.	MCA M1	54/55	8	1.50	1.40	3.62	1.6		
l./r.	MCA INF	81/83	70	1.00	0.50	1.88	1.6	45.30	0.11
l./r.	MCA SUP	82/84	71	1.00	0.50	1.88	1.6	45.30	0.11
l./r.	ACA A1	56/57	12	1.05	1.00	2.56	1.6		
l./r.	ACA A2	58/59	24	0.90	0.85	2.19	1.6	9.24	0.53
l./r.	ACoA	60	2	0.65	0.65	1.62	1.6		
Patient data (see chapter 3)									
l.	ICA	40	178.0	2.39	2.39	5.98	0.8		
r.	ICA	42	178.0	2.69	2.69	6.73	0.8		
r.	PCA	47	5.5	0.95	0.95	2.37	1.6		
l.	PCA	48	16.2	1.05	1.05	2.62	1.6	19.23	0.33
r.	PCA	49	16.2	1.15	1.15	2.87	1.6	14.63	0.44
l.	PCoA	50	18.0	0.64	0.64	1.60	1.6		
r.	PCoA	51	18.0	1.34	1.34	3.35	1.6		
l.	ICA B <sub>I</sub>	52	2.7	2.09	2.09	5.22	1.6		
r.	ICA B <sub>I</sub>	53	2.8	2.04	2.04	5.10	1.6		
l.	MCA M <sub>I</sub>	54	8.3	1.63	1.63	4.07	1.6		
r.	MCA M <sub>I</sub>	55	6.7	1.85	1.85	4.63	1.6		
l.	ACA A <sub>I</sub>	56	8.0	1.00	1.00	2.50	1.6		
r.	ACA A <sub>I</sub>	57	12.0	1.41	1.41	3.53	1.6		
l.	ACA A <sub>2</sub>	58(i)	3.3	1.00	1.00	2.50	1.6		
l.	ACA A <sub>2</sub>	58(ii)	0.7	1.48	1.48	3.70	1.6		
l.	ACA A <sub>2</sub>	58(iii)	9.7	1.14	1.14	2.85	1.6		
r.	ACA A <sub>2</sub>	59(i)	4.5	1.41	1.41	3.53	1.6		
r.	ACA A <sub>2</sub>	59(ii)	22.5	1.34	1.34	3.35	1.6		
r.	ACA A <sub>2</sub>	59(iii)	8.2	1.23	1.23	3.07	1.6	11.97	0.54
l.	OphtA	73	33.5	0.63	0.63	1.58	0.8	89.09	0.07
l.	ICA sinus	74	8.2	2.00	2.00	5.00	1.6		
r.	OphtA	75	31.2	0.77	0.77	1.92	0.8		
r.	ICA sinus	76	8.6	2.15	2.15	5.38	1.6		
l.	AChorA	77	36.8	0.41	0.41	1.02	1.6	323.70	0.02
l.	ICA B <sub>2</sub>	78	3.7	1.90	1.90	4.75	1.6		
r.	AChorA	79	24.6	0.59	0.59	1.48	1.6	108.50	0.06
r.	ICA B <sub>2</sub>	80	3.7	2.38	2.38	5.95	1.6		
l.	MCA INF	81	5.8	1.64	1.64	4.10	1.6		
l.	MCA SUP	82	11.6	1.35	1.35	3.38	1.6		
r.	MCA INF	83	4.3	2.09	2.09	5.22	1.6		
r.	MCA SUP	84	9.8	1.56	1.56	3.90	1.6		
r.	OphtA	100	3.1	0.59	0.59	1.48	0.8	108.50	0.06
r.	OphtA	101	10.0	0.66	0.66	1.65	0.8	77.55	0.08
r.	MCA	102	4.5	0.90	0.90	2.25	1.6	30.58	0.21
r.	MCA	103	23.1	0.99	0.99	2.47	1.6		
r.	MCA	104	3.4	0.88	0.88	2.20	1.6	32.68	0.20

Table A.1: continued

	Name	Nr.	$l$	$a_p$	$a_d$	$h \cdot 10$	E	$R \cdot 10^{-9}$	$C \cdot 10^{10}$
r.	MCA	105	25.3	0.59	0.59	1.48	1.6		
r.	MCA	106	9.4	0.57	0.57	1.42	1.6	120.40	0.05
r.	MCA	107	5.9	0.43	0.43	1.07	1.6	279.80	0.02
r.	MCA	108	14.0	0.71	0.71	1.78	1.6	62.30	0.10
r.	MCA	109	4.9	1.83	1.83	4.58	1.6		
r.	MCA	110	16.9	0.95	0.95	2.37	1.6	26.00	0.25
r.	MCA	111	4.6	1.21	1.21	3.02	1.6		
r.	MCA	112	9.7	1.17	1.17	2.93	1.6	13.89	0.46
r.	MCA	113	8.9	1.03	1.03	2.58	1.6	20.42	0.32
r.	ACA	114	20.1	0.77	0.77	1.92	1.6		
r.	ACA	115	25.8	0.66	0.66	1.65	1.6	77.50	0.08
r.	ACA	116	21.4	0.47	0.47	1.17	1.6	215.10	0.03
r.	ACA	117	21.8	0.83	0.83	2.08	1.6	38.93	0.17
l.	MCA	118	17.0	1.46	1.46	3.65	1.6		
l.	MCA	119	6.8	1.19	1.19	2.98	1.6		
l.	MCA	120	19.5	0.50	0.50	1.25	1.6	178.30	0.04
l.	MCA	121	5.5	1.20	1.20	3.00	1.6	12.90	0.50
l.	MCA	122	27.9	1.18	1.18	2.95	1.6		
l.	MCA	123	33.5	0.49	0.49	1.22	1.6	189.20	0.03
l.	MCA	124	18.1	0.84	0.84	2.10	1.6	37.55	0.17
l.	MCA	125	1.4	1.00	1.00	2.50	1.6		
l.	MCA	126	28.9	0.68	0.68	1.70	1.6	70.80	0.09
l.	MCA	127	1.4	1.00	1.00	2.50	1.6		
l.	MCA	128	26.4	0.41	0.41	1.02	1.6	323.70	0.02
l.	MCA	129	17.8	0.99	0.99	2.47	1.6		
l.	MCA	130	16.4	0.81	0.81	2.02	1.6	41.92	0.15
l.	MCA	131	4.6	0.86	0.86	2.15	1.6	35.00	0.18
l.	MCA	132	13.8	0.52	0.52	1.30	1.6		
l.	MCA	133	17.7	0.39	0.39	0.98	1.6	405.90	0.02
l.	MCA	134	46.2	0.38	0.38	0.95	1.6	376.00	0.02
l.	MCA	135	21.5	0.77	0.77	1.92	1.6		
l.	MCA	136	56.6	0.41	0.41	1.02	1.6	323.70	0.02
l.	MCA	137	7.2	0.85	0.85	2.12	1.6		
l.	MCA	138	13.6	0.35	0.35	0.88	1.6	519.50	0.01
l.	MCA	139	18.4	0.77	0.77	1.92	1.6	48.78	0.13
l.	ACA	140	9.5	0.38	0.38	0.95	1.6	405.90	0.02
l.	ACA	141	5.9	0.46	0.46	1.15	1.6	229.20	0.03
l.	ACA	142	24.3	0.82	0.82	2.05	1.6	40.42	0.16
l.	ACA	143	18.5	0.77	0.77	1.92	1.6		
l.	ACA	144	12.1	0.72	0.72	1.80	1.6	59.70	0.11
l.	ACA	145	22.0	0.60	0.60	1.50	1.6	103.20	0.06

**Table A.2:** Abbreviations of the names of the arterial segments.

Abbreviation	Name
ACA	anterior cerebral artery
AChorA	anterior choroidal artery
ACoA	anterior communicating artery
BA	basilar artery
CCA	common carotid artery
ECA	external carotid artery
ICA	internal carotid artery
MCA	middle cerebral artery
OphtA	ophthalmic artery
PCA	posterior cerebral artery
PCoA	posterior communicating artery
sup. cerebellar.	superior cerebellar
sup. temp. (p./f.)	superficial temporal (parietal/frontal)
sup. thy.	superior thyroid
sup./inf.	superior/inferior
VA	vertebral artery



## APPENDIX B

### Pressure measurements in the internal carotid artery during the injection of contrast agent

---

## B.1 Introduction

During the injection of contrast agent in the internal carotid artery, both the flows and the flow distribution change. The computational analysis of this procedure suggested that this effect depends on the geometry of the vasculature as well as the location within the vasculature (chapter 5). Although the flow is altered, the pressure rise computed is too small (less than 1%) to be measured accurately. If pressure measurements in the internal carotid during injection would support this finding, it would partially verify this model prediction.

The pressures obtained with the pressure wire (2 patients; see chapter 6) are used to confirm that the pressure increase induced by the injection of contrast agent during cerebral angiography is negligible, as predicted by the 1D wave propagation model described in chapter 5.

## B.2 Methods

The data (2 patients) was obtained with a pressure wire (ComboWire, Vulcano) situated 1 cm distal to the catheter tip (Royal Hallamshire Hospital, Sheffield). The ComboWire also allows the measurements of peak velocities, which visualised the exact timing of the injection. The measurement was performed over about 300 seconds, while the manual injection lasted about 4 seconds. All patients involved gave their informed consent.

In order to evaluate the effect of the injection on the pressure in the internal carotid artery, the variation of the cyclic mean (see chapter 6) in time was compared to the overall mean  $\pm$  the standard deviation. The velocity signal, which relies on red blood cells present in the fluid of which the velocity is being measured, showed strong irregularities over the course of the injection. These irregularities were used to confirm the timing of the injection.

## B.3 Results

The influence of the injection on the pressure is too small to be measured (fig B.1). Although the pressure briefly exceeds the mean+SD, this is also observed well before the injection ( $t \simeq 205$ ). The natural variations in blood pressures, i.e., the wave pattern observed in the cyclic averaged pressure, are higher than the increase caused by the pressure.

## B.4 Conclusion

The 1D model presented in chapter 5 predicted the pressure increase due to the injection of contrast agent would be too low to be captured by *in vivo* pressure measurements.

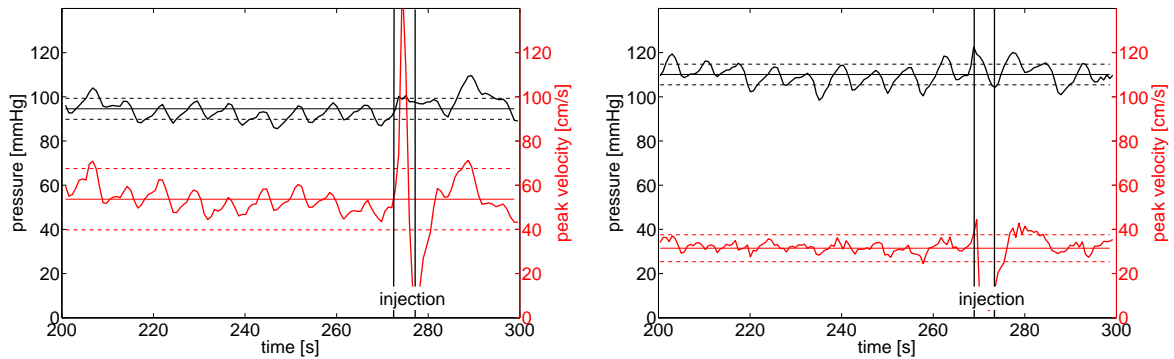


**Figure B.1:** The cyclic averaged pressure shows no increase due to the injection in (left) patient 1 and (right) patient 2. The included velocity signals clearly show the timing of the injection.

Indeed, the influence of the injection is smaller than the natural variations of the blood pressure caused by for example autoregulation, as no effect was observed in the pressures measured here. The pressure measurements performed during the injection of contrast agent verified the predictions by the 1D model presented in chapter 5, i.e., no significant increase in pressure is observed during the injection.



# Bibliography

---

- R Aaslid. Cerebral autoregulation and vasomotor reactivity. *Frontiers of neurology and neuroscience*, 21:216–228, 2006.
- R Aaslid, KF Lindegaard, W Sorteberg, and H Nornes. Cerebral autoregulation dynamics in humans. *Stroke*, 20(1):45–52, 1989.
- J Alastruey, SM Moore, KH Parker, T David, J Peiró, and SJ Sherwin. Reduced modelling of blood flow in the cerebral circulation: Coupling 1-D, 0-D and cerebral autoregulation models. *International journal for numerical methods in fluids*, 00:1–6, 2007a.
- J Alastruey, KH Parker, J Pieró, SM Byrd, and SJ Sherwin. Modelling the circle of willis to assess the effects of anatomical variations and occlusions on cerebral blood flows. *Journal of Biomechanics*, 40:1794–1805, 2007b.
- BH Amundsen, U Wisløff, J Helgerud, J Hoff, and SA Slørdahl. Ultrasound recorded axillary artery blood flow during elbow-flexion exercise. *Medicine & Science in Sports & Exercise*, 34(8):1288–1293, 2002.
- M Anliker, RL Rockwall, and E Ogden. Nonlinear analysis of flow pulses and shockwaves in arteries. part I: Derivation and properties of mathematical model. *Zeitschrift für angewandte Mathematik und Physik*, 22:217–246, 1971.
- T Anor, L Grinberg, H Baek, JR Madsen, MV Jayaraman, and GE Karniadaki. Modeling of blood flow in arterial trees. *Systems Biology and Medicine*, 2:612–623, 2010.
- F Asakura, H Tenjin, N Sugawa, S Kimura, and O Fumiya. Evaluation of intra-aneurysmal blood flow by digital subtraction angiography: blood flow change after coil embolization. *Surgical Neurology*, 59:310–319, 2003.
- K Azer and CS Peskin. A one-dimensional model of blood flow in arteries with friction and convection based on the womersley velocity profile. *Cardiovascular Engineering*, 7: 51–73, 2007.
- DC Banks and BA Singer. A predictor-corrector technique for visualizing unsteady flow. *IEEE Transactions on Visualization and Computer Graphics*, 1(2):151–163, June 1995.

- E Bartels. The axial imaging plane - the main domain of the transcranial color-coded duplex ultrasonography? *European Journal of Ultrasound*, 16:47–57, 2002.
- J Beck, S Rohde, J Berkefeld, V Seifert, and A Raabe. Size and location of ruptured and unruptured intracranial aneurysms measured by 3-dimensional rotational angiography. *Surgical Neurology*, 65:18–27, 2006.
- D Bessems, MCM Rutten, and FN van de Vosse. A wave propagation model of blood flow using an approximate velocity profile function. *Journal of Fluid Mechanics*, 580: 145–168, 2007.
- D Bessems, C Giannopapa, MCM Rutten, and FN van de Vosse. Experimental validation of a time-domain-based wave propagation model of blood flow in viscoelastic vessels. *Journal of Biomechanics*, 41:284–291, 2008.
- BWAMM Beulen, AC Verkaik, N Bijnens, MCM Rutten, and FN van de Vosse. Perpendicular ultrasound velocity measurement by 2d cross-correlation of rf data: part b. volume flow estimation in curved vessels. *Experiments in Fluids*, 49:1219–1229, 2010.
- H Bogunovic, JM Pozo, MC Villa-Uriol, CB Majoie, R van den Berg, HA van Andel, JM Macho, J Blasco, LS Roman, and Frangi AF. Automated segmentation of cerebral vasculature with aneurysms in 3d-ra and tof-mra using geodesic active regions: an evaluation study. *Medical Physics*, 38:210–222, 2011.
- L Boussel, V Rayz, C McCulloch, A Martin, G Acevedo-Bolton, M Lawton, R Higashida, WS Smith, WL Young, and D Saloner. Aneurysm growth occurs at region of low wall shear stress: patient-specific correlation of hemodynamics and growth in a longitudinal study. *Stroke*, 39(11):2997–3002, 2008.
- L Boussel, V Rayz, A Martin, G Acevedo-Bolton, MT Lawton, R Higashida, WS Smith, WL Young, and D Saloner. Phase-contrast magnetic resonance imaging measurements in intracranial aneurysms in vivo of flow patterns, velocity fields, and wall shear stress: comparison with computational fluid dynamics. *Magnetic Resonance in Medicine*, 61(2): 409–417, 2009.
- PC Buijs, MJ Krabbe-Hartkamp, CJ Bakker, EE de Lange, LM Ramos, MM Breteker, and WP Mali. Effect of age on cerebral blood flow: measurement with ungated two-dimensional phase-contrast mr angiography in 250 adults. *Radiology*, 209(3):667–674, 1998.
- JD Burns and RD Jr. Brown. Treatment of unruptured intracranial aneurysms: surgery, coiling, or nothing? *Current Neurology and Neuroscience Reports*, 9(1):6–12, 2009.
- CG Caro, TJ Pedley, RC Schroter, and WA Seed. *The mechanics of the circulation*. Oxford University Press, Oxford, UK, 1978.
- MA Castro, CM Putman, and JR Cebra. Computational modeling of cerebral aneurysms in arterial networks reconstructed from multiple 3d rotational angiography images. *Proc SPIE Medical Imaging 2005: Physics of Medical Imaging*, 5746:233–244, 2005.

- MA Castro, CM Putman, and JR Cebral. Patient-specific computational modeling of cerebral aneurysms with multiple avenues of flow from 3d rotational angiography images. *Academic Radiology*, 13(7):811–821, July 2006a.
- MA Castro, CM Putman, and JR Cebral. Patient-specific computational fluid dynamics modeling of anterior communicating artery aneurysms: a study of the sensitivity of intra-aneurysmal flow patterns to flow conditions in the carotid arteries. *AJNR American Journal of Neuroradiology*, 27:2061–2068, November/December 2006b.
- MA Castro, CM Putman, and JR Cebral. Computational fluid dynamics modeling of intracranial aneurysms: effects of parent artery segmentation on intra-aneurysmal hemodynamics. *AJNR American Journal of Neuroradiology*, 27:1703–1709, September 2006c.
- JR Cebral, MA Castro, S Appanaboyina, CM Putman, D Millan, and AF Frangi. Efficient pipeline for image-based patient-specific analysis of cerebral aneurysm hemodynamics: technique and sensitivity. *IEEE Transactions On Medical Imaging*, 24(4):457–467, April 2005a.
- JR Cebral, MA Castro, JE Burgess, RS Pergolizzi, MJ Sheridan, and CM Putman. Characterization of cerebral aneurysms for assessing risk of rupture by using patient-specific computational hemodynamics models. *AJNR Am J Neuroradiol*, 26:2550–2559, November/December 2005b.
- JR Cebral, MA Castro, D Millan, AF Frangi, and CM Putman. Pilot clinical study of aneurysm rupture using image-based computational fluid dynamics models. In: Amini AA, Manduca A, eds. *Proceedings SPIE: the International Society for Optical Engineering. Medical Imaging 2005: Physiology, Function, and Structure from Medical Images*, 5746: 245–256, 2005c.
- JR Cebral, RS Pergolizzi, and CM Putman. Computational fluid dynamics modeling of intracranial aneurysms: qualitative comparison with cerebral angiography. *Academic Radiology*, 14(7):804–813, July 2007.
- JR Cebral, MA Castro, CM Putman, and N Alperin. Flow-area relationship in internal carotid and vertebral arteries. *Physiological Measurement*, 29(5):585–594, 2008.
- JR Cebral, F Mut, D Sforza, R Löhner, E Scrivano, P Lylyk, and C Putman. Clinical applications of image-based CFD for cerebral aneurysms. *International Journal for Numerical Methods in Biomedical Engineering*, 27(7):977–992, 2011.
- I Chatziprodromou, A Tricoli, D Poulidakos, and Y Ventikos. Hemodynamics and wall remodelling of a growing cerebral aneurysm: a computational model. *Journal of Biomechanics*, 40:412–426, 2007.
- D Chemla, J-L Hébert, C Coirault, K Zamani, I Suard, P Colin, and Y Lecarpentier. Total arterial compliance estimated by stroke volume-to-aortic pulse pressure ratio in humans. *American journal of physiology - Heart and circulatory physiology*, 274:H500 – H505, 1998.

- PR Chen, K Frerichs, and R Spetzler. Current treatment options for unruptured intracranial aneurysms. *Neurosurgical Focus*, 17:E5, 2004a.
- PR Chen, K Frerichs, and R Spetzler. Natural history and general management of unruptured intracranial aneurysms. *Neurosurgical Focus*, 17:E1, 2004b.
- R Dammers, F Stifft, JHM Tordoir, JMM Hameleers, APG Hoeks, and PJEHM Kitslaar. Shear stress depends on vascular territory: comparison between common carotid and brachial artery. *Journal of Applied Physiology*, 94(485-489), 2003.
- T David and S Moore. Modeling perfusion in the cerebral vasculature. *Medical Engineering Physics*, 30:1227-1245, 2008.
- WR Dean. Note on the motion of fluid in a curved pipe. *Philosophical Magazine*, 4(20): 208-222, July 1927.
- WR Dean. The stream-line motion of fluid in a curved pipe. *Philosophical Magazine*, 5(30):673-695, April 1928.
- CR Deane and HS Markus. Colour velocity flow measurement: In vitro validation and application to human carotid arteries. *Ultrasound in Medicine & Biology*, 23(3):447-452, 1997.
- L Dempere-Marco, E Oubel, M Castro, C Putman, A Frangi, and J Cebral. CFD analysis incorporating the influence of wall motion: application to intracranial aneurysms. *Medical Image Computing and Computer Assisted Intervention*, 9:438-445, 2006.
- P Dickley and P Kailasnath. The diameter-cube hypothesis: a new biophysical model of aneurysm rupture. *Surgical Neurology*, 58(166-180), 2002.
- DR Enzmann, MR Ross, MP Marks, and NJ Pelc. Blood flow in major cerebral arteries measured by phase-contrast cine mr. *AJNR Am J Neuroradiol*, 15(1):123-129, 1994.
- R Fahrig, H Nikolov, AJ Fox, and DW Holdsworth. A three-dimensional cerebrovascular flow phantom. *Medical Physics*, 26(8):1589-1599, 1999.
- D Fiorella, FC Albuquerque, P Han, and CG McDougall. Preliminary experience using the neuroform stent for the treatment of cerebral aneurysms. *Neurosurgery*, 54:6-16, 2004.
- MD Ford, N Alperin, SH Lee, DW Holdsworth, and DA Steinman. Characterization of volumetric flow rate waveforms in the normal internal carotid and vertebral arteries. *Physiological Measurement*, 26(4):477-488, 2005a.
- MD Ford, GR Stuhne, HN Nikolov, DF Habets, SP Lownie, DW Holdsworth, and DA Steinman. Virtual angiography for visualization and validation of computational models of aneurysm hemodynamics. *IEEE Transactions on Medical Imaging*, 24(12): 1586-1592, 2005b.
- O Frank. Die grundform des arteriellen pulses. *Z. Biol.*, 37:483-526, 1899.

- MH Friedman and DL Fry. Arterial permeability dynamics and vascular disease. *Atherosclerosis*, 104:189–194, 1993.
- JH Gault, J Jr. Ross, and DT Mason. Patterns of brachial arterial blood flow in conscious human subjects with and without cardiac dysfunction. *Circulation*, 34:833–848, 1966.
- KK Gnanalingham, V Apostolopoulos, S Barazi, and K O’Neill. The impact of the international subarachnoid aneurysm trial (isat) on the management of aneurysmal subarachnoid haemorrhage in a neurosurgical unit in the uk. *Clinical Neurology and Neurosurgery*, 108:117–123, 2006.
- L Grinberg, E Cheever, T Anor, JR Madsen, and GE Karniadakis. Modeling blood flow circulation in intracranial arterial networks: a comparative 3d/1d simulation study. *Brain*, 124:249–278, 2001.
- AC Guyton and JE Hall. *Textbook of medical physiology*. W.B. Saunders Company, Philadelphia, 1996. ISBN 0721659446.
- C Hahn and MA Schwartz. Mechanotransduction in vascular physiology and atherogenesis. *Nature Reviews Molecular Cell Biology*, 10:53 – 62, 2009.
- K Hayashi, H Handa, S Nagasawa, A Okumura, and K Moritake. Stiffness and elastic behavior of human intracranial and extracranial arteries. *Journal of Biomechanics*, 13(2):175–184, 1980.
- J Hendrikse, AF van Raamt, Y van der Graaf, WPTM Mali, and J van der Grond. Distribution of cerebral blood flow in the circle of willis. *Radiology*, 235(1):184–189, 2005.
- DW Holdsworth, CJD Norley, R Fraynell, and BK Rutt. Characterization of common carotid artery blood-flow waveforms in normal human subjects. *Physiological Measurements*, 20:219–240, 1999.
- DI Hollnagel, PE Summers, D Poulidakos, and SS Kollias. Comparative velocity investigations in cerebral arteries and aneurysms: 3d phase-contrast mr angiography, laser doppler velocimetry and computational fluid dynamics. *NMR in Biomedicine*, 22:795–808, 2009.
- GA Holzapfel, TC Gasser, and M Stadler. A structural model for the viscoelastic behavior of arterial walls: Continuum formulation and finite element analysis. *European Journal of Mechanics - A/Solids*, 21(3):441 – 463, 2002.
- TJR Hughes and J Lubliner. On the one-dimensional theory of blood flow in the larger arteries. *Mathematical Biosciences*, 18:161–170, 1973.
- H Isoda, Y Ohkura, T Kosugi, M Hirano, MT Alley, R Bammer, NJ Pelc, H Namba, and H Sakahara. Comparison of hemodynamics of intracranial aneurysms between MR fluid dynamics using 3D cine phase-contrast MRI and MR-based computational fluid dynamics. *Neuroradiology*, 52:913–920, 2010.

- Y Itzchak, M Modan, R Adar, and V Deutsch. External iliac artery blood flow in patients with arteriosclerosis obliterans. *American Journal of Roentgenology*, 125(2):437–441, 1975.
- J Jeong and F Hussain. On the identification of a vortex. *Journal of Fluid Mechanics*, 285: 69–94, 1995.
- SC Johnston, RT Higashida, DL Barrow, LR Caplan, JE Dion, G Hademenos, LN Hopkins, A Molyneux, RH Rosenwasser, F Vinuela, and CB Wilson. Recommendations for the endovascular treatment of intracranial aneurysms. *Stroke*, 33, 2002.
- S Juvela, M Porras, and K Poussa. Natural history of unruptured intracranial aneurysms: probability and risk factors for aneurysm rupture. *Neurosurgical Focus*, 93:379–387, 2000.
- S Juvela, K Poussa, and M Porras. Factors affecting formation and growth of intracranial aneurysms: a long term follow up study. *Stroke*, 32:485–491, 2001.
- CJ Koebbe, E Veznedaroglu, P Jabbour, and RH Rosenwasser. Endovascular management of intracranial aneurysms: current experience and future advances. *Neurosurgery*, 59: S93–102, 2006.
- T Koivisto, R Vanninen, H Hurskainen, T Saari, J Hernesniemi, and M Vapalahti. Outcomes of early endovascular versus surgical treatment of ruptured cerebral aneurysms. *Stroke*, 31, 2000.
- D Krex, HK Schackert, and G Schackert. Genesis of cerebral aneurysms-an update. *Acta Neurochirurgica*, 143:429–449, 2001.
- SK Kyriacou and JD Humphrey. Influence of size, shape and properties on the mechanics of axisymmetric saccular aneurysms. *Journal of Biomechanics*, 29:1015–1022, 1996.
- RR Lall, CS Eddleman, BR Bendok, and HH Batjer. Unruptured intracranial aneurysms and the assessment of rupture risk based on anatomical and morphological factors: sifting through the sands of data. *Journal of Applied Physiology*, 26:E2, 2009.
- WK Laskey, HG Parker, VA Ferrari, WG Kussmaul, and A Noordergraaf. Estimation of total systemic arterial compliance in humans. *Journal of Applied Physiology*, 69:112–119, 1990.
- CAD Leguy, EMH Bosboom, APG Hoeks, and FN van de Vosse. Model based assessment of dynamic arterial blood volume flow from ultrasound measurements. *Medical and Biological Engineering and Computing*, 47:641–648, 2009.
- D Lesage, ED Angelini, I Bloch, and G Funka-Lea. A review of 3d vessel lumen segmentation techniques: Models, features and extraction schemes. *Medical Image Analysis*, 13 (6):819 – 845, 2009.
- DC Levin, DA Phillips, S Lee-Son, and PR Maroko. Hemodynamic changes distal to selective arterial injections. *Investigative Radiology*, 12(2):116–120, 1977.

- BB Lieber, V Livescu, LN Hopkins, and AK Wakhloo. Particle image velocimetry assessment of stent design influence on intra-aneurysmal flow. *Annals of Biomedical Engineering*, 30:768–777, 2002.
- BB Lieber, C Sadasivan, Q Hao, J Seong, and L Cesar. The mixability of angiographic contrast with arterial blood. *Medical Physics*, 36(11):5064–5078, 2009.
- DS Liebeskind. Collateral circulation. *Stroke*, 34:2279–2284, 2003.
- TM Liou and SN Liou. A review on *in vitro* studies of hemodynamic characteristics in terminal and lateral aneurysm models. *Proceedings of the National Science Council, Republic of China (B)*, 23:133–148, 1999.
- TM Liou and SN Liou. Pulsatile flows in a lateral aneurysm anchored on a stented and curved parent vessel. *Experimental Mechanics*, 44:253–160, 2004.
- RF Mabon, PD Soder, WA Carpenter, and DP Giddens. Fluid dynamics in cerebral angiography. *Radiology*, 128(3):669–676, 1978.
- AM Malek and S Izumo. Control of endothelial cell gene expression by flow. *Journal of Biomechanics*, 28(12):1515–1528, 1995.
- I Marshall, P Papathanasopoulou, and K Wartolowska. Carotid flow rates and flow division at the bifurcation in healthy volunteers. *Physiological Measurement*, 25:691–697, 2004.
- A Marzo, P Singh, P Reymond, N Stergiopoulos, U Patel, and R Hose. Influence of inlet boundary conditions on the local haemodynamics of intracranial aneurysms. *Computer Methods in Biomechanics and Biomedical Engineering*, 12:431–444, 2009.
- A Marzo, P Singh, I Larrabide, A Radaelli, S Coley, M Gwilliam, ID Wilkinson, P Lawford, P Reymond, U Patel, A Frangi, and DR Hose. Computational hemodynamics in cerebral aneurysms: the effects of modelled versus measured boundary conditions. *Annals of Biomedical Engineering*, 39:884–896, 2011.
- X Mellado, I Larrabide, M Hernandez, and A Frangi. Flux driven medial curve extraction. *The Insight Journal*, 2007.
- FJH Meyer and S Riederer. Pulsatile increase in aneurysm size determined by cine phase-contrast mr angiography. *Journal of Neurosurgery*, 78:879–883, 1993.
- P Mitchell and J Jakubowski. Risk analysis of treatment of unruptured aneurysms. *Journal of Neurology, Neurosurgery and Psychiatry*, 68:577–580, 2000.
- P Mitchell, A Gholkar, RR Vindlacheruvu, and D Mendelow. Unruptured intracranial aneurysms: benign curiosity or ticking bomb? *Neurology*, 3:85–92, 2004.
- P Mitchell, D Birchall, and D Mendelow. Blood pressure, fatigue, and the pathogenesis of aneurysmal subarachnoid hemorrhage. *Surgical Neurology*, 66:574–580, 2006a.

- P Mitchell, D Birchall, and D Mendelow. Blood pressure, fatigue, and the pathogenesis of aneurysmal subarachnoid hemorrhage. *Surgical Neurology*, pages 574–580, 2006b.
- K Mizoi, T Yoshimoto, Y Nagamine, T Kayama, and K Kosu. How to treat incidental cerebral aneurysms: a review of 139 consecutive cases. *Surgical Neurology*, 44:114–121, 1995.
- MA Moehring and MP Spencer. Power m-mode doppler (pmd) for observing cerebral blood flow and tracking emboli. *Ultrasound in Medicine and Biology*, 28:49–57, 2002.
- A Molyneux. International subarachnoid aneurysm trial (isat) of neurosurgical clipping versus endovascular coiling in 2143 patients with ruptured intracranial aneurysms: a randomised trial. *Lancet*, 360:1267–1274, 2002.
- AJ Molyneux, RSC Kerr, L-M Yu, M Clarke, M Sneade, JA Yarnold, and P Sandercock. International subarachnoid aneurysm trial (isat) of neurosurgical clipping versus endovascular coiling in 2143 patients with ruptured intracranial aneurysms: a randomised comparison of effects on survival, dependency, seizures, rebleeding, subgroups, and aneurysm occlusion. *Lancet*, 366:809–817, 2005.
- AJ Molyneux, RSC Kerr, J Birks, N Ramzi, J Yarnold, M Sneade, and J Rischmiller. Risk of recurrent subarachnoid haemorrhage, death, or dependence and standardised mortality ratios after clipping or coiling of an intracranial aneurysm in the international subarachnoid aneurysm trial (isat): long-term follow-up. *The Lancet Neurology*, 8:427–433, 2009.
- S Moore, T David, JG Chase, J Arnold, and J Fink. 3d models of blood flow in the cerebral vasculature. *Journal of Biomechanics*, 39:1454–1463, 2006.
- SK Morcos, P Dawson, JD Pearson, JY Jeremy, AP Davenport, MS Yates, P Tirone, P Cipolla, C de Haën, P Muschick, W Krause, H Refsum, CJ Emery, P Liss, A Nygren, J Haylor, ND Pugh, and JOG Karlsson. The haemodynamic effects of iodinated water soluble radiographic contrast media: a review. *European Journal of Radiology*, 29(1):31–46, 1998.
- TW Morris, MA Kern, and RW Katzberg. The effects of media viscosity on hemodynamics in selective arteriography. *Investigative Radiology*, 17(1):70–76, 1982.
- G Mulder, ACB Bogaerds, P Rongen, and FN van de Vosse. On automated analysis of flow patterns in cerebral aneurysms based on vortex identification. *Journal of Engineering Mathematics*, 64:391–401, 2009.
- G Mulder, ACB Bogaerds, P Rongen, and FN van de Vosse. The influence of contrast agent injection on physiological flow in the circle of willis. *Medical Engineering and Physics*, 33:195–203, 2011a.
- G Mulder, A Marzo, ACB Bogaerds, SC Coley, P Rongen, DR Hose, and FN van de Vosse. Patient-specific modelling of cerebral blood flow: geometrical variations in a 1d model. *Cardiovascular Engineering and Technology*, 2011b. *In press*.

- C Murray. The physiological principle of minimum work. i.the vascular system and the cost of blood volume. *Physiology*, 12:207–214, 1926.
- A Nader-Sepahi, M Casimiro, J Sen, and ND Kitchen. Is aspect ratio a reliable predictor of intracranial aneurysm rupture? *Neurosurgery*, 54:1343–1348, 2004.
- A Narracott, P Lawford, H Liu, R Himeno, and R Hose. Development of a model for the investigation of blood clotting in cerebral aneurysms following coiling. *Proceedings of the International Congress on Computational Bioengineeringjournal*, 2003.
- H Nornes, W Sorteberg, P Nakstad, SJ Bakke, R Aaslid, and K-F Lindegaard. Haemodynamic aspects of clinical cerebral angiography concurrent two vessel monitoring using transcranial doppler ultrasound. *Acta Neurochirurgica*, 105(3):89–97, 1990.
- Y Ohashi, T Horikoshi, M Sugita, T Yagishita, and H Nukui. Size of cerebral aneurysms and related factors in patients with subarachnoid hemorrhage. *Surgical Neurology*, 61:239–247, 2004.
- SO Oktar, C Yücel, D Karaosmanoglu, K Akkan, H Ozdemir, N Tokgoz, and T Tali. Blood-flow volume quantification in internal carotid and vertebral arteries: comparison of 3 different ultrasound techniques with phase-contrast mr imaging. *American Journal of Neuroradiology*, 27:363–369, 2006.
- MS Olufsen. A structured tree outflow condition for blood flow in the larger systemic arteries. *American Journal of Physiology*, 276:H257–H268, 1999.
- MS Olufsen, CS Peskin, WY Kim, A Nadim, and J Larsen. Numerical simulation and experimental validation of blood flow in arteries with structured-tree outflow conditions. *Annals of Biomedical Engineering*, 28(11):1281–1299, 2000.
- MS Olufsen, A Nadim, and LA Lipsitz. Dynamics of cerebral bleed flow regulation explained using a lumped parameter model. *American Journal of Physiology - Regulatory, Integrative and Comparative Physiology*, 282:611–622, 2002.
- L Parlea, R Fahrig, DH Holdsworth, and S Lownie. An analysis of the geometry of saccular intracranial aneurysms. *American Journal of Neuroradiology*, 20:1079–1089, 1999.
- T Passerini, MR De Luca, L Formaggia, A Quarteroni, and A Veneziani. A 3D/1D geometrical multiscale model of the cerebral vasculature. *Journal of Engineering Mathematics*, 2009.
- G Pavlisa, D Ozretic, T Murselovic, G Pavlisa, and M Rados. Sole stenting of large and giant intracranial aneurysms with self-expanding intracranial stents-limits and complications. *Acta Neurochirurgica*, 152:763–769, 2010.
- TJ Pedley. *The fluid dynamics of large blood vessels*. Cambridge University Press, Cambridge, UK, 1980.
- TJ Pedley and RD Kamm. The effect of secondary motion on axial transport in oscillatory tube flow. *Journal of Fluid Mechanics*, 193:347–367, 1988.

- MJ Perko. Duplex ultrasound for assessment of superior mesenteric artery blood flow. *European journal of vascular and endovascular surgery*, 21(2):106–116, 2001.
- SR Pope, LM Ellwein, CL Zapata, V Novak, CT Kelley, and MS Olufsen. Estimation and identification of parameters in a lumped cerebrovascular model. *Mathematical Biosciences and Engineering*, 6:93–115, 2009.
- ND Pugh. Haemodynamic and rheological effects of contrast media: the role of viscosity and osmolality. *European Radiology*, 6:S13–S15, 1996.
- VL Rayz, L Boussel, G Acevedo-Bolton, AJ Martin, WL Young, MT Lawton, R Higashida, and D Saloner. Numerical simulations of flow in cerebral aneurysms: comparison of cfd results and in vivo mri measurements. *Journal of Biomechanical Engineering*, 130(5):051011, 2008.
- VL Rayz, L Boussel, L Ge, JR Leach, AJ Martin, MT Lawton, C McCulloch, and D Saloner. Flow residence time and regions of intraluminal thrombus deposition in intracranial aneurysms. *Annals of Biomedical Engineering*, 38(10):3058–3069, 2010.
- PJ Reuderink. *Analysis of the flow in a 3D distensible model of the carotid artery bifurcation*. Phd thesis, Technische Universiteit Eindhoven, Eindhoven, 1991.
- P Reymond, F Merenda, F Perren, D Rüfenacht, and N Stergiopulos. Validation of a one-dimensional model of the systemic arterial tree. *American journal of physiology. Heart and circulatory physiology*, 297:H208–H222, 2009.
- GJ Rinkel. Natural history, epidemiology and screening of unruptured intracranial aneurysms. *Revue neurologique*, 164:781–786, 2008.
- GJ Rinkel, A Djibuti, M amd Algra, and J van Gijn. *Prevalence and risk of rupture of intracranial aneurysms: a systematic review*. PhD thesis, 1998.
- S Rudin, Z Wang, I Kyprianou, C Ionita, Y Wu, KR Hoffmann, DR Bednarek, and H Meng. Imaging stent-induced flow modification in cerebro-vascular aneurysms with x-ray micro-angiography. *International Symposium on Biomedical Imaging*, 2002.
- BW Schaaf and PH Abbrecht. Digital computer simulation of human systemic arterial pulse wave transmission: A nonlinear model. *Journal of Biomechanics*, 5(4):345 – 364, 1972.
- P Scheel, C Ruge, UR Petrich, and M Schöning. Color duplex measurement of cerebral blood flow volume in healthy adults. *Stroke*, 31(1):147–150, 2000.
- H Schmitt, M Grass, R Suurmond, T Köhler, V Rasche, S Hähnel, and S Heiland. Reconstruction of blood propagation in three-dimensional rotational x-ray angiography (3D-RA). *Computerized Medical Imaging and Graphics*, 29(7):507 – 520, 2005.
- M Schöning, J Walter, and P Scheel. Estimation of cerebral blood flow through color duplex sonography of the carotid and vertebral arteries in healthy adults. *Stroke*, 25: 17–22, 1994.

- J Schröder, H Keller, B Terwey, and U Mittmann. Hämodynamische effekte der intraarteriellen kontrastmittelinjektion. *Röfo: Fortschritte auf dem Gebiete der Röntgenstrahlen und der Nuklearmedizin*, 135(2):143–151, 1981.
- A Segal. *Sepran user manual and programmers guide*. Ingenieursbureau Sepra, Leidschendam, 2000.
- DM Sforza, R Lohner, C Putman, and J Cebal. Hemodynamic analysis of intracranial aneurysms with moving parent arteries: Basilar tip aneurysms. *International Journal for Numerical Methods in Biomedical Engineering*, 26:1219–1227, 2010.
- SJ Sherwin, L Formaggia, J Peiró, and V Franke. Computational modelling of 1d blood flow with variable mechanical properties and its application to the simulation of wave propagation in the human arterial system. *International Journal for Numerical Methods in Fluids*, 43:673–700, 2003.
- Y Shim, A Pasipoularides, CA Straley, TG Hampton, PF Soto, CH Owen, JW Davis, and DD Glower. Arterial windkessel parameter estimation: a new time-domain method. *Annals of Biomedical Engineering*, 22:66–77, 1994.
- A-M Shinneeb, JD Bugg, and R Balachandar. Variable threshold outlier identification in piv data. *Measurement Science and Technology*, 15:1722–1732, 2004.
- SD Shpilfoygel, RA Close, DJ Valentino, and GR Duckwiler. X-ray videodensitometric methods for blood flow and velocity measurement: A critical review of literature. *Medical Physics*, 27(9):2008–2023, 2000.
- K Siddiqi, S Bouix, A Tannenbaum, and SW Zucker. Hamilton-jacobi skeletons. *International Journal of Computer Vision*, 48:215–231, 2002.
- AC Simon, ME Safar, JA Levenson, GM London, BI Levy, and NP Chau. An evaluation of large arteries compliance in man. *American Journal of Physiology*, 237(5):H550–H554, 1979.
- PK Singh, A Marzo, SC Coley, G Berti, P Bijlenga, PV Lawford, M-C Villa-Uriol, D Rufenacht, KM McCormack, A Frangi, UJ Patel, and R Hose. The role of computational fluid dynamics in the management of unruptured intracranial aneurysms: a clinicians' view. *Computational intelligence and Neuroscience*, 2009:1–12, 2009.
- PK Singh, A Marzo, H Tahir, TF Weeratunge, K Kumar, M Boutarbouch, R Hose, UJ Patel, and SC Coley. Effects of heparin on the hemodynamic characteristics of intracranial aneurysms. *Journal of Neuroradiology*, 37:300–301, 2010.
- PS Slosberg. Unexpected results in long-term medically treated ruptured intracranial aneurysm including data on 14 patients followed more than 30 years each. *Acta Neurochirurgica*, 139:697–705, 1997.
- L Speelman, EMH Bosboom, GWH Schurink, J Buth, M Breeuwer, MJ Jacobs, and FN van de Vosse. Initial stress and nonlinear material behavior in patient-specific aaa wall stress analysis. *Journal of Biomechanics*, 42:1713–1719, 2009.

- RL Spilker and CA Taylor. Tuning multidomain hemodynamic simulations to match physiological measurements. *Annals of Biomedical Engineering*, 38:2635–2648, 2010.
- P Spiller, FK Schmiel, B Politz, M Block, U Fermor, W Hackbarth, J Jehle, R Korfer, and H Pannek. Measurement of systolic and diastolic flow rates in the coronary artery system by x-ray densitometry. *Circulation*, 68:337–347, 1983.
- BN Steele, MS Olufsen, and CA Taylor. Fractal network model for simulating abdominal and lower extremity blood flow during resting and exercise conditions. *Computer Methods in Biomechanics and Biomedical Engineering*, 10(1):39–51, 2007.
- DA Steinman. Image-based computational fluid dynamics modeling in realistic arterial geometries. *Annals of Biomedical Engineering*, 30:483–497, 2002.
- N Stergiopoulos, DF Young, and TR Rogge. Computer simulation of arterial blood flow with applications to arterial and aortic stenosis. *Journal of Biomechanics*, 25:1477–1488, 1992.
- N Stergiopoulos, JJ Meister, and N Westerhof. Evaluation of methods for estimation of total arterial compliance. *American Journal of Physiology*, 268:H1540–H1548, 1995.
- N Stergiopoulos, B Westerhof, and N Westhof. Total arterial inertance as the fourth element of the windkessel model. *American Journal of Physiology*, 276:H81–H88, 1999.
- P Stoeter, N Prey, C Hoffmann, HJ Büdingen, and R Bergleiter. Doppler-sonographic examination of the arterial flow in the carotid and supraorbital arteries during carotid angiography. *Neuroradiology*, 26(3):199–207, 1984.
- H Tanaka, N Fujita, T Enoki, K Matsumoto, Y Watanabe, K Murase, and H Nakamura. Relationship between variations in the circle of willis and flow rates in internal carotid and basilar arteries determined by means of magnetic resonance imaging with semi-automated lumen segmentation: reference data from 125 healthy volunteers. *AJNR American Journal of Neuroradiology*, 27:1770 – 1775, 2006.
- H Tenjin, F Asakura, Y Nakahara, K Matsumoto, T Matsuo, F Urano, and S Ueda. Evaluation of intraaneurysmal blood velocity by time-density curve analysis and digital subtraction angiography. *American Journal of Neuroradiology*, 19:1303–1307, 1998.
- T Terada, M Tsuura, and Matsumoto H. Endovascular treatment of unruptured cerebral aneurysms. *Acta Neurochirurgica Supplementum*, 94:87–91, 2005.
- R Torii, M Oshima, T Kobayashi, K Takagi, and TE Tezduyar. Influence of wall elasticity in patient-specific hemodynamic simulations. *Computers & Fluids*, 36(1):160–168, 2007.
- R Torii, M Oshima, T Kobayashi, K Takagi, and TE Tezduyar. Fluid-structure interaction modelling of blood flow and cerebral aneurysm: significance of artery and aneurysm shapes. *Computers Methods in Applied Mechanics and Engineering*, 198(45-46):3613–3621, 2009.

- G Tsvigoulis, AV Alexandrov, and MA Sloan. Advances in transcranial doppler ultrasonography. *Current Neurology and Neuroscience Reports*, 9(1):46–54, 2009.
- H Ujiie, H Tachibana, O Hiramatsu, AL Hazel, T Matsumoto, Y Ogasawara, H Nakajima, T Hori, K Takakura, and F Kajiya. Effects of size and shape (aspect ratio) on the hemodynamics of saccular aneurysms: a possible index for surgical treatment of intracranial aneurysms. *Neurosurgery*, 45:119–129, 1999.
- FN van de Vosse and N Stergiopoulos. Pulse wave propagation in the arterial tree. *Annual Review of Fluid Mechanics*, 43:467–499, 2011.
- FN van de Vosse, J de Hart, CHGA van Oijen, D Bessems, TWM Gunther, A Segal, BJB Wolters, JMA Stijnen, and FPT Baaijens. Finite-element-based computational methods for cardiovascular fluid-structure interaction. *Journal of Engineering Mathematics*, 47:335–368, 2003.
- G van der Graaf. Gpiv software. 2007.
- J van Gijn and GJE Rinkel. Subarachnoid haemorrhage: diagnosis, causes and management. *Brain*, 124:249–278, 2001.
- P Venugopal, D Valentino, H Schmitt, P Villablanca, F Viñuela, and G Duckwiler. Sensitivity of patient-specific numerical simulation of cerebral aneurysm hemodynamics to inflow boundary conditions. *Journal of Neurosurgery*, 106:1051–1060, 2007.
- SJ Vermeersch, ER Rietzschel, ML De Buyzere, D De Bacquer, G De Backer, LM Van Bortel, TC Gillebert, PR Verdonck, and Segers P. Determining carotid artery pressure from scaled diameter waveforms: comparison and validation of calibration techniques in 2026 subjects. *Physiological Measurement*, 29:1267–1280, 2008.
- IE Vignon-Clementel, CA Figueroa, AL Marsden, JA Feinstein, KE Jansen, and CA Taylor. Outflow boundary conditions for three-dimensional finite element modeling of blood flow and pressure in arteries. *Computer methods in applied mechanics and engineering*, 195:3776–3796, 2006.
- I Waechter, J Bredno, R Hermans, J Weese, DC Barratt, and DJ Hawkes. Model-based blood flow quantification from rotational angiography. *Medical Image Analysis*, 12(5):586–602, 2008. Special issue on the 10th international conference on medical imaging and computer assisted intervention - MICCAI 2007.
- T Warelius. Effects of contrast medium injection on haemodynamics in cerebral angiography. *British Journal of Radiology*, 40:538–540, 1967.
- PN Watton, A Selimovic, NB Raberger, P Huang, GA Holzapfel, and Y Ventikos. Modelling evolution and the evolving mechanical environment of saccular cerebral aneurysms. *Bimechanics and Modeling in Mechanobiology*, 10:109–132, 2011.
- JJ Wentzel, FJH Gijzen, N Stergiopoulos, PW Serruys, CJ Slager, and R Krams. Shear stress, vascular remodeling and neointimal formation. *Journal of Biomechanics*, 36:681–688, 2003.

## REFERENCES

---

- N Westerhof, F Bosman, CJ De Vries, and A Noordergraaf. Analog studies of the human systemic arterial tree. *Journal of Biomechanics*, 2:121–143, 1969.
- N Westerhof, G Elzinga, and P Sipkema. An artificial arterial system for pumping hearts. *Journal of Applied Physiology*, 31(5):776–781, 1971.
- N Westerhof, J-W Lankhaar, and BE Westerhof. The arterial windkessel. *Medical and Biological Engineering and Computing*, 47(2):131–141, 2009.
- J Westerweel. Efficient detection of spurious vectors in particle image velocimetry data. *Experiments in Fluids*, 16(3-4):236–247, Februari 1994.
- DO Wiebers, JP Whisnant, and J Huston. Unruptured intracranial aneurysms: natural history, clinical outcome, and risks of surgical and endovascular treatment. *Lancet*, 362:103–110, 2002.
- HR Winn, JA Jane, J Taylor, D Kaiser, and GW Britz. Prevalence of asymptomatic incidental aneurysms: review of 4568 arteriograms. *Journal of Neurosurgery*, 96:43–49, 2002.
- K Yavuz, S Geyik, I Saatci, and HS Cekirge. Wingspan stent system in the endovascular treatment of intracranial aneurysms: clinical experience with midterm follow-up results. *Journal of Neurosurgery*, 109(3):445–453, 2008.
- B Yazici, B Erdoğan, and A Tugay. Cerebral blood flow measurements of the extracranial carotid and vertebral arteries with doppler ultrasonography in healthy adults. *Diagn Interv Radiol*, 11:195–198, 2005.
- C Zhang, M-C Villa-Uriol, M De Craene, JM Pozo, and AF Frangi. Morphodynamic analysis of cerebral aneurysm pulsation from time-resolved rotational angiography. *IEEE Transactions on Medical Imaging*, 28, 2009.

# Samenvatting

---

Cerebrale aneurysmata zijn gelokaliseerde, pathologische verwijdingen van cerebrale arteriën, voornamelijk in de cirkel van Willis. Hoewel niet alle aneurysmata instabiel zijn, vormt de kans op ruptuur een significant klinisch probleem. De bloeding als gevolg van ruptuur wordt geassocieerd met een hoge morbiditeit en mortaliteit. Aangezien de huidige indicatoren voor instabiliteit, gebaseerd op morfologische factoren, onvoldoende betrouwbaar zijn, worden er nieuwe indicatoren voor de stabiliteit van aneurysmata gezocht.

Hemodynamische factoren zijn waarschijnlijk relevant in de ontwikkeling en stabiliteit van aneurysmata, omdat zij bij de remodelering van de arteriële wand een belangrijke rol spelen. Studies suggereren dat bijvoorbeeld de afschuifspanning en stromingspatronen in een aneurysma mogelijke parameters zijn in beoordeling van de stabiliteit. Deze factoren kunnen worden geschat als het lokale 3D patiënt-specifieke snelheidsveld bekend is, welke kan worden verkregen met behulp van een combinatie van metingen en modellen. De belangrijkste factoren die het snelheidsveld beïnvloeden, zijn de vasculaire geometrie en het debiet door deze geometrie. In de afgelopen tien jaar zijn de technieken nodig voor het verkrijgen van de vasculaire geometrie verbeterd. Meer recentelijk is de focus verschoven naar het verkrijgen van meer realistische randvoorwaarden voor het te modelleren 3D-vasculaire segment.

Het doel van dit onderzoek is om de betrouwbaarheid van het met numerieke modellen verkregen snelheidsveld in een aneurysma te verbeteren. Er wordt een protocol voorgesteld om patiënt-specifieke randvoorwaarden voor het te modelleren 3D-segment te schatten, zonder extra invasieve procedures uit te moeten voeren. Met behulp van een 1D golfvoortplantings model, dat gebaseerd is op een patiënt-specifieke geometrie en randvoorwaarden, kunnen op beter bereikbare locaties gemeten druk en debiet vertaald worden naar randvoorwaarden voor het 3D model. Een dergelijk protocol biedt de mogelijkheid tot een verbeterde statistische betrouwbaarheid, gezien de toename van het aantal patiënten dat kan deelnemen aan studies voor het identificeren van relevante indicatoren.

Met behulp van vortex identificatie, zoals beschreven in hoofdstuk 2, kan de vortexdynamica van de stromingspatronen in een aneurysma worden gekwantificeerd. Hoewel een patiënt-specifieke geometrie vaak wordt gebruikt voor 3D-segmenten, is het 1D model waarop de randvoorwaarden voor het 3D model zijn gebaseerd meestal patiënt-generiek.

In hoofdstuk 3 wordt een patiënt-specifieke geometrie voor het 1D model gedefinieerd. De resulterende flow golven aan de randen van het 3D-segment zijn vergeleken met de golven verkregen met een patiënt-generieke geometrie. De invloed van deze verschillende in de randvoorwaarden op het 3D snelheidsveld in het aneurysma wordt geëvalueerd in hoofdstuk 4. Sommige methoden om debiet te meten vereisen de injectie van een contrastmiddel. In hoofdstuk 5 wordt het effect van deze injectie op het te meten debiet gemodelleerd. Op basis van druk metingen in de interne carotide zijn variaties van de vorm van de druk golven en het effect van deze variaties op de randvoorwaarden voor het 1D model geanalyseerd. Tenslotte wordt in hoofdstuk 7 een protocol voor volledige patiënt-specifieke modellering besproken.

# Acknowledgements

---

First, I greatly acknowledge the iXR Innovation department from Philips Healthcare for providing the funding for the research presented in this thesis. From this department, I thank Tom Bruijns, Roel Hermans and Peter Rongen, especially since they were also involved in my Master project, which has been the foundation for this PhD project.

My supervisors, Frans and Arjen, I would like to thank for your input and support, and for providing a nice working atmosphere where no discussion was avoided. Furthermore, Frans, thank you for your understanding, the evening entertainment and for the many years that we have worked together in general.

From the University of Sheffield, I would like to thank Rod Hose for enabling the patient measurements and my three month stay. Furthermore, I would like to acknowledge Stuart Coley for performing the patient measurements and allowing me to be present during the coiling procedure and measurements to improve my understanding. A special thanks to Alberto for all the work he did in extracting the pressure data and providing me with the right tools to analyse the patient-specific geometry. Richard, although I greatly appreciate the work you did to enable chapter 4, the many relaxing breaks during the day as well as the evenings, which I couldn't have done without, mean even more to me.

I would like to thank the colleagues I shared the office with over the past few years for providing me with the vital distractions; Bart for being just as addicted to coffee as I am; Lars for the 'fresh-air' addiction; Peter for sharing feelings about our PhD; René for the conversations about, e.g., partners and houses. Erica, I greatly appreciate the office outings that you organised, and of course our weekly lunch in the last few months. You've been a great friend, and I'm absolutely positive we will be for many years to come.

Frederike, thank you for helping me with the cover design, the physical challenge, and for getting me my job at Virtual Proteins. I would like to thank all my colleagues at Virtual Proteins, and Frits and Sigrid in particular, for putting up with me and helping me out whenever I was feeling to sleep-deprived to think straight. Of course I should thank my friends for still being my friends even after I disappeared for prolonged periods of time. Although my family was not as involved as during my Masters project, the many phone calls and help in our building-site-distraction project has been greatly appreciated. Gareth, I wouldn't have made it without you, thank you for all the support and for making me laugh at least once a day.



# Curriculum Vitae

---

Gwen Mulder werd geboren op 13 april 1981 te Eindhoven. In 1999 behaalde ze haar VWO diploma aan het Strabrecht College in Geldrop. Gedurende haar studie Biomedische Technologie aan de Technische Universiteit Eindhoven (1999-2006) liep zij stage aan de Canterbury University in Christchurch, New Zealand. Haar afstudeerproject, waarin de snelheidsvelden in een geidealiseerd cerebraal aneurysma zowel experimenteel als numeriek werden beschouwd, was opgezet in samenwerking met de X-ray Predevelopment afdeling binnen Philips Healthcare, Best. De vragen die rezen gedurende dit project leidde tot haar promotie onderzoek, waarin de samenwerking met Philips werd voortgezet. Ten behoeve van het verkrijgen van patient data werd tevens een samenwerking aangegaan met Medical Physics Group van The University Of Sheffield, waarvoor zij drie maanden in Sheffield heeft doorgebracht. De resultaten van dit onderzoek staan beschreven in dit proefschrift.